

Radiation Damage in Hexagonal-close-packed metals.

A thesis submitted in accordance with the requirements of the
University of Liverpool for the degree of Doctor in Philosophy by:

Duncan Howard Yellen

01/4/90

Dept of Materials Science and Engineering
University of Liverpool
P.O Box 147
Liverpool L69 3BX

Abstract

Radiation damage in hexagonal-close-packed metals.

Duncan Howard Yellen

Displacement cascades have been established to be the primary cause of damage in materials exposed to a fast-neutron flux. The production of vacancy loops by this mechanism is of particular importance, these loops are known to play a major role in the microstructural development during irradiation. Despite current and potential applications for h.c.p materials, (e.g zircaloy, used for fuel cladding in PWR's) little is known of the cascade processes.

In this thesis attention is focussed on cascade collapse to form vacancy loops in five of the h.c.p metals, namely titanium, cobalt, rhenium, ruthenium and magnesium, chosen for their wide-ranging material properties. Heavy-ions have been used to simulate the energetic recoils created in collisions between fast neutrons and lattice atoms, the ensuing cascades may then collapse to form vacancy dislocation loops, these loops have been studied using transmission electron microscopy. This enables detailed analysis of loop geometries, sizes and number densities. Single energy antimony ions and molecules of energies between 50 and 150 keV have been employed. To allow for the anisotropic nature of the h.c.p crystallography, each material has been irradiated in single crystal form in two separate orientations, parallel (S_3) and normal (S_1) to the basal plane.

The efficiency of collapse has been noted to vary dramatically for the five metals studied, these variations do not correlate simply with any one material parameter such as melting point, c/a ratio or atomic weight. In titanium, the probability of visible vacancy loop production is very low, this contrasts with cobalt, a material of similar atomic weight and melting point, where a significant proportion of the vacancies created are retained as visible loops (~10%). Ruthenium, chosen for its similarity in many respects to zirconium, also exhibits a high retention efficiency of 5-10%. A significant feature of the results is that basal loops with a c-component to their Burgers vector have been observed in ruthenium and titanium, although these are not the metals with the lowest basal-plane stacking fault energies.

The data collected from this extensive study of heavy-ion damage in h.c.p materials has enhanced understanding of the complexities of the processes involved in cascade formation, and illuminates the point that no one materials parameter is solely responsible for the evolution of the observed microstructure.

Contents.

	<u>Page number.</u>
<u>Chapter 1 Introduction.</u>	11
<u>Chapter 2 Radiation Damage.</u>	
2.1: Introduction.	13
2.2 : Cascade evolution.	15
2.3 : Factors affecting cascade collapse.	17
2.4 : Crystallographic effects.	23
2.4.i : Replacement collision sequences.	23
2.4.ii : Channelling.	25
2.5 : The suitability of heavy ion and near surface studies.	27
2.6 : Cascade Quantification.	30
2.7 : Experimental cascade observations.	33
2.7.i : Field ion microscopy.	33
2.7.ii : Transmission electron microscopy (T.E.M) observations.	34
2.7.iii : Observation of defects In varying crystal systems.	35
2.7.iv : Yield and efficiency trends observed.	38
2.7.v : Temperature effects.	39
2.8 : Summary.	39
<u>Chapter 3 H.C.P materials.</u>	
3.1 : Introduction.	42
3.2 : Miller-Bravais indices.	42
3.3 : Dislocation loops in h.c.p metals.	44
3.4 : T.E.M observations of loops in h.c.p metals.	47
3.4.i : Quenching studies.	48
3.4.ii : Electron Irradiations.	49
3.4.iii : Heavy ion irradiations.	50

	<u>Page number.</u>
3.4.IV : Neutron irradiations.	51
3.4.v : Zirconium.	52
3.5 : Computer modelling.	55
3.6 : Trends.	55
 <u>Chapter 4 : Experimental methods.</u>	
4.1 : Background.	60
4.2 : Materials.	60
4.3 : Disc preparation.	62
4.4 : Chemical etching.	64
4.5 : Foil irradiation.	64
4.5.i : Dosimetry Using Ordered Alloys.	66
4.5.ii : Foil Orientation.	67
4.5.iii : Channelling Effects.	68
4.6 : Transmission electron microscopy.	69
4.7 : Interpretation of Data.	73
4.8: Scanning transmission electron microscopy (S.T.E.M).	75
 <u>Chapter 5 Results.</u>	
5.1 : Introduction.	83
5.2 : Atomic Ion implants.	83
5.3 : The antimony ion matrix.	84
5.4 : Loop nature and depth.	85
5.5 : Loop analysis.	85
5.5.i : The S_1 orientation.	85
5.5.ii : The S_3 orientation.	87
5.6 : Loop size and density.	87
5.6.i : S_1 foils.	87

	<u>Page number.</u>
5.6.ii : Low dose irradiations.	88
5.6.iii : S ₃ foils.	89
5.7 : Quantitative results.	89
5.8 : Vacancy concentration and energy density.	89
5.9 : Commercial titanium Irradiations.	90
5.10. : Other metals.	91
5.10.i : S ₁ foils.	91
5.10.ii : S ₃ foils.	92
5.11 : Trends.	93

Chapter 6 Cascade collapse in titanium.

6.1 : Introduction.	129
6.2 : Loop depth.	130
6.3 : Loop geometry.	133
6.3 i : Faulted and perfect loops.	133
6.3 ii : Loop normal.	134
6.3.iii : Basal loops.	135
6.4 : Stacking fault energy.	138
6.4.i : Prism plane stacking fault energy of titanium.	139
6.4.ii : Basal plane stacking fault energy of titanium.	139
6.5 : S ₁ Orientation commercial titanium.	140
6.5.i : Loop depth.	141
6.5.ii : Loop geometry.	141
6.5.iii : Stacking fault energy.	141
6.6 : Defect yield and efficiency calculations.	142
6.6.i : Sub-cascade formation.	142
6.6.ii : Corrections to measured parameters.	143
6.6.iii : Defect yield trends.	144

	<u>Page number.</u>
6.6.iv : Loop size and cascade efficiency.	145
6.6.v : Yield and efficiency for commercial titanium.	148
6.7 : Segregation.	149
<u>Chapter 7 Cascade collapse in h.c.p metals.</u>	
7.1 Introduction.	159
7.2 : Materials parameters: their relation to the defect density.	160
7.2.i : Melting point.	160
7.2.ii : Atomic Mass	161
7.2.iii : c/a ratio	161
7.2.iv : Stacking fault energy	162
7.2.v : Vacancy concentration and energy density	163
7.2.vi : Electron-phonon coupling	164
7.3 : Individual characteristics of the metals studied.	165
7.3.i : Magnesium.	166
7.3.ii : Cobalt.	167
7.3.iii : Ruthenium.	169
7.3.iv: Rhenium.	170
7.4 : Comparison to cubic metals.	171
7.5 : Summary.	171
7.6 : Implications for reactor construction materials.	172
7.7 : Cluster fusion.	172
<u>Chapter 8 Summary and Suggestions for Further Work.</u>	
8.1 : Summary.	184
8.2 : Suggestions for further work.	185
<u>References</u>	186-196

List of Illustrations.

	<u>Page number.</u>
Fig 2.1: Quasi-melting behaviour.	41
Fig 3.1: Hexagonal-close packed-crystallography.	57
Fig 3.2: Basal faults.	58
Fig 4.1: The Lintott ion-implanter.	81
Fig 4.2: Black-white reversals.	82
Fig 5.1: Depth distribution for 150 keV Sb_3^+ ions in S_1 iodide Ti.	105
Fig 5.2: Depth distributions for S_1 Ti.	106
Fig 5.3: W.S.S theoretical depth chart.	107
Fig 5.4: Stereo pair for 150 keV Sb_3^+ ions in commercial Ti.	108
Fig 5.5: S_1 analysis.	109-111
Fig 5.6: Loop normals.	112
Fig 5.7: S_3 analysis.	113
Fig 5.8 Loop sizes for 150 keV Sb_3^+ ions in S_1 iodide Ti.	114
Fig 5.9: Loop sizes for S_1 iodide Ti.	115
Fig 5.10: Loop sizes for S_3 iodide Ti.	116
Fig 5.11: Chart of $d.y$ and ϵ for Ti (S_1).	117
Fig 5.12: Chart of $d.y$ and ϵ for Ti (S_3).	118
Fig 5.13: $d.y$, and ϵ vs irradiation parameters for S_1 iodide Ti.	119
Fig 5.14: $d.y$, and ϵ vs irradiation parameters for S_3 iodide Ti.	120
Fig 5.15: N.R.T theoretical damage estimates.	121
Fig 5.16: Cascade volume per ion for Ti.	122
Fig 5.17: Vacancy concentration per ion for Ti.	123
Fig 5.18: Energy density per ion for Ti.	124

	<u>Page number.</u>
Fig 5.19: Irradiation parameters vs d.y and ϵ for S_1 "comm" Ti.	125
Fig 5.20: A micrograph of each metal irradiated.	126-127
Fig 5.21: Loop sizes for the range of h.c.p metals.	128
Fig 6.1: Iodide and commercial Ti unfaulting probabilities.	154
Fig 6.2: Micrograph of a low dose irradiation in Ti.	155
Fig 6.3: Efficiency vs vacancy concentration.	156
Fig 6.4: Efficiency vs energy density.	157
Fig 6.5: Molecular ion recombination effects.	158
Fig 7.1: D.R.E, d.y, and ϵ vs melting point.	174
Fig 7.2: D.R.E, d.y, and ϵ vs atomic mass.	175
Fig 7.3: D.R.E, d.y, and ϵ vs c/a ratio.	176
Fig 7.4: D.R.E, d.y, and ϵ vs stacking fault energy.	177
Fig 7.5: D.R.E, d.y, and ϵ vs vacancy concentration.	178
Fig 7.6: D.R.E, d.y, and ϵ vs energy density.	179
Fig 7.7: c/a ratio vs stacking fault energy.	180
Fig 7.8: Energy density per atom vs ion energy.	181
Fig 7.9: Vacancy concentration per atom vs ion energy.	182
Fig 7.10: D.R.E, d.y, and ϵ vs electron-phonon coupling.	183

List of Tables.

	<u>Page number.</u>
Table 3.1: Properties of the hexagonal metals.	59
Table 4.1: Annealing conditions.	76
Table 4.2: Electropolishing conditions.	77
Table 4.3: Irradiations performed.	78
Table 4.4: $g \cdot b$ values.	79
Table 4.5: Extinction distances.	80
Table 5.1: Implications of the antimony ion matrix.	94
Table 5.2: Depth measurements.	95
Table 5.3: S_1 iodide Ti results.	96
Table 5.4: Loop normals.	97
Table 5.5: S_3 iodide Ti results.	98
Table 5.6: Loop sizes for S_1 iodide Ti	99
Table 5.7: Low dose S_1 iodide Ti results.	100
Table 5.8: Loop sizes for S_3 iodide Ti.	101
Table 5.9: S_1 commercial Ti results.	102
Table 5.10: Loop sizes for the range of h.c.p metals.	103
Table 5.11: Results from the range of h.c.p metals.	104
Table 6.1: S_1 prism loop populations adjusted for loop loss.	150
Table 6.2: Loop normal populations.	151
Table 6.3: S_1 yield and efficiency values adjusted for loop loss.	152
Table 6.4: S_3 results adjusted for loop loss.	153

Acknowledgements.

Many thanks are due to my supervisors, Professor D.J.Bacon at the Materials Science and Engineering Department, Liverpool University & Drs C.A.English and W.J.Phythian at A.E.A Technology, Harwell for their help, assistance and advice throughout this project. Thanks are also due to my colleagues Andy Calder and Keith Tappin for their friendship and helpful contributions to the many meetings over the last three years. Special thanks are due to Yasuhide Minonishi of Tohoku University, Japan for kindly providing the titanium single crystals used in this study.

I would also like to thank everyone in ion-implantation at Harwell for their helpful advice and for performing all of the specimen irradiations. Thanks are also due to Nick Marochov, who came and went!

This project was financed by an S.E.R.C quota award with additional support from A.E.A Technology, Harwell, Didcot, Oxon.

Finally, of course a big thanks to all those who have served at Valley Parade for keeping me amused and sane when things went wrong. Come on City!

Chapter 1

Introduction.

Despite the prevailing unfavourable climate for nuclear power generation in the United Kingdom, the need for development of this industry is still a great one. Fossil fuels by definition cannot last forever and their use must be limited in the future due to the detrimental effects these fuels have on the environment, causing acid rain and contributing to the dangerous build up of greenhouse gases. Environmentally cleaner solutions such as wind and wave power are not capable of power generation on the scale required to replace the fossil fuel industry and also entail widespread destruction of areas of natural beauty and valuable breeding grounds for some of the country's rarer species of wildlife. It is against this background that countries such as France continue to press ahead with their nuclear programme and the joint European project into developing efficient fusion power also progresses.

It is clear, however from the terrible scale of the accident at Chernobyl and earlier accidents such as that at Three Mile Island, and also from the failure of the recent plans to privatise the British nuclear industry, that great strides remain to be made before the confidence of the public at large can be won over. To achieve this, nuclear power generation must be demonstrated to be cheap and more importantly safe. Reactor designs must therefore be improved and one way forward towards this aim is the search for new materials capable of withstanding the extremely hostile environment in a nuclear reactor. To help identify possible new materials we must firstly increase our understanding of the behaviour of materials in this environment to elucidate the reasons for resistance to radiation induced mechanisms such as growth, creep and void-swelling.

Towards this aim the present study has been undertaken in collaboration with the United Kingdom Atomic Energy Authority at Harwell, and forms part of their underlying research programme into materials development for the nuclear environment. Here the emphasis centres on transmission electron microscopy investigations into the effects of low dose heavy-ion implantation of a range of

hexagonal-close-packed metals. The production of vacancy loops by the collapse of displacement cascades has long been recognised to be of fundamental importance to the development of damage structures in materials subjected to a reactor environment. The driving force for studying the affects of ion implantation in a material stems from the similarities of the final defect structures observed with those noted for neutron irradiations for the vacancy component of damage. It is useful to employ this simulation method since great control is obtained over the energy, dose, temperature and damage rate incurred, whereas in a reactor producing a neutron flux these parameters cannot be readily altered. The hexagonal-close-packed system is of interest due to the technological importance of materials such as zirconium and titanium which have this structure, and display virtually a complete absence of any observed void-swelling under irradiation. Little heavy-ion implantation work has been performed on these materials despite the use of zircaloy materials as fuel cladding in present-day pressurised water reactors. The aim therefore of this study is to identify the likely behaviour of these materials in a radiation environment and to determine how the crystal structure and also a whole range of other materials parameters effect the type and quantity of damage produced.

In chapter two the present understanding of the mechanisms involved in irradiation of materials in general is reviewed and in chapter three this review is extended to the special case of the hexagonal-close-packed materials. The experimental procedures necessary to perform this investigation are detailed in chapter four and the results thus obtained are catalogued in chapter five. Chapter six involves a detailed discussion of the results obtained for the implantations in titanium, the metal on which the bulk of this study has concentrated and in chapter seven the discussion expands to encompass the whole range of metals examined. Finally in chapter eight the main successes of the work are summarised and suggestions for further work are made.

Chapter 2 Radiation Damage.

2.1 Introduction.

Interest in developing safer and more efficient nuclear power facilities continues to provide the impetus in materials science to search for new materials capable of withstanding the extremely hostile environment present at the core of a nuclear reactor. In fission reactors, neutrons of up to 2 MeV are produced and core components such as fuel cladding can achieve temperatures of up to 700° C. For fusion reactors, fast neutrons of up to 14.1 MeV are produced in the D-T reaction and this is coupled with plasma temperatures exceeding 10⁸K. These fast neutron fluxes and high temperatures can have a severely deleterious effect on the surrounding wall and construction materials of the reactor, causing void swelling, creep and other damaging phenomena. In the search for new materials capable of coping with these environments, there is continued interest in the hexagonal-close-packed (h.c.p) metals such as zirconium, which is already used as fuel cladding in water cooled reactors, and titanium. These materials are known to be resistant to neutron-induced void swelling (Yoo, 1973 and Jones, 1980 respectively) even at elevated temperatures, although the reasons for this remain unclear.

In this chapter the basic processes which cause radiation damage will be outlined and the existing theories for explaining observations of irradiated materials will be briefly considered, together with the relation between cascade processes and the resultant observed macroscopic changes in the material properties due to the occurrence of point defects and transmutation products, including such changes in bulk properties as void swelling, irradiation induced creep and growth, and segregation effects. The nature and role of heavy-ion simulation experiments in investigating these material characteristics will also be considered.

An energetic particle such as a fast neutron will produce cascades of displaced atoms on incidence with a lattice. In a reactor environment a neutron will collide with a lattice atom and in so doing will transfer some of its energy to this atom, known as the primary knock-on atom (p.k.a). Both the neutron and the p.k.a will continue through the lattice displacing more atoms, the neutron going on to produce many p.k.a's. Note that the neutron transfers varying amounts of energy and glancing collisions will occur where energy is lost but few point defects are produced. Since, for energies in the keV range, the probability cross section of collision for the p.k.a increases as the particle slows down, large numbers of atoms are displaced in a comparatively small volume before the p.k.a comes to rest, and thus each p.k.a results in the production of high densities of point defects in a small area. This phenomenon is known as a displacement cascade, and results in the production of Frenkel pairs, that is a vacancy (missing atom) and an interstitial (extra atom). These displaced atoms have a profound effect on the bulk properties of the irradiated material, since the radiation-induced microstructure can result in changes in both the dimensional and mechanical properties of the material. Vacancy production is known to be of particular importance since at sufficiently high temperatures vacancies can migrate through the matrix and cluster into three dimensional cavities known as voids, leading to the macroscopic phenomenon known as void swelling, assuming that additional sinks exist to attract the interstitials. At lower temperatures point defects are known to agglomerate into platelets of vacancies and interstitials known as dislocation loops and possibly also more complicated structures such as stacking fault tetrahedra, depending on the crystal structure.

The extent of the damage produced in the crystal lattice is determined by the primary collision event i.e the amount of energy transferred to the p.k.a. The mass, type and energy of the particles involved will govern whether the collision is elastic or inelastic. In elastic collisions, where energy is conserved, atomic

displacements occur and classical mechanics may be applied, simply treating the situation as a two body collision. For an elastic collision the primary recoil energy E_p is given by:

$$E_p = \frac{4M_1M_2\sin^2\left(\frac{\phi}{2}\right)E_1}{(M_1+M_2)^2} \quad (2.1)$$

where:

E_1 = projectile energy

M_1, M_2 = projectile and target masses respectively

ϕ = recoil angle

Notice that E_p will be at its maximum for head on collisions.

However for the case of high energy electrons, considered here to determine whether transmission electron microscopy (T.E.M) analysis will in itself produce displacements, relativistic effects become important and since $M_1 \ll M_2$ an approximation can be made (Thompson 1969) giving:

$$E_p = \frac{2E_1(E_1 + 2M_0c^2)\sin^2(\theta_1/2)}{M_2c^2} \quad (2.2)$$

where:

θ_1 = projectile scattering angle c = speed of light M_0 = rest mass of electron

From these equations we can calculate that for a titanium target, a 2 MeV fission neutron can transfer up to 160 keV to the p.k.a, and a 200 keV electron can transfer up to 9 eV, which is significantly smaller than the energy required to displace an atom from its lattice site (~ 25 eV in titanium). For inelastic collisions, kinetic energy is lost to the electrons (and transmutations can also occur), and thus in any attempt at simulation of the course of an incident particle allowance must be made for this continuing energy loss to the lattice.

2.2 Cascade Evolution.

Three distinct stages can be identified during the evolution of a displacement

cascade. In the initial phase an incident neutron displaces the p.k.a, typically according to computer simulation in about 10^{-18} secs, the resultant p.k.a travels through the lattice as it slows down and produces a process of multiple collisions, each of which produces further knock-ons until the energy of each atom falls below $2 E_d$ (the displacement threshold energy), usually within about 10 nm of the primary event. This stage takes roughly 10^{-13} secs and is often referred to as the collisional phase, during which the vacancies and interstitials become separated due to replacement collision sequences and possibly also by other mechanisms such as channelling, (Thompson 1981). By this stage the p.k.a no longer has sufficient energy to cause further displacements and the remaining energy is dissipated as lattice vibrations or "heat". In the second stage energy dissipation through the lattice continues for about 10^{-11} secs, the kinetic energy of the cascade will drop from around 10^4 K to ambient temperature and at this stage large scale rearrangement of the lattice atoms will occur. This is known as the thermal spike phase (Seitz and Koehler 1956). In this manner the p.k.a creates several excited zones and for the high recoil energies used in this study these excited zones will overlap and essentially the entire cascade volume becomes a thermal spike. Some Frenkel pairs produced in the cascade will recombine as the atoms can easily make a few diffusional jumps at these elevated temperatures. Defect migration and impurity diffusion within the material, together with evaporation at the surface for near-surface p.k.a's, will all occur during the thermal spike phase. Notice, however, that even for the highest possible spike temperatures, the time scale involved is too short to allow for any major mass transport through diffusion to occur. However since vacancy clustering is known to occur (see next section), some mass transport, resulting in segregation of impurities etc is possible. The final stage occurs at ambient temperature, when interstitials may still be mobile and further recombination of Frenkel pairs will occur. The remaining point defects will cluster into loops or be lost to sinks. The precise mechanism by which the

vacancies cluster and then collapse to form loops is still not fully understood and is considered in detail in the next section.

2.3 Factors Affecting Cascade Collapse.

Collision processes occur in less than one full lattice vibration period and the individual cascades produced can vary greatly. Each point defect produced has a strong tendency to either recombine, cluster or escape to a sink. No fully-accepted theory as yet exists to explain cascade collapse. Briefly, the widely accepted concept for vacancy loop formation following irradiation is the thermal spike model. Here the incoming p.k.a creates a depleted zone (D.Z), where the local crystal symmetry of the specimen is destroyed. For favourable energy and mass conditions the p.k.a produces localised "melting" in this region, and heat is lost to the lattice and possibly to the electrons to enable recrystallisation to occur. The recrystallised D.Z will contain a population of arbitrarily distributed vacancies due to the removal of some interstitials from the D.Z by a variety of processes. Some of these vacancies can then agglomerate to form vacancy platelets, usually on the close packed planes. The possible questions relating to the mechanisms by which these processes occur, i.e how do the vacancies agglomerate, what are the processes producing vacancy-interstitial separation, and how quickly does recrystallisation occur, are considered in the next two sub-sections. Experimental and computer simulation evidence for this behaviour is also considered.

a.) Energy density and vacancy concentration.

Energy density effects point to the above mentioned thermal spike behaviour and show the importance of the vacancy concentration produced. Eyre and English (1982) suggest that the vacancy concentration in the cascade region must exceed 1% for collapse to occur. On irradiating gold with a range of ion species, Ruault *et al* (1979) found vacancy or interstitial loops, depending on the incident ion mass used. Thus a critical energy density θ_D^{\dagger} was postulated below which vacancy loops

would not nucleate. This critical value was set at 2 eV/atom and was also suggested to hold for copper and nickel. This begs the question, why are the interstitial loops only seen below θ_D^\dagger ? This question remains unanswered. However at θ_D^\dagger the energy density is so high that essentially all the atoms in the cascade are in motion (i.e a damage spike, Sigmund 1977) so perhaps this is the condition for vacancy loop formation. The energy density of the induced cascade will rise with atomic mass of the incident particle as a smaller volume of atoms will be affected by the cascade due to energy considerations.

b.) Vacancy migration

Interestingly, English and Eyre (1982) also speculate that for high vacancy concentrations, vacancy mobility will also be higher, possibly due to a self-induced hydrostatic tension in the cascade, which would reduce the activation volume component of the diffusion energy. Thus the cascade core will act as a strong vacancy sink due to the steep concentration gradient that will exist over the small distance of the cascade region, and this will be reduced once nucleated loops grow. The formation of large vacancy loops at 30 K (Black 1984) points to some form of directed motion of vacancies towards the cluster nucleus. Protasov and Chudinov (1982), from molecular dynamics (M.D), simulations suggest this is due to vacancy migration up thermal gradients within the cascade. This ties in with earlier work by Morning (1968) who found that vacancies are preferentially attracted towards high temperature regions. Thus the thermal spike lifetimes assume importance since long lifetimes equate to more possible migration.

c.) Lattice temperature effects.

Experiments on the ordered alloy Cu_3Au show a reduction in yield of visible loops per incident ion from 0.7 for room temperature irradiations by Jenkins and Wilkens (1976) to 0.49 for 4.2 K irradiations by Black (1984). Thus, ambient lattice temperature appears to play an important role in determining the probability of cascade collapse, indicating that thermal spike lifetime and cooling

rate are important parameters. The observation of cascade collapse at such low temperatures is of central importance since cascade collapse is thus seen to occur at temperatures well below that at which vacancies are mobile, and indeed vacancy loops have been observed for irradiations at liquid helium temperature (4.2 K) in gold, (Calder 1989), as well as in ordered alloys, (Black 1984).

d.) Quasi-melting

Quasi-melting is one currently favoured concept for explaining the mechanism by which vacancies agglomerate to form a dislocation loop on irradiation with energetic particles. From molecular dynamics simulations it is believed that during the cascade, atoms at the centre of the disordered zone have such high energy that the crystalline nature of the lattice is temporarily lost, resulting in a liquid-like region at the core of the cascade. This central region will be rich in vacancies since interstitials are carried away from the core by a variety of processes, (channelling and replacement collision sequences [R.C.S], both of which are discussed in section 2.4). The central cascade region will be rapidly quenched due to the large temperature gradients existing in the crystal and is thought to solidify from the outside in, thus sweeping forth the vacancies on a "wave" of recrystallization which carries the vacancies to the centre of the zone which then collapses to form a vacancy platelet.

In recent work by Diaz de la Rubia *et al* (1989) using Molecular Dynamics simulations (M.D) of thermal spikes in copper and nickel, 5 keV p.k.a events were generated and the radial distribution functions for the lattice calculated at various picosecond intervals. The liquid-like nature of the core of the cascade is illustrated by the temporary disappearance of the (200) peak in the distribution functions for both copper and nickel. An example of the observations made by Diaz de la Rubia *et al* is shown in fig 2.1. This quasi-melting process is described as a "zone refining" mechanism whereby the slower the resolidification process, the more efficiently the vacancies are swept together. If this is correct there will also be important

ramifications for impurity segregation in cascades. One success of this model so far is its apparent ability to explain the large difference in yields seen for copper and nickel, although of course until further corroboration is obtained this could prove to be purely coincidental. These two metals have similar masses but copper has a much higher yield and this is explained by a slower re-solidification in copper leading to more vacancy segregation to the core of the cascades. One implication of this model is that the melting point of the material must play a central role in determining the quenching of the thermal spike since high melting point materials will re-solidify far more quickly and indeed may not exhibit this quasi-melting behaviour at all. Experimental evidence to confirm a definite link between melting point and damage parameters will be sought in this study.

It should be noted that as with all computer simulations to date, Diaz de la Rubia *et al* are restricted to the low energy range up to 5 keV and this may not be representative of much higher energy primary events. It should also be remembered that the two-body potential used to simulate the behaviour of the atoms is quite primitive, requiring a positive pressure to be applied to hold the crystal together and thus these potentials are of limited use in modelling cascade events. Diaz de la Rubia *et al* stress the important role they believe is played by R.C.S events and these are discussed further in the next section.

e.) Electron-phonon coupling.

Until recently the role of the valence electrons in cascade collapse processes has been largely ignored, other than to assume that there is an additional constant energy loss due to the valence electrons as the p.k.a slows down. Recent evidence (Diaz de la Rubia *et al* 1989) that the thermal spike lifetime may be of central importance to the subsequent damage evolution has led to a reappraisal of the effects due to the electron-phonon coupling interactions.

A recent paper by Flynn and Averback (1988) shows that quenching of the thermal spike due to thermal conduction occurs over a time scale comparable to

that required for electronic thermalization and thus by neglecting the electronic contribution to the cooling process incorrect evaluations for thermal spike lifetimes will result for some metals.

It is well known that over "long" periods of time the electrons are always out of equilibrium with the lattice, however to determine whether equilibrium occurs over "short" time scales depends critically on the factor T_0 , where T_0 is the temperature at which the electronic mean free path λ is reduced to the Wigner-Seitz radius r_s , thus, assuming the electron mean free path depends linearly on T (predicted by the harmonic approximation, Flynn and Averback, 1988):

$$\lambda = r_s T_0 / T \quad \text{for } T > \Theta_D \quad (2.3)$$

Θ_D = the Debye temperature, T = the spike temperature.

Since a cascade of radius r will contain $(r/r_s)^3$ atoms we find:

$$r = r_s (Q/3k_b T)^{1/3} \quad (2.4)$$

where Q = the total energy of the system.

The number of mean free paths required to escape the cascade zone can be approximated to $(r/\lambda)^2$ and assuming that the carriers will absorb $k\Theta_D$ per collision (from classical energy transfer equation) then the effective local temperature of the carriers reaches:

$$T_{\text{eff}} = \Theta_D (r/\lambda)^2 \quad (2.5)$$

By equating T to T_{eff} in equations (2.3)-(2.5) we find that electronic equilibrium is obtained for radii smaller than a critical value r_c :

$$r_c = r_s \Theta_D Q / 3k_b T_0^2$$

when the temperature will have cooled to:

$$T_c = 9T_0^6 / \Theta_D^3 (Q/k_b)^2 \quad (2.6)$$

Thus the critical temperature depends on T_0^6 and is proportional to λ^6 . Metals as similar as copper and nickel turn out to have extremely disparate critical temperatures. Nickel has a very low critical temperature (300 K) and therefore achieves electronic equilibrium throughout the duration of the spike. Thus the

temperature of the thermal spike is moderated as heat conduction out of the cascade region is improved.

To determine the size of the effect of the electron-phonon coupling requires comparison of the electron mean free path in the liquid metal to the dimensions of the cascade. Electron mean free paths can be smaller than the cascade radius and in such metals electron-phonon coupling is expected to play an important role as heat can be lost to the valence electrons. Maximum spike temperatures can be drastically reduced due to the additional heat capacity of the electron system. Metals expected to have strong coupling (e.g iron) do not show strong spike effects in radiation damage experiments, which is a good pointer that this effect is playing an important role.

f.) Stacking fault energy.

Considerable experimental evidence points to the stacking fault energy playing an important role in determining the amount of damage present in the irradiated material. This seems sensible since a material with a high stacking fault energy will require more energy to disturb its perfect stacking order, while low stacking fault energy materials will more easily transform to an alternate local packing. It should be noted, however, that the stacking fault energy is by no means a hard and fast guide to the amount of damage likely to be induced in the material.

g.) Vacancy-interstitial separation.

Finally, the vacancy-interstitial separation is obviously of great importance in determining whether recombination takes place. In one theory, (Wilkins 1975) this separation is thought to be related to the ratio l_i/R_c where l_i is the R.C.S length and R_c is the cascade radius. Instinctively this would seem to have some relation to the final quantity of damage present as large R.C.S lengths will remove interstitials beyond the cascade radius. Note that R.C.S lengths will be influenced by crystallography, lattice temperature and purity. The crystallographic effects will now be considered in more detail.

2.4. Crystallographic effects

Since all the materials irradiated in this study are crystalline rather than amorphous, as is sometimes assumed in theoretical calculations to simplify the mathematics, it is reasonable to assume that this will have an effect on the resulting damage. Two processes are known to be of particular importance; R.C.S and channelling. The R.C.S lengths are important since they clearly play a major role in determining the rate of defect survival. Channelling is considered in detail since it is desirable to tailor the experimental procedure to the effect that this phenomenon is kept to a minimum.

2.4.1 Replacement Collision Sequences (R.C.S)

Despite having been postulated for over thirty years, R.C.S events remain one of the most contentious areas in the field of radiation damage. Indeed, many worthy attempts at explaining the fundamentals of cascade collapse have foundered due to lack of information on R.C.S lengths. For instance results as disparate as 50 Å (Ecker 1974) and 2000 Å (Seeger 1970) have been reported for R.C.S lengths in gold. Historically, Silsbee (1957) was the first to propose that below some critical energy both mass and energy can be transferred along the close-packed directions of a crystal lattice by the process now known as R.C.S. A simple description of R.C.S is as follows: Energy (or mass) can be transferred along the close packed directions by "snooker-ball" type interactions between the atoms. Each atom in the chain displaces the next atom along, while the direction of the R.C.S is kept "focussed" by the surrounding atoms. Eventually the energy transferred to an atom will be less than that required to displace the next atom and the R.C.S will end by depositing a self-interstitial atom (s.i.a) at the end of the sequence. Thus the important net effect is to separate a vacancy (left at the start of the sequence) from an interstitial by a large enough distance to ensure recombination does not take place. In favourable (close-packed) directions little

energy is lost per collision so the R.C.S may extend over many atomic spacings. Any irregularities in the crystal lattice such as dislocations or impurities will effectively reduce the R.C.S length by interrupting the sequence. If only energy is transferred along the row of atoms but overall no atomic displacements occur, this is known as a focousson, and this is important since energy can thus be removed from the cascade without the creation of any Frenkel pairs.

Molecular dynamics (M.D) computer simulations of R.C.S events to date reveal that this phenomenon is of greatest importance at energies in the range 50-500 eV e.g Erginsoy *et al* (1964,1965). Due to this low energy nature, R.C.S events are of particular importance around the periphery of the cascade region where many low energy collisions will occur. It should, however, also be considered that at these low energies channelling can also play an important role since the channelling angles grow markedly at low energies (see next section). Thus interstitial transport away from the cascade region may occur between the close packed planes rather than along them.

Several attempts have been made to quantify the lengths of R.C.S's in various materials and with varying degrees of success. A recent study by Bullough (1987) attempted to measure R.C.S lengths in copper and molybdenum at low energies and at low temperatures. By irradiating at 4K down the [011] direction and measuring the depth distribution of the interstitial loops produced it was hoped to find a twin peak corresponding to the R.C.S lengths along the close-packed directions. No long-range (i.e > 200 Å) events were detected and channelling effects proved difficult to rule out for the distributions observed. In an earlier study Hertel (1980) had concluded that R.C.S lengths along the <011> directions in copper had a mean range of roughly 180 Å. Wei and Seidman (1980) using field ion microscopy (F.I.M) determined the mean separation between the cascade core and the s.i.a's produced to be 175 Å in tungsten. However doubts exist as to the applicability of F.I.M results to bulk materials. Overall, computer simulation seems to predict much shorter

lengths than those found by experimental methods. For instance, Tenenbaum (1978) using M.D found R.C.S lengths equivalent to only 15 atomic replacements i.e about 40 Å. The interaction potential used in the M.D code is one possible reason for the discrepancy, but it is clear that very little confidence can be attached to any estimate so far obtained for R.C.S lengths.

2.4.II Channelling

Stark (1912) first proposed the idea that the penetration of a crystal by an incident particle will be affected by the orientation. Incident particles can travel over extended distances through the lattice in the "open" channels that exist between close-packed planes. The projectile is guided along through the lattice by a series of glancing collisions with the close-packed planes. This phenomenon is of particular importance since by this process energetic atoms can travel large distances from the initial cascade region before colliding with a lattice atom and thus creating distinct sub-cascades. Hence irradiation with one heavy ion may result in the observation of more than one visible dislocation loop. This effect is of great importance, therefore, in considering the observed defect yield (discussed later). Experimental confirmation of this phenomenon came from Nelson and Thompson (1963), who studied the intensity of transmission of a proton beam through thin gold foils. The theoretical proton beam penetration was calculated and foils were then machined to a thickness corresponding to the limits of penetration, assuming an amorphous foil. Transmitted currents, however, were found to be as much as ten times higher along the close packed <110> directions in comparison to a non-aligned direction.

Thompson (1969) showed that channelling can be successfully modelled using classical mechanics. The angular width Ψ_0 of the channelling direction (the width off-axis at which channelling effects have fallen by 1/e) is found to be proportional to $(M_1 M_2)^{1/2}$ and decreases at higher energies. An energy minimum has been found to exist below which channelling will not occur-usually at a few

hundred eV.

In the present and many earlier fundamental studies, heavy-ions have been used to simulate the individual cascades produced in neutron irradiations, and this will be considered in detail in section 2.5. Channelling is of great importance in heavy ion damage studies for three reasons:

- 1) Some incident ions may pass straight through the foil, hence lowering the amount of damage seen in comparison to bulk specimens. It is therefore important to perform irradiations "off-axis" as described in chapter 3 to reduce this effect.
- 2) Sub-cascade formation will be encouraged due to the possibility of highly energetic secondary knock-on atoms being channelled some distance away from the original cascade region and thus creating a second depleted zone
- 3) Defect production will be reduced due to the energy loss without displacement which is characteristic of the channelling events, and hence less energy is available for the production of Frenkel pairs.

Various theoretical attempts have been made to estimate the number of ions channelled in a solid and for a more in-depth discussion of channelling, reference should be made to Gemmel's excellent and extensive work (1974). According to Lindhard (1965), when an ion passes within a certain angle $C\Psi_c$ (where $1 < C < 2$) of a row of atoms the beam is effectively divided into two components, a random part for which we can assume an amorphous target and a channelled part. Lindhard identifies two channelling regimes. At high energies he estimates the critical angle to be:

$$\psi_1 = \left(\frac{2Z_1Z_2e^2}{dE} \right)^{\frac{1}{2}} \quad (2.7)$$

where Z_1 and Z_2 are the masses of the target and projectile atoms, and d is the planar spacing. For low energies the Thomas-Fermi atomic model is employed and thus

$$\psi_2 = \left(\frac{Ca}{d\sqrt{Z}} \psi_1 \right)^{\frac{1}{2}} \quad (2.8)$$

where $C = 3$

A study by Cairns *et al* (1972) on measuring the critical angle for channelling of heavy ions in copper using X-ray techniques found good agreement with the more generalized equation due to Wijngaarden (1969) which used an inverse square power law, fitted to the screened Coulomb potential giving:

$$\psi_c = \left(\frac{a}{2.71d} \psi_1^2 \right)^{\frac{1}{3}} \quad (2.9)$$

where a is the Thomas-Fermi screening radius:

$$a = \frac{0.8853a_0}{\sqrt{Z_1^{2/3} + Z_2^{2/3}}} \quad (2.10)$$

This is applicable over a large range of energies and is especially accurate for the lower energies considered in this study. The equations detailed above will be utilized later to determine the critical channelling angle for all of the metals examined.

Finally, as with R.C.S events, channelling can be severely curtailed by thermal lattice vibrations and any lattice imperfections i.e dislocation loops, s.i.a's and misfit impurity atoms which will partially or completely block channels, as will stacking faults (Schober and Balluffi 1968). Therefore, channelling effects will be dose-dependent, reducing as the dislocation density rises (Nelson and Thompson 1963). Channelling is usually considered to be a high energy effect, and at low energies (1 keV or less), channelling will not be noted. One interesting effect noted by Gemmell (1974) is that for molecular ions, channelling effects tend to be reduced: this is in direct contradiction to T.E.M observations for molecular-ion irradiations and will be considered in the discussion chapter.

2.5 The Suitability of Heavy-Ion and Near Surface Studies

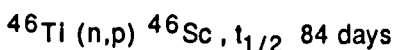
Mid-energy (50-150 keV) heavy ions have been used exclusively throughout this study to simulate the energetic recoils produced by neutron damage in a nuclear reactor environment. The range of these ions is typically a few hundred angstroms, and so the irradiations have been performed on thin (~ 1000Å) foils in which the damage can be observed directly using T.E.M. The question arises as to just how applicable these simulations are to the bulk effects produced on the material by neutron damage. Several differences must be considered when trying to extrapolate from the data produced by heavy ion simulations.

1.) The interstitial component of the damage produced by heavy ion irradiations is rarely observed since the close proximity of the foil surface acts as a very strong interstitial sink and interstitials will be mobile at room temperature. Also, the relatively low doses used in heavy ion studies compared with in-situ neutron irradiations generally precludes the possibility of large scale interstitial aggregation to form stable loops.

2.) Vacancy loops may be lost to the surface by glide (glissile loops) or, more rarely, by climb (glissile and sessile loops), reducing the apparent defect density in comparison with bulk studies.

3.) Vacancy-interstitial recombination will be greater in neutron irradiated materials since cascades are generated throughout the bulk of material whereas for near surface studies interstitials may be lost to the surface rather than recombine.

4.) As well as atomic displacement damage, neutron bombardment also produces transmutations, for instance in titanium:



This behaviour is not mirrored in the low dose heavy ion simulations which is beneficial since transmutation products are usually radioactive, rendering direct study of neutron damage difficult and time consuming. Transmutations commonly produce helium which is of specific importance due to its ability to stabilize voids

in the lattice. However, for heavy ion irradiations at these low doses and without additionally implanted gases to help stabilize the voids we would not expect void production. It should also be noted that these transmutation products will generally result in detrimental changes to the reactor constructional materials.

5.) Neutron irradiations are expensive and difficult to control, whereas for heavy ion experiments the ions are implanted at one distinct energy. Also, neutron irradiations can only be performed for a full spectrum of energies, thus complicating the interpretation of the results obtained.

In a rigorous study by Muncie et al (1985), results obtained from irradiating single crystal copper in the materials test reactor PLUTO were compared with earlier results obtained by Stathopoulos (1980) and English et al (1976) for heavy ion irradiations of similar material. It was found that all the anomalies between the neutron irradiated and heavy ion bombarded copper could be attributed to the differences mentioned above leading to a net reduction in loop size and density for comparable doses of neutrons to those obtained for heavy ions.

Kinney and Guinan (1982), in a paper comparing the results of computer simulation using the BURST code (see Guinan *et al* 1977) with F.I.M studies in tungsten, found that for defects lying within one R.C.S length (the maximum lengths observed in this study were 35 Å) of the surface, significant reductions in the displacement energy (E_d) occurred along the $\langle 111 \rangle$ close packed directions, thus affecting the resultant near surface damage. A total absence of interstitials was also noted within two R.C.S lengths of the surface, leading to a corresponding increase in vacancy loop size of up to 20%.

Allowance can be made for the energy spectrum effects of neutron irradiation by assigning some threshold energy below which an incident neutron will not produce a visible loop. Taking a realistic value of around 8 keV for the resultant p.k.a's (obtained by extrapolating from Stathopoulos's data on minimum loop size and allowing for the effects of increased vacancy-interstitial recombination in bulk

samples), we find that the neutron and heavy ion bombarded copper results are actually in very good agreement. So we can conclude that heavy ion experiments are relevant to reactor environment studies.

2.6 Cascade Quantification

In considering the initial cascade produced in the lattice with respect to the final damage structures observed in the electron microscope, it is of primary importance to have a reliable quantitative estimate for the number of Frenkel pairs initially produced by the incident ion. The seminal work of Kinchin and Pease (1955) provides a good starting point for any estimate of the amount of damage produced by the p.k.a event. By assuming hard sphere interactions between atoms and by postulating a threshold energy (E_d) below which no displacements would occur, they derived an expression for the number of Frenkel pairs produced:

$$N_d = \frac{E}{2 E_d} \quad (2.11)$$

where E is the p.k.a energy. From Sigmund's (1969) theoretical calculations a factor k (roughly 0.8) is usually inserted to modify this equation from a hard sphere model to allow for energy losses to the lattice. In fact k is known to vary for energies below 10 keV but for the energy range of interest in this study k can be considered energy independent.

Nelson (1969) modified this equation further by incorporating several correction factors to obtain a more realistic approximation for the atomic scattering processes. The stopping power theory of Lindhard *et al* (1963) was utilized. Electronic losses [$W(E)$] were assumed important only for the p.k.a. The threshold energy was calculated as E_f , the threshold for R.C.S events rather than E_d and also a factor allowing for defect recombination [$\beta(E)$] was included, although this is usually set equal to one, giving:

$$N_d = \frac{\alpha \cdot \beta(E) \cdot W(E) \cdot E}{\gamma(E) \cdot E_f} \quad (2.12)$$

where $\gamma(E)$ here corresponds to the factor 2 in the Kinchin-Pease model. Since Beeler (1966) noted from cascade calculations that γ tends to rise for higher energies, possibly due to overlapping of cascades, the parameter γ can be varied for higher energy irradiations, but this is not necessary for the energy range considered in this study.

Computer simulations have been used by many workers to track the course of a p.k.a through the lattice. Torrens and Robinson (1974) constructed a simulation in which the trajectories of the displaced atoms conformed to a sequence of isolated binary collisions. Using a threshold energy E_d , any collision transferring more energy was added to the cascade. Temperature effects were accommodated by giving each atom a random Gaussian displacement following the Debye model. Inelastic energy losses were incorporated using a modified version of Firsov's model (1959).

Thus they found:

$$N_d = \frac{k(E-Q)}{2E_d} = \frac{kE'}{2E_d} \quad \text{for } E' > \frac{2E_d}{k} \quad (2.13)$$

where Q = energy lost due to electron excitation and therefore E' = available damage energy. Thus equation (2.13) is analogous to the half-Nelson equation.

Obviously to facilitate easy comparison of the results of various workers it is desirable to have an international standard for calculating N_d . Norgett, Robinson and Torrens (1975) proposed a procedure based on the above method for calculating N_d , and as such it provides an International standard. E_d was set at 40 eV, the experimentally confirmed value for b.c.c iron. This value was chosen since at the time (1975) iron was the only material for which extensive M.D results were available, and it is still widely used since it provides a good first estimate for most metals and E_d is known to vary slightly with crystal orientation so a precise figure for each material is difficult to obtain. It should be noted that this represents a mean displacement energy rather than a minimum so as not to result

in an overestimate of the damage produced. A numerical approximation was given relating E' to E utilizing the universal function $g(E)$ due to Robinson (1970) as follows:

$$E' = \frac{E}{1 + k.g(E)} \quad (2.14)$$

Where: $g(E) = 3.4008E^{1/6} + .40244E^{3/4} + \epsilon$

$$k = 0.1337 Z_1^{1/6} (Z_1/A_1)^{1/2}$$

$$\epsilon = \left(\frac{A_2 E}{(A_1 + A_2)} \right) \left(\frac{a}{Z_1 Z_2 e^2} \right)$$

$$a = \left(\frac{9\pi^2}{128} \right)^{1/3} a_0 (Z_1^{2/3} + Z_2^{2/3})^{-1/2}$$

a_0 = Bohr radius e = electronic charge

Z_1, Z_2 = projectile and target atomic numbers respectively.

A_1, A_2 = projectile and target mass numbers respectively.

Substituting the relevant numbers for iron we arrive at the final internationally accepted standard of:

$$N_d = 10 E', \text{ where } E' \text{ is in keV} \quad (2.15)$$

It should be noted that this model is only strictly accurate for $M_1 = M_2$ and for energies much less than $25 M_1^{4/3} A_1$ keV (i.e 572 MeV for the antimony ions used here). The disparity between M_1 and M_2 will not be too detrimental to the accuracy of the equation as long as the ratio $M_1 : M_2$ does not stray too far from unity.

More recently Biersack and Haggmark (1980) developed a Monte-Carlo style simulation named "the TRansport of Ions in Matter" (TRIM) which is growing in popularity. Originally developed for determining ion ranges and damage depths, comparison with experimental results confirms that the program works well from 0.1 keV up to several MeV. This Monte-Carlo approach has the advantage over earlier analytical techniques in that a more rigorous treatment of elastic scattering

is possible and explicit consideration of the surface can be made. The p.k.a undergoes binary nuclear collisions losing energy through nuclear and electronic energy losses and each p.k.a. history ends either at the injected surface or at a pre-specified energy threshold. Relativistic effects are not considered and hence there exists an upper energy bound to accuracy. To simulate the increase in capture cross section as the particle slows down the free flight path between collisions is reduced as the particle loses energy.

This programme is unique in being able to handle both high and low energy particles by utilizing the Moliere (1947) interatomic potential for low energies, where nuclear scattering and energy loss is particularly important, and the un-screened Coulomb potential is used at high energies. The interpolation scheme of Biersack (1975) is used to bridge the gap between the two energy regimes.

2.7. Experimental Cascade Observations.

T.E.M has been used exclusively throughout this study to observe dislocation loops produced from displacement cascades. It is worth noting however that another technique, field-ion microscopy (F.I.M) exists for the direct observation of displacement cascades in crystals. The important aspects of these methods are briefly discussed here.

2.7.1 Field Ion Microscopy.

This is the only technique at present capable of studying individual displacement cascades atom by atom. The specimen used is a fine wire, electropolished to produce a sharp hemispherical tip, which is further sharpened in the microscope to a radius of 5-100 nm by field evaporation. This utilizes a high electric field (typically 100 V/nm) to remove atoms from the surface tip. Observations and micrographs are made between each pulse of the field evaporator. One experiment can typically involve up to 5,000 micrographs, these are then analysed to provide a 3-D picture of the region of interest. Magnifications of

around 10^6 times are generally achieved using this method. (For a full review reference should be made to Seidman, 1973).

There are however several disadvantages involved in using F.I.M

- 1.) High melting point materials are generally the easiest to analyse (commonly tungsten and platinum) and sample preparation is difficult.
- 2.) Up to 5,000 micrographs are taken for each sample making analysis very time consuming.
- 3.) Only individual cascades are studied so dose effects cannot be analysed.
- 4.) Surface effects can be quite considerable (see Kinney and Guinan, 1982) and only very small volumes of the metal can be examined which may not necessarily be representative of the whole sample.
- 5.) The high voltages involved in stripping off atoms from the tip may in itself cause damage and thus influence the results.

However F.I.M studies remain the only method available for observing individual point defects in a cascade and the technique has been successfully applied to confirm some important trends in the field of radiation damage:

- 1.) The number of vacancies per depleted zone is in good agreement with theory for varying projectile mass and energy and is virtually independent of mass.
- 2.) The diameter of the depleted zone decreases with increasing projectile mass, and thus the vacancy concentration increases.
- 3.) The probability of sub-cascade formation increases with increasing energy.
- 4.) The spatial distribution of vacancies is strongly dependent on the projectile mass.

This behaviour is as predicted from computer simulations, thus confirming that F.I.M is a useful analytical tool despite the limitations outlined above.

2.7.II Transmission Electron Microscopy (T.E.M) observations

Throughout this study, the samples used are in the form of 3 mm discs electropolished to produce wedge shaped foils of thickness less than $1,000 \text{ \AA}$ so that

electron transparency is achieved. Observations of the damage produced by the incident ion are limited to the final stable dislocation configurations produced. It is however possible in the case of ordered alloys to gain information on the dimensions of the cascade region by employing superlattice reflections to image the induced disorder (Jenkins *et al* 1976). The advantages offered by T.E.M are that large numbers of defects can be fairly rapidly analysed, most materials are amenable to the sample preparation techniques and surface effects are less important compared to F.I.M.

T.E.M observations to date have helped to build up the following picture of irradiation damage. Following recombination the remaining vacancies can aggregate in collapsed platelets forming faulted Frank loops on the close packed planes of the lattice. If the stacking fault energy (S.F.E), and size of the loop are such that it is energetically favourable, these loops can unfault to form perfect loops, i.e loops without an associated stacking fault.

2.7.III. Observations of Defects In Varying Crystal Systems.

At this stage it is useful to introduce the concept of the Burgers vector of a dislocation loop. The Burgers vector simply gives a measure of the material added or removed from the perfect crystal. In this study two types of vacancy loops will be observed. For an edge dislocation the Burgers vector is normal to the line of the dislocation. The dislocation loops seen in this study are noted to vary from pure-edge to 30° non-edge. Perfect Burgers vectors are those which correspond to a lattice translation vector. Faulted Burgers vectors result in a change in the stacking sequence of the planes of the crystal and thus have an associated stacking fault. For a more detailed review of dislocation notation reference should be made to Hull and Bacon (1984).

In face-centred-cubic (f.c.c) metals collapse is noted to be readily produced and correspondingly high yield and efficiency values are observed. Much work has been performed on copper (McIntyre 1967, Rühle 1969, Stathopoulos 1980), and

other f.c.c materials investigated appear to behave in a broadly similar fashion (although yields may vary considerably, c.f copper and nickel). Faulted loops with Burgers vector $\mathbf{b} = 1/3 \langle 111 \rangle$ are observed and for the high S.F.E f.c.c materials such as nickel (Eyre *et al* 1977) these can unfault to $\mathbf{b} = 1/2 \langle 110 \rangle$, whereas for a low S.F.E material such as silver (English *et al* 1980) the loops may dissociate on the {111} planes forming tetrahedral structures. Impurities were noted to dramatically reduce the defect yield in aluminium (King *et al* 1970), where high purity (99.9999%) aluminium exhibited resolvable loops after exposure to $3.5 \times 10^{20} \text{ n/m}^2$, but commercial purity aluminium irradiated to the same dose exhibited no visible damage.

For body-centred-cubic (b.c.c) metals a different picture has emerged, for much lower yields and efficiencies are observed and for the extreme case of self-irradiated iron no damage at all is observed (Jenkins *et al* 1978). Due to the high S.F.E of these materials, very few faulted loops have been observed and commonly only the perfect loops with $\mathbf{b} = 1/2 \langle 111 \rangle$ and $\mathbf{b} = \langle 100 \rangle$ are seen. Since these loops are glissile, the observed defect yield may be reduced by loop loss due to glide to the surface if \mathbf{b} has a component perpendicular to the direction of the foil surface. This effect must be taken into consideration when defect yields are compared. Mastell and Brimhall (1965) found an increase in carbon content enhanced defect formation, while a more recent study by English *et al* (1977) noted that for molybdenum doped with a very small amount of nitrogen (17 appm) the yield fell by a factor of five, and a similar effect was noted for f.c.c materials, where a comparison of type 321 stainless steel with a ternary alloy of similar composition, (Robinson and Jenkins 1981) revealed a much lower yield for the high impurity content 321 steel. On irradiation with high energy molecular ions, "craters" are observed in molybdenum (English *et al* 1987), and these were noted to be mostly over 7.5 nm in diameter and faceted irrespective of irradiation orientation. These craters were found to occur more frequently for higher

irradiation temperatures. This phenomenon as yet appears to be unique to the b.c.c case.

The precise form of damage found in hexagonal-close-packed (h.c.p) systems will be considered in detail in the next chapter. Both faulted and perfect loops have been observed due to the large range of S.F.E's that exist for these metals. These loops have been observed mostly but not exclusively on the most densely packed planes, and thus the c/a ratio is obviously an important parameter to be considered for these materials.

The interstitial component of damage is usually not seen at low doses in near-surface, heavy-ion studies since the surface acts as a strong sink for interstitials which are mobile at much lower temperatures than vacancies. Hence interstitials are mostly lost to point defect sinks, though some may agglomerate to form small loops at high damage doses.

Merkle (1976), studying cascade collapse in gold, found the fraction of cascades which collapse to form vacancy loops tended to increase more or less linearly for irradiations up to a threshold of 40 keV, at which point the fraction became unity, implying each incident ion produces a cascade which then collapses to produce a visible vacancy loop. Above this threshold the fraction increased beyond one implying that sub-cascades are being formed, that is some incident ions are producing more than one cascade. These sub-cascades are thought to arise due to secondaries channelling away from the main cascade for a significant distance before being de-channelled and producing a second dispersed zone. This effect has also been found in silver by Lyle and Merkle (1975) and has been confirmed in gold by several other workers. Evidence for sub-cascades also comes from many computer simulations e.g Beeler (1974). Heinisch (1983) calculated that the cascade extent for any high energy p.k.a. could be regarded as equivalent to the superposition of several low energy cascade regions. In an interesting recent paper Rossi *et al* (1988) applied the new mathematics of fractals to a cascade event and

these accurately mirrored the events occurring in a depleted zone particularly with reference to the onset of sub-cascade formation. The size of the cascade as a function of ion mass and energy was also found to be in good agreement with experimental data. The fractal approach shows the threshold for sub-cascade formation can be expected to increase with target mass but it should be noted that the mathematics only hold fully for the case of self-ion irradiations.

2.7.IV. Yield and Efficiency Trends Observed.

By varying the ion type, mass and energy, a variety of cascades of widely varying size, energy density and vacancy concentration can be produced, and one of the most important questions to be investigated is, how does the resultant vacancy loop size and density vary with incident ion mass and energy over the full range of metals? This will be a good guide to the total amount of damage produced in the foil. The following points have emerged:

- a.) The dislocation loop density at constant dose is seen to rise as the incident ion mass rises. This is most probably due to the higher energy/vacancy density achieved due to the reduction in cascade size with increasing ion mass.- e.g Jenkins (1978)
- b.) Interestingly, the yield of visible loops increases for molecular ion irradiations in comparison to single ion runs (Jager and Merkle 1981, English 1981). Taken together with the F.I.M work of Pramanik and Seidman (1983), who looked at single and molecular self ion irradiations of tungsten and found larger (but not twice as large) depleted zones for the case of the W_2^+ irradiations, this provides strong evidence for the overlap of molecular cascade regions, leading to a higher vacancy concentration and hence an increased cascade collapse probability.
- c.) Stathopoulos's (1980) exhaustive study on copper confirms the general trend that defect size and hence vacancy retention efficiency increases for an increase of the irradiation ion mass. This will again be due to an increase in the average energy density over the cascade region.

d.) As the incident ion energy increases the yield of loops increases in a non-linear fashion. This is due to the existence of a threshold to the onset of visible damage and also the onset of subcascade formation (Phythian 1985).

e.) As the incident ion energy increases the vacancy retention efficiency in each loop decreases (Hausserman 1972). However the yield rises more rapidly than the efficiency decreases so a net rise in the number of vacancies in the foil is observed with increasing ion energy.

2.7.v Temperature Effects.

As noted earlier, ambient lattice temperature will affect the final damage structures observed. English (1976) found that the defect yield began to fall in copper as the irradiation temperature rose above 300 °C and this was attributed to loop shrinkage due to thermal emission of vacancies at elevated temperatures. However turning to the case of molybdenum, English (1977) found that the defect yield begins to decrease above 150-200 °C, while loop shrinkage due to vacancy emission is not possible in molybdenum until 700-800 °C. There is therefore a strong temperature dependence for collapse in molybdenum. Experiments on an ordered alloy Cu₃Au show a reduction in yield of visible loops per incident ion from 0.78 for room temperature irradiations by 100 keV Kr ions to 0.52 for 4.2K irradiations by Black *et al* (1986). This trend was noted for a variety of ion masses and energies, thus ambient lattice temperature appears to play an important role in determining the probability of cascade collapse.

2.8 Summary

It can therefore be said, that while no absolute understanding as yet exists, various materials parameters play a large role in determining the type and amount of damage observed as a result of displacement cascade production. The yield of collapsed cascades in the form of vacancy loops is dependent on a variety of factors, as follows:

a.) Mass number

High mass may contribute to a higher yield, since higher energy density cascades will be produced due to atoms being displaced in a smaller volume.

b.) Melting point

It has been proposed that rapid resolidification within cascades leads to lower yields

c.) Energy density.

High density leads to higher yields due to compact cascades and longer R.C.S's.

d.) Stacking fault energy.

Lower stacking fault energy has been noted to result in higher yields.

e.) Lattice temperature.

High ambient lattice temperature means slower cooling and thus higher yields.

f.) Electron-phonon coupling

This can result in rapid cooling and lower thermal spike lifetimes, and thus lead to lower yields.

g.) Crystallography

The crystalline nature (large/small grain or single crystal) and the crystal structure will have a pronounced effect on the type and quantity of defects observed and this will be considered in more detail for the h.c.p case in the next chapter.

None of these trends are definitive and it is obvious that a combination of these effects plus perhaps other as yet undiscovered ones are at work. It is clear that more research is needed in this field to elucidate our understanding of the damage mechanisms.

3.1 Introduction.

As discussed in the previous chapter, much attention has been focused on the region of the h.c.p. material with disordered atoms while the work has been done on the h.c.p. material, under the systematic study of random structures by Phyllis (1965, and Phyllis *et al* 1987, 5, 1988). With the continued quest

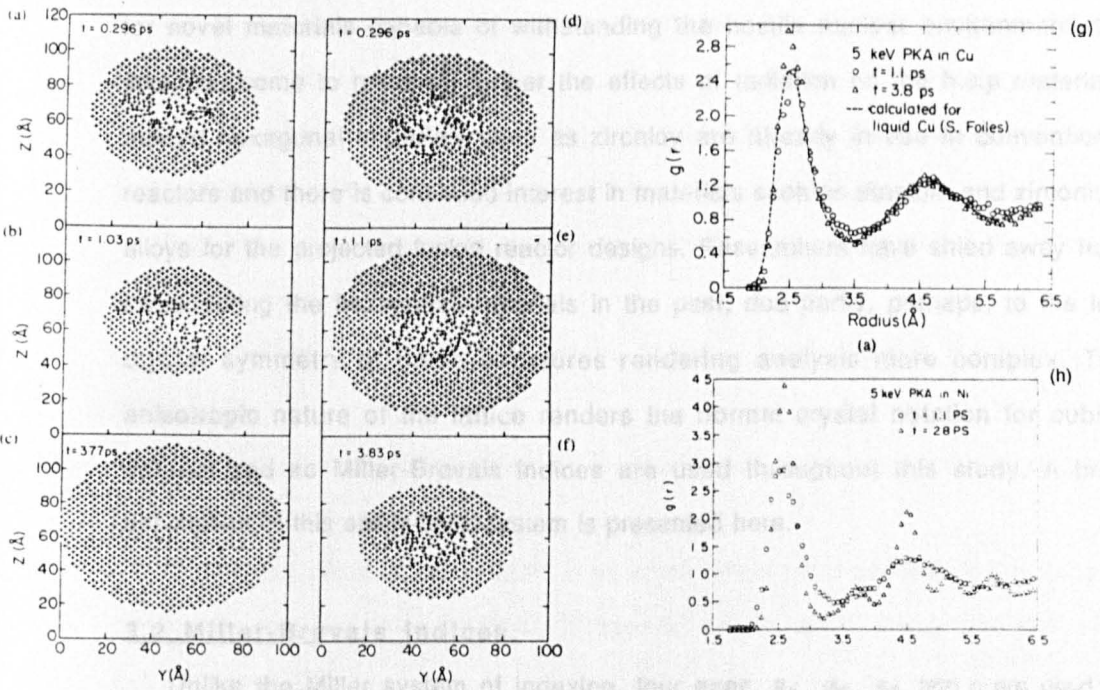


Fig 2.1: (100) projection of the atomic configurations observed near the centre of 5 keV simulated cascades in Ni (a-c) and Cu (d-f) at various times and the associated disordered-zone radial pair distribution functions for Cu (g) and Ni (h), showing liquid-like behaviour. Reproduced from Diaz de la Rubia *et al* (1989).

Chapter 3 H.C.P Materials.

3.1 Introduction.

As detailed in the previous chapter, much attention has been focussed on the reaction of cubic materials to irradiation while comparatively little work has been done on the h.c.p materials, other than the systematic study of ruthenium undertaken by Phythian (1985, and Phythian *et al* 1987, & 1990). With the continued quest for novel materials capable of withstanding the hostile nuclear environment, the time has come to research further the effects of radiation on the h.c.p materials. Indeed hexagonal materials such as zircaloy are already in use in conventional reactors and there is continued interest in materials such as titanium and zirconium alloys for the projected fusion reactor designs. Researchers have shied away from investigating the hexagonal materials in the past, due partly, perhaps, to the low crystal symmetry of these structures rendering analysis more complex. The anisotropic nature of the lattice renders the normal crystal notation for cubics defunct and so Miller-Bravais indices are used throughout this study. A brief description of this easily-used system is presented here.

3.2 Miller-Bravais Indices.

Unlike the Miller system of indexing, four axes, a_1 , a_2 , a_3 and c are used as illustrated in fig 3.1. For an ideal h.c.p material formed by close packed spheres, the ratio of the length of the c and a axes is 1.633. In practice for the pure metals this varies between 1.57 and 1.89. The indices used are of the type $[u,v,t,w]$ and (h,k,l,l) for directions and planes respectively, where the first three indices in this Miller-Bravais system of notation are related by:

$$u+v+t+w = 0 \text{ and } h+k+l = 0$$

Here the indices correspond to the four axes shown in fig 3.1. Equivalent directions and planes can be obtained by exchanging the position and sign of these first three indices. Throughout this study reference will be made to the basal plane, (0001) and

the prism planes, $\{10\bar{1}0\}$. The basal plane is close-packed, with the close-packed directions being the $\langle 11\bar{2}0 \rangle$'s. The shortest lattice vector is $1/3\langle 11\bar{2}0 \rangle$. It follows therefore that dislocation glide will generally occur with Burgers vector $\mathbf{b} = 1/3\langle 11\bar{2}0 \rangle$, with slip planes either (0001) or $\{10\bar{1}0\}$.

The important dislocation Burgers vectors for the h.c.p system are as follows:

- 1.) Six perfect dislocations in the basal plane with Burgers vectors along the densely packed directions of the form $\mathbf{b} = 1/3\langle 11\bar{2}0 \rangle$.
- 2.) Two perfect dislocations with Burgers vectors perpendicular to the basal plane of the form $\mathbf{b} = [0001]$.
- 3.) Twelve perfect dislocations resulting from the addition of dislocations of types 1 and 2 above, resulting in dislocations of the form $\mathbf{b} = 1/3\langle 11\bar{2}3 \rangle$.
- 4.) Two imperfect dislocations with Burgers vectors perpendicular to the basal plane of the form $\mathbf{b} = 1/2[0001]$.
- 5.) Six imperfect basal dislocations of the Shockley partial type, of the form $\mathbf{b} = 1/3\langle 1\bar{1}00 \rangle$.
- 6.) Imperfect dislocations resulting as a combination of types 4 and 5 and thus having the form $\mathbf{b} = 1/6\langle 2\bar{2}03 \rangle$.

Three basal plane stacking faults exist which retain close-packing of the close-packed layers. Two intrinsic faults (conventionally I_1 and I_2) together with an extrinsic fault (E).

I_1 : is formed by the removal of one basal layer followed by slip of the form $1/3\langle 10\bar{1}0 \rangle$ to reduce the stacking fault energy, thus:

ABABABABA.....- ABABBABA.....- ABABCBCB

I_2 : is formed by $1/3\langle 10\bar{1}0 \rangle$ slip in a perfect crystal:

ABABABAB - ABABCACA

E: is formed by the addition of an extra plane:

ABABABAB - ABABCABAB

All these faults are shown schematically in fig 3.2. These faults introduce a layer of f.c.c packing (ABC) into the material and thus will have an associated characteristic

stacking fault energy γ . The change in the second neighbour sequence of the planes is the main contributor to the stacking fault and since there is one change for I_1 , two for I_2 , and three for E, to a first approximation we can say $\gamma_E = 3/2\gamma_{I2} = 3\gamma_{I1}$.

Generally experimental estimates for γ are higher than for the f.c.c materials. Stable faults have been observed on prism and pyramidal planes, but much of the evidence for this comes from computer simulation, (see section 3.5), rather than directly from experimental observation.

3.3 Dislocation loops in h.c.p metals.

This study is primarily concerned with identifying the dislocations produced by heavy-ion implantation, and so the Burgers vector of a dislocation is of primary importance, since from this the loop is known to be either faulted or perfect and the habit planes of these dislocations can then also be identified. Two types of loop populations are commonly observed in h.c.p materials, namely those with their habit planes on either the prism or basal planes.

Basal loops are formed by the removal (vacancy) or addition (interstitial) of one basal layer, resulting initially in a loop of Burgers vector $\mathbf{b} = 1/2[0001]$. This is unstable since for a vacancy type dislocation, two similar atomic layers will be in contact whereas for an interstitial platelet there will also by definition be an associated stacking fault, which may or may not be unstable. Two partial unfauling reactions are possible for vacancy loops (see Hull and Bacon, 1984 for a full description). In one the stacking of one layer may change, i.e from B to C due to glide below the layer of a $1/3\langle 1010 \rangle$ Shockley partial accompanied by a second Shockley partial of opposite sign above the layer giving a resultant reaction:

$$1/2[0001] + 1/3[1\bar{1}00] + 1/3[\bar{1}100] = 1/2[000\bar{1}] \quad (3.1)$$

Alternatively, a single $1/3\langle \bar{1}010 \rangle$ Shockley partial may sweep over the platelet displacing the atoms above by $1/3\langle 10\bar{1}0 \rangle$ relative to those below giving:

$$1/2[0001] + 1/3[1\bar{1}00] = 1/6[2\bar{2}03] \quad (3.2)$$

Loops of type (1) are sessile Frank loops with $b^2 = c^2/4 \sim 2a^2/3$ and represent

the extrinsic stacking fault described earlier, while loops of type (2) are sessile Frank partials with $b^2 \sim a^2$ and are thus I_1 type intrinsic faults.

It is important to remember that due to the variations in stacking of the different loop types (section 3.2) γ_E is approximately three times γ_{I1} , and since dislocation energy is proportional to b^2 with the addition of the contribution from the stacking fault energy, a critical loop size will therefore exist for which the partial unfauling reaction (3.2) is energetically favourable, as in the f.c.c case. Both these loop types have been observed experimentally (i.e Phythian 1985). Factors such as stress, temperature and impurity content as well as the stacking fault energy will all have some bearing on which loop type results. Since the basal planes are not the most densely packed planes for $c/a < \text{ideal}$, but are observed experimentally to be the habit planes of loops in some cases, it would seem that basal stacking faults aid the stability of these loops. The stacking fault energy can be determined experimentally as follows. Assuming circular loops and $\gamma_E = 3\gamma_{I1} = 3\gamma$, then from isotropic elastic theory the total energy of the two basal loop types for a loop of radius ρ may be equated for the critical loop size r_c , at which the two energies are equal, an expression for γ can therefore be found (see Phythian *et al* 1987):

$$\gamma 2\pi r_c^2 = r_c G b_s^2 \frac{(1-\nu/2)}{2(1-\nu)} \left[\ln \left(\frac{8r_c}{r_o} \right) - 2 \right] \quad (3.3)$$

where

r_c = the critical radius (determined experimentally)

G = the shear modulus

ν = the Poisson ratio

r_o = the dislocation core radius (one to two atomic spacings).

b_s = the shear component of the Burgers vector, in this case $a/3$

Thus we have a method for calculating the stacking fault energy from experimental data. It is encouraging to note that Phythian *et al* (1987) successfully used this method to obtain an estimate for both the basal and prism stacking fault energies in

ruthenium. These in fact turned out to be very close to the theoretically calculated estimates of Legrand (1984). It is clear that the core radius is a sensitive parameter here for determining the stacking fault energy and thus will limit the accuracy of the final calculation, and this will be taken into account when the equation is utilised in later chapters.

Turning now to the case of prism plane loops, which are the type we would expect to dominate for $c/a < \sqrt{3}$, since the corrugated prism planes are then the closest packed. This range includes most of the h.c.p materials. Transmission electron microscopy studies have revealed vacancy loops of both the faulted $1/2 \langle 10\bar{1}0 \rangle$ type and the perfect $1/3 \langle 11\bar{2}0 \rangle$ type, together with some observations of perfect interstitial loops with Burgers vector of the type $\mathbf{b} = 1/3 \langle 11\bar{2}0 \rangle$. It is interesting to note that the $\{11\bar{2}0\}$ planes are neither close packed nor widely spaced and that $\mathbf{b} = 1/3 \langle 11\bar{2}0 \rangle$ loops are found not only as pure edge loops on the $\{11\bar{2}0\}$ planes but also as non-edge loops at up to 30° from pure edge (i.e on the $\{10\bar{1}0\}$ densely packed planes). It seems likely therefore that point defects initially nucleate as a single layer platelet on the $\{10\bar{1}0\}$ close packed planes with an associated stacking fault. Again, if energetically favourable, this will unfault by a shear with the Burgers vector reaction:

$$1/2 \langle 10\bar{1}0 \rangle + 1/6 \langle \bar{1}2\bar{1}0 \rangle = 1/3 \langle 11\bar{2}0 \rangle \quad (3.4)$$

The resulting loops are perfect glissile loops which are able to adopt the variety of orientations observed in T.E.M. From the size at which the perfect loops are seen to begin to dominate an estimate may also be made for the stacking fault in the prism plane of titanium, from elastic theory we find:

$$\gamma \pi r_c^2 = r_c G b_s^2 \frac{(1-\nu/2)}{2(1-\nu)} \left[\ln \left(\frac{8r_c}{r_o} \right) - 2 \right] \quad (3.5)$$

where here b_s is the shear component of the perfect Burgers vector and thus equates to $a/2$.

3.4. T.E.M observations of dislocation loops in h.c.p materials.

By far the most extensive work so far undertaken in this area is the work of Phythian (1985) and Phythian *et al* (1987, 1990), on ruthenium, a material originally chosen for its similar c/a ratio to the commercially important materials titanium and zirconium, coupled with the fact that T.E.M foils could be easily produced and stored without the rapid deterioration due to oxidation inherent with titanium and zirconium foils. A complete list of the important h.c.p elements together with their melting point, atomic number and c/a ratio is given in table 3.1.

Phythian's detailed study involved room temperature heavy ion irradiations of varying ion energy (10-100 keV) and varying ion mass (84 [Kr] - 184 [W]) into single crystal ruthenium. The important conclusions arising were as follows.

- 1.) All the loops observed were vacancy in nature.
- 2.) As with earlier studies, cascade collapse occurred readily to produce faulted $\mathbf{b} = 1/2\langle 10\bar{1}0 \rangle$ loops on the $\{10\bar{1}0\}$ prism planes.
- 3.) A population of perfect $\mathbf{b} = 1/3\langle 11\bar{2}0 \rangle$ loops was also noted, these were assumed to form as a result of an unfauling reaction as detailed in equation (3.5).
- 4.) An anisotropic effect due to ion beam direction was observed. When the foils were irradiated approximately parallel to the basal planes a small population of basal plane loops was also observed. These basal loops initially formed as $\mathbf{b} = 1/2[0001]$ loops, some of which subsequently unfaulked to $\mathbf{b} = 1/6\langle 20\bar{2}3 \rangle$ loops with lower associated stacking fault energy, as in reaction (3.4) above.
- 5.) Loop depth increased for increasing ion energy and decreasing ion mass.
- 6.) Defect yield increased with ion energy and had a complex dependence on ion mass, increasing with mass at low energies but decreasing with mass at high energies.
- 7.) Cascade efficiency increased with ion mass and decreased with increasing ion energy.
- 8.) Estimates for the basal and prism stacking fault energies were obtained and these were in good agreement with Legrand's (1984) theoretical values for ruthenium.
- 9.) Significant loop loss was observed, most markedly for foil orientations at 45° to

the basal plane where loops were observed to glide to the surface before any analysis was possible, although loop loss was also observed to some extent in all the orientations used.

This work has highlighted the importance of the unique crystal structure of the h.c.p metals to the ensuing damage observed, while the yield and efficiency values obtained have further underlined the role played by vacancy concentration and subcascade formation. This will be considered further in the context of the present work in the discussion chapters.

3.4.1 Quenching studies

Taking an historical perspective to research in the field of h.c.p materials we find that, initially, vacancy loop formation in metals was originally studied by quenching experiments. This process produces a large supersaturation in the vacancy concentration in the metal by first raising it to near its melting point at which vacancies are numerous and mobile, and then rapidly cooling (quenching) back to room temperature, thus effectively freezing the extra vacancy population into the material. Berghezan *et al* (1961) quenched zinc and the subsequent analysis revealed basal loops of Burgers vector $\mathbf{b} = 1/6\langle 20\bar{2}3 \rangle$. Hales *et al* (1968) confirmed this analysis and also observed that the loops grew under the electron beam in the T.E.M. They proposed that the mechanism for this growth could be attributed to vacancy injection from the oxide surface. An interesting study by Hillairet (1970) on quenched magnesium revealed that for pure (<1 ppm impurities) magnesium, prism loops of the $\mathbf{b} = 1/3 \langle 11\bar{2}0 \rangle$ perfect type are seen, whereas for material containing only 30 ppm impurities the prism faulted $\mathbf{b} = 1/6 \langle 20\bar{2}3 \rangle$ loops are observed. This highlights the fact that impurities can play an important role in loop nucleation and growth. In this study, therefore, great care has been taken to determine the exact impurity content of all the materials studied. Both $1/6\langle 20\bar{2}3 \rangle$ and $1/2[0001]$ loop types were observed by Levy *et al* (1975) in work on quenched single crystal cadmium, so by this stage a pattern of faulted vacancy loops forming on the most densely packed planes was beginning to emerge. However quenching only illuminates

our understanding of the vacancy component in some metals. The behaviour of the interstitial component of damage must also be considered, and this can be achieved using electron irradiations.

3.4.ii Electron Irradiations.

For electron irradiations, the electron microscope is not only the analytical tool but also assumes the mantle of projectile implanter. Typically, a High Voltage Electron Microscope (H.V.E.M) is used. This produces high fluxes of high energy electrons, usually around 1 MeV compared with a standard T.E.M which will operate at around 100-200 keV. Electron irradiation differs from neutron (and indeed heavy ion) irradiations in that the maximum energy transferable to the p.k.a is small, (< 100 eV), as can be calculated from equation (2.2), and thus cascade phenomena are not expected to occur. A profusion of isolated point defects (Frenkel pairs) are produced and at high enough doses these may agglomerate by diffusion into dislocation loops. It is usual therefore for only the interstitial component of damage to be seen since the vacancies, although present, will be far less mobile in most metals at room temperature and thus unable to agglomerate into visible dislocation loops. However, at elevated temperatures the vacancy component of damage may manifest itself as voids e.g Carpenter (1973), although this study also noted that helium ion implantation was necessary to stabilise these voids.

Whitehead *et al* (1978) investigated the effect of high energy electrons on zinc and cadmium, finding both $b = 1/2[0001]$ and $b = 1/6\langle 20\bar{2}3 \rangle$ type basal loops. They also noted that on continued irradiation double basal loops began to form, i.e $1/2[0001] + 1/2[0001]$ or $1/6\langle 20\bar{2}3 \rangle + 1/6\langle 20\bar{2}3 \rangle$. Hossain and Brown (1977), working on magnesium found perfect prism $b = 1/3\langle 11\bar{2}0 \rangle$ loops in magnesium, in direct contrast with an earlier study by Kwadjo (1973). Interestingly, in this earlier study, the same single crystal was used but the specimens examined were fatigued and this resulted in the observation of basal $b = 1/6\langle 20\bar{2}3 \rangle$ loops. Salisbury *et al* (1980) also looked at magnesium and again interstitial basal loops of $b = 1/6\langle 20\bar{2}3 \rangle$ were observed. Faulted basal loops with a

central unfaulted area were also observed, the central unfaulted area comprising two $b = 1/6\langle 20\bar{2}3 \rangle$ loops such that the sum of the outer and inner loops combined was $[0001]$.

As mentioned already, however, quenching and electron irradiations do not generate the high energy p.k.a's inherent to neutron damage in a reactor environment, so we now turn to heavy ion experiments.

3.4.iii Heavy-ion Irradiations.

Apart from the study of ruthenium by Phythian (1985) already mentioned, the pioneering work in this area was performed by Föll and Wilkens (1977) on cobalt. They irradiated three distinct orientations (and indeed instigated the S_1 , S_2 and S_3 notation used by Phythian and detailed in the next chapter) of single crystal cobalt with 60 keV gold ions. A vacancy loop population consisting mostly of perfect prism plane loops with $b = 1/3\langle 11\bar{2}0 \rangle$, together with a few faulted vacancy loops with $b = 1/2\langle 10\bar{1}0 \rangle$ were observed and so the now accepted mechanism of unfaulting from $1/2\langle 10\bar{1}0 \rangle$ to $1/3\langle 11\bar{2}0 \rangle$ was first proposed as outlined in reaction (5). Interestingly, although a specific hunt for basal loops was undertaken, none was found. Woo and Carpenter (1983) irradiated titanium with bismuth ions and observed mostly $b = 1/3\langle 11\bar{2}0 \rangle$ loops together with a few $b = 1/2\langle 10\bar{1}0 \rangle$ loops. However this study was far from rigorous, for no basal loops were sought and only basal orientation foils were irradiated, so this work has been repeated as an integral part of the present investigation into cascade collapse in titanium. From these works, it becomes clear that cascade collapse to form dislocation loops can occur readily in the h.c.p system with low dose irradiations producing a reasonably high yield of loops, unlike for instance in the case of b.c.c iron. Thus heavy-ion implantation is a good tool for investigating the expected behaviour of these materials under a neutron flux.

3.4.iv Neutron Irradiations.

Despite the expense and difficulties involved there are also a few cases where

h.c.p materials have been studied following exposure to a neutron flux. Early work on neutron irradiated rhenium by Brimhall and Mastell (1968) utilised the I vector technique developed by Rühle (1965) to analyse the nature of the defects observed. They observed perfect prism plane loops, however, as already mentioned, perfect prism plane loops have now been identified with $\{10\bar{1}0\}$ habit planes and the I vector technique employed could have been mistaken these loops with the faulted $1/2\langle 10\bar{1}0\rangle$ loops. Caution must therefore be used when assessing the earliest work. It is now commonly accepted practice to use the **g.b** analysis technique described in detail in the next chapter and used throughout this study. However it is still worth noting that Brimhall and Mastell identified prism loops with $\mathbf{b} = 1/3\langle 11\bar{2}0\rangle$, since this is the only study to date that has been performed on rhenium. Brimhall (1971) went on to look at neutron irradiated titanium and again observed $\mathbf{b} = 1/3\langle 11\bar{2}0\rangle$ perfect loops. He also noted that these loops were elliptical in nature, having their major axis in the $[0001]$ direction and the minor axis in the basal planes. Later work by Jostsons *et al* (1980) went on to show that the ellipticity of the loops varied with their vacancy/interstitial nature. They found the ratio of the major to minor axes was ~ 0.45 for vacancies and ~ 0.7 for interstitials. Griffiths (1983) looked at both annealed and cold-worked neutron irradiated titanium and reported seeing mainly vacancy type $\mathbf{b} = 1/3\langle 11\bar{2}0\rangle$ loops, but also noted a small population of basal defects present in the cold-worked specimens with $\mathbf{b} = 1/n\langle 20\bar{2}3\rangle$.

Finally, it is interesting to record the work of White *et al* (1983), who irradiated polycrystalline titanium with 3 MeV protons at 710 K to a dose of 0.02 d.p.a. Their analysis of the defects produced was inconclusive but determined that most of the damage was of the type $\mathbf{b} = 1/n\langle 01\bar{1}w\rangle$ where n and w are non-zero integers, and the loops were noted to have $\{10\bar{1}1\}$ habit planes. The defects were also analysed in a S.T.E.M revealing a quantity of iron clustered around the defects consistent with a monolayer over the whole defect and this will be further considered in the results chapter.

3.4.v Zirconium.

No mention has been made as yet of the defect structures observed in irradiated

zirconium. A wealth of papers exist on the reaction of zirconium and its alloys to the full gamut of irradiations, due to its commercial viability as a reactor construction material. This arises from the inherently low neutron absorption cross section and also its compatibility with water for water-cooled reactors. However a review of the literature can be a bewildering task since much controversy exists over the exact nature of the damage observed. Bearing in mind that zircaloy is already widely in use in the nuclear industry there is obviously a great need for a heightened understanding of this material's behaviour.

One important detrimental effect due to exposure to a neutron flux is the phenomenon known as growth, that is a change in the shape of the material with little or no associated change in volume. Since the materials used for reactor construction are polycrystalline and indeed are additionally cold-worked to increase their defect density, growth will tend to be suppressed due to the random orientations of the crystal grains. This, however is not the case in textured materials such as zirconium after annealing, since this material satisfies the two criteria for growth, namely it exhibits an anisotropic response to irradiation (i.e basal and prism loops are crystallographically distinct) and in polycrystalline form the individual grains tend to align unidirectionally (texture). This behaviour, coupled with the fact that several models for growth are reliant on the presence of c-loops in zirconium (e.g Buckley 1962, Dollins 1975, Pedraza 1981) necessitates conclusive evidence to be found for the presence or absence of basal loops in zirconium. In this and subsequent sections basal loops, which have an $[0001]$ component to their Burgers vectors, will be referred to as c-loops.

For many years the debate raged as to the presence of c-loops, with much evidence being compiled on both sides until it was decided to end the controversy once and for all by setting up an international round-robin study in which five leading international laboratories were each given the same starting material (zirconium and zircaloy-2) and then independently neutron irradiated and analysed the material before reporting back for comparison and discussion. The findings of this research are reviewed by the various workers both individually and also jointly in Northwood

et al (1979). The damage structures observed were found to consist entirely of $1/3\langle 11\bar{2}0 \rangle$ loops with no evidence at all for c-loops. Both vacancies and interstitials were noted, the majority being vacancy in nature. As observed earlier in titanium, the loops were elliptical, with the major axis again in the [0001] direction, but here the axial ratio varied from 0.5 to 1.3 with no obvious correlation between ellipticity and vacancy/interstitial nature being observed. The study makes special note of the detrimental effect of surface hydrides to the quality of electron micrographs attainable. Some of the earlier observations of c-loops are therefore possibly attributable to surface hydride contrast effects. Other earlier evidence for c-loop damage had been the effect known as "corduroy" contrast. Bell (1975) originally believed that this effect was associated with c-component damage, despite the fact that no c-loops were visible in the electron microscope in this study and corduroy contrast was found to be present in every sample. Kelly (1976) claims that corduroy contrast in fact arises from foil relaxation due to long range stress fields of $1/3\langle 11\bar{2}0 \rangle$ dislocation loops arranged in bands parallel to the (0001) plane. Interestingly, an earlier study by Blake *et al* (1974) had noted that loops of the same Burgers vector and habit plane tend to align in rows and this "rafting" effect is believed to occur due to glide caused by interactions between the localised stress fields of the loops. However Bell and Adamson (1978) dispute Kelly's interpretation, maintaining that corduroy is not an artefact and this issue remains as yet unresolved. Other trends elucidated by this exhaustive study were that there was a reduction in mean loop size and an increase in loop density for zircaloy-2 in comparison to pure zirconium, highlighting the effect of solute addition. Also, in general, loop size was found to increase and loop density decrease as the irradiation temperature is raised.

The earliest "confirmed sighting" of c-loops now dates back to Jostsons *et al* (1977), who observed that they occurred in only two of the five batches of material they neutron irradiated and only when the irradiation temperature rose above 720 K. Further evidence for c component damage comes from electron irradiation work. Griffiths *et al* (1983) observed $\mathbf{b} = 1/6\langle 20\bar{2}3 \rangle$ and $\mathbf{b} = 1/3\langle 11\bar{2}3 \rangle$ loops between

575 and 775 K. The $1/3\langle 11\bar{2}3 \rangle$ loops were noted to be interstitial and had pyramidal or complex habit planes and were shown to be largely dependent on the foil normal, lying on only two of the six available $\{1\bar{1}01\}$ planes, implying that the surface stresses generated by oxidation are important. Vacancy loops with $\mathbf{b} = 1/2[0001]$ were also observed at 725 K (Griffiths *et al* 1984) and these were again shown to be largely dependent on the foil normal. More recently Zee *et al* (1987) have turned once again to neutron irradiated zirconium due to renewed interest in the role of c component damage in the growth of zirconium and its alloys. They report extremely high growth rates in swaged single crystal zirconium and believe this is correlated to the accompanying moderate density of a and c component dislocations and high density of oriented twins. Annealing the crystals prior to irradiation led to a substantial reduction in the growth rate and although this behaviour was complex, it again reveals a glimpse of the role played by dislocations in this material. An interesting phenomenon observed in zirconium, originally noted by Carpenter *et al* (1981), is the onset of "breakaway growth" at high irradiation temperatures and high neutron fluences; that is the growth rate initially saturates but then at advanced doses the growth rate again increases, not dramatically, but there is a definite increase. Rogerson (1988) reviews much of the current work in this field, noting that break-away growth is observed in both single and poly-crystalline zirconium and also some zirconium alloys. Causey *et al* (1986) note that c component dislocations introduced during irradiation result in increased creep and growth suggesting that these c component dislocations act as preferential sinks thus increasing the vacancy-interstitial separation and hence giving rise to the enhanced "breakaway" growth observed. This growth behaviour is noted only at high fluences and is consistent with the development of a "cold-worked" type microstructure in annealed materials above the breakaway fluences, i.e c component dislocations are present, which is not observed to be the case for low dose irradiations.

Void formation in zirconium is difficult to produce and this property adds to the desirability of the metal as a reactor material. Indeed void formation is generally observed only when solute gases such as neon or helium have been pre-injected to

help stabilise the voids. This is the case for both neutron (e.g Gilbert *et al* 1979) and electron irradiations (Faulkner and Woo 1980).

3.5 Computer Modelling.

Computer modelling of the h.c.p system is still very much in its infancy due to the difficulties inherent in obtaining accurate interatomic potentials. Bacon (1988) recently reviewed the more successful attempts at modelling and emphasised the achievements and limits of the work in this field so far. He notes that when normalized energies are used all the model crystals have similar qualities and none so far have as yet come close to replicating the behaviour of any of the real h.c.p metals. Stable vacancy and interstitial platelets have been successfully modelled. Interestingly Foster *et al* (1987) found vacancy defects analogous to the stacking fault tetrahedra in f.c.c metals, involving faults in the basal, pyramidal and prism planes. Several stable and meta-stable sites have been identified for self-interstitials, lying both in the basal planes and between them.

3.6 Trends.

Reviewing the whole range of h.c.p metals we now see certain trends emerging. For materials with $c/a < \text{ideal}$, loops form preferentially, but not exclusively, on the prism planes with either perfect $\mathbf{b} = 1/3\langle 11\bar{2}0 \rangle$ or faulted $\mathbf{b} = 1/2\langle 10\bar{1}0 \rangle$ Burgers vector, dependent on the loop size and stacking fault energy of the material. Similarly, faulted loops with $\mathbf{b} = 1/6\langle 20\bar{2}3 \rangle$ and $\mathbf{b} = 1/2 [0001]$ are observed to dominate when the c/a ratio rises above $\sqrt{3}$. The observation of both populations of loops in a single material may well be attributable to impurities (c.f magnesium) and crystallographic orientation to the irradiation beam, (ruthenium, c-loops in S_3 but not S_1).

There is therefore a good deal of uncertainty in relation to the properties of point defects and their clusters, both in terms of displacement cascade parameters (e.g the number and concentration of defects, and crystal anisotropy) and material properties (e.g c/a ratio, stacking fault energy and melting point). Thus the rest of

this study deals with the search for evidence to shed light on the theories outlined in the last two chapters over the whole range of h.c.p materials.

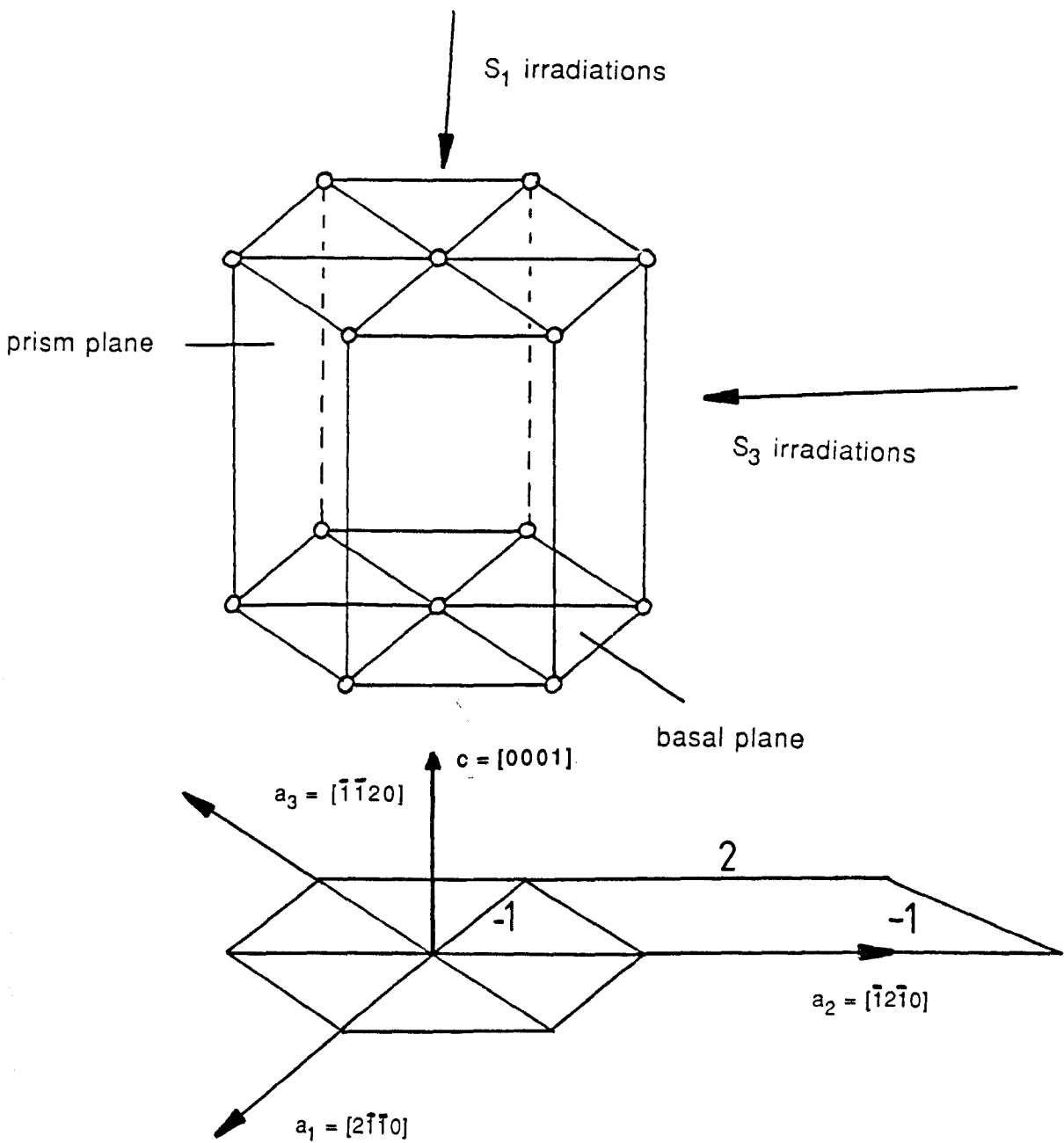
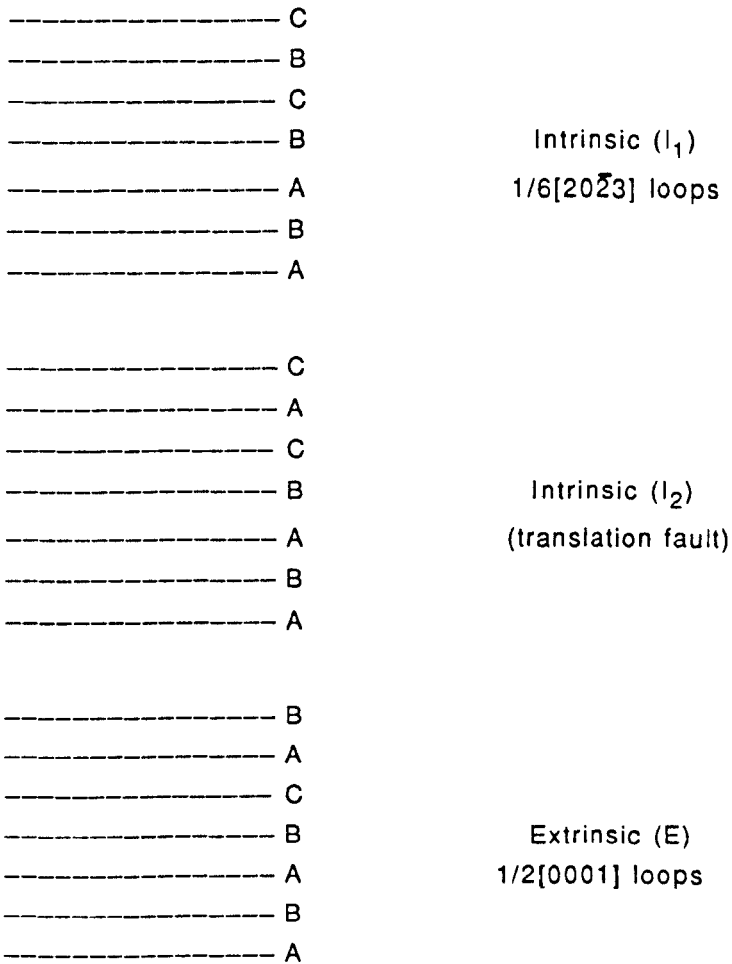


Fig 3.1: A schematic representation of the crystallography of the h.c.p system and an illustration of the irradiation directions S_1 and S_3 .



Energetically: $\gamma_E \sim 3\gamma_1$: $\gamma_2 \sim 2\gamma_1$

Fig 3.2: A schematic of the stacking faults observed on the basal plane in hexagonal-close-packed materials.

Metal (At.No)	Melting (K) Point	S.F.E (mJ/m ³)		Atomic Weight	Lattice Parameters (Å)		
		γ_{basal}	γ_{prism}		a	c	c/a
Beryllium (4)	1550	R = 0.6		9.01	2.286	3.584	1.568
Yttrium (39)	1520	210	60	88.9	3.65	5.73	1.57
Hafnium (72)	2423	390	185	178.49	3.195	5.051	1.581
Ruthenium (44)	2520	875	520	101.07	2.706	4.282	1.582
Titanium (22)	1948	290	110	47.9	2.951	4.684	1.587
Zirconium (40)	2125	340	150	91.22	3.231	5.148	1.593
Rhenium (75)	3450	540	600	186.2	2.76	4.458	1.615
Cobalt (27)	1765	45	230	58.93	2.507	4.070	1.623
Magnesium (12)	924	R = 0.25		24.31	3.209	5.211	1.623
Zinc (30)	693	R = 0.25		65.37	2.665	4.947	1.856
Cadmium (48)	594	R = 0.2		112.4	2.979	5.617	1.886

Table 3.1: Materials parameters for a range of h.c.p.metals. The S.F.E values are those calculated by Legrand (1984). Where γ is not known, R the ratio of the basal to prism stacking fault is shown.

Chapter 4 Experimental methods.

4.1 Background

It has been shown, both experimentally (e.g Eyre 1973) and by theoretical calculation (Winterbon, Sigmund and Sanders 1970) that for the energies used in this study (i.e up to 150 keV), the damage produced by heavy ion irradiation will lie within the first few hundred angstroms of the surface. It is therefore necessary to produce electron transparent foils prior to irradiation, thus ensuring none of the damage is removed during electropolishing. These foils are produced in the form of standard 3 mm transmission electron microscope (T.E.M) discs. Initially the samples were stored and transported in vacuum pots, however problems arose due to the accumulation of rotary pump oil on the specimens which, coupled with vibration induced damage, was found to result in short useful lifetimes of the foils for microscopy, and therefore a more effective storage system was sought. Foils were found to survive much longer when stored in a dry ethanol solution (the water being removed by the addition of anhydrous sodium sulphate). In this way specimen lifetime was found to increase to several weeks before deterioration of foil quality due to oxidation rendered them unusable. Damage in transit was also noted to reduce since the liquid acts as a buffer to any vibrations. Prior to irradiation the foils were carefully marked using a diamond scribe to indicate the irradiated side and after irradiation at Harwell the foils were analysed using either the Phillips EM400T at Harwell or the JEOL JEM 200B at Liverpool.

4.2 Materials

Five metals, titanium, ruthenium, rhenium, magnesium and cobalt have been considered in this study. Since it has been shown that impurity content in single crystal material can have a considerable effect on the resultant observed defect distribution, care has been taken to determine the type and levels of impurity present in the single crystals analysed.

To aid comparison, the ruthenium single crystal foils were machined from the same source as used by Phythian in his earlier study. This crystal was produced by electron-beam zone-refinement of ruthenium powder having the initial impurity content as supplied by the manufacturers Metals Crystals Limited;

Fe	20 p.p.m
Mg, Ni, Si, Ag, Al, Ca, Cr, Cu	< 1 p.p.m each

Both titanium single crystals were very kindly supplied by Dr Yasuhide Minonishi of Tohoku University Japan. The impurity content of the nominally pure crystal was analysed after electron beam zone refining to be;

O 330 p.p.m	C 30 p.p.m
Cl,Fe,H,N <10 p.p.m	Mg,Al,Si,Mn not detected

The commercial purity crystal was supplied as nominally 0.2 wt% oxygen. However a fuller analysis of the impurity content would obviously prove useful, thus after irradiation the discs were sent for analysis by the chemical division at the U.K.A.E.A Harwell. This process has the innate advantage that the impurity content is measured after the electropolish and anneal and is therefore a good guide as to the state of the foil at the time of irradiation. The following analysis was obtained;

Commercial titanium:

Fe, Cr, Mo and Zr: <0.02 wt %, Al: < 0.05 wt %,
O: 0.11 wt % C: 0.060 wt % N: < 0.001 wt %

The cobalt, rhenium and magnesium single crystals were supplied by Metals, Crystals and Oxides. Unfortunately there was not enough material for a full analysis. However the crystals were supplied with claimed purities of:

cobalt	99.995%
rhenium	99.99%
magnesium	99.998%

4.3 Disc preparation.

Samples from the six h.c.p single crystals were prepared using the same basic technique. Firstly the crystals were aligned in the required crystallographic

orientation. This was achieved by the use of back-reflection Laue X-ray diffraction techniques. Having calculated the interplanar spacings and stereographic projections for each material (note that this is necessary due to the variation in c/a ratio) the orientation of each single crystal may thus be obtained from the results of the individual diffraction patterns taken. Thus by careful orientation in the spark eroder the crystals were machined into slices 0.3 mm thick of the required orientations. Following the earlier work by Föll and Wilkens (1977) and Phythian (1985) it is clear that due to the anisotropic nature of the h.c.p system and the possibility of loop loss due to foil orientation, the two orientations of most interest were;

$$S_1 : n_f \sim [0001]$$

$$S_3 : n_f \sim \langle 12\bar{3}0 \rangle$$

as illustrated in fig 3.1, where n_f is the foil normal and thus these are the only orientations irradiated in this study. The reasons these orientations were chosen will be discussed more fully in the results chapter. From these slices, 3 mm discs were trepanned, again by the use of spark erosion. The discs were then polished on 600 grit to remove any residual deposits and surface damage caused by the spark machining process. These were electrolytically cleaned prior to being placed in the ultra-high vacuum (U.H.V) furnace for heat treatment.

With the exception of cobalt (due to its low vapour pressure), all the materials were annealed at approximately 10^{-9} Torr at varying temperatures in a U.H.V furnace specifically designed for 3 mm T.E.M discs (see Table 4.1 for individual materials details). This was necessary since in the as-received condition the crystals have an unacceptably high dislocation density which must be reduced to ensure that observed damage is due solely to the irradiation performed. It should be noted that for titanium care must be taken not to exceed 882 °C as the metal undergoes the α - β phase transformation to b.c.c at this temperature thus destroying the single crystal nature of the foils. In the furnace each T.E.M disc was separated by a molybdenum blank to prevent sintering during the anneal. The temperature during the anneal was monitored by means of both a thermocouple and an infra-red detector.

The pressure was also carefully monitored and by means of a system of titanium sublimation pumps in addition to the usual design of a rotary pump, diffusion pump and cold trap can be kept below 10^{-7} Torr during the anneal. After the anneal the temperature is lowered slowly to ensure that few vacancies are quenched into the samples, and the discs were then ready for electropolishing.

Cobalt is known to sublime in a high vacuum and also has a low transformation temperature (440°C) to the f.c.c structure, and therefore U.H.V heat-treatment is unsuitable. The cobalt discs were sealed in a quartz tube under a vacuum of $\sim 10^{-5}$ Torr and then placed in a standard baffle furnace at 400°C for 24 hours before being slowly cooled back to room temperature.

The discs were all electropolished using a Strueurs twin jet Tenupol. Each material requires different electrolytic solutions and voltage settings and these are detailed in table 4.2. The flow rate was set to the minimum capable of maintaining a constant current so as to reduce buckling of the foils. It should be noted that in all cases except ruthenium, d.c current was used. Juchniewicz (1962) found that when a d.c current was applied to platinum the electrolyte polarised in the vicinity of the disc thus inhibiting polishing, but if an a.c current was applied perforation and good foil quality could be achieved. Phythian (1985) found that this method also resulted in a good final polish for ruthenium. Immediately the foils were indicated to have perforated by the light sensor on the Tenupol they are immersed in a methanol bath maintained at the same temperature as the electrolytic solution being used, thus removing any traces of the polishing solution left on the surface. The foils were then moved to another methanol bath and washed for several minutes as any contamination at this stage will be extremely detrimental to the final image quality obtained. Thus washed, the foils were then stored in dry ethanol to await irradiation. In the case of ruthenium, distilled water rather than methanol was used to wash the discs, as this is found to result in better quality foils.

Thomas and Balluffi (1967) noted that contamination of the foil prior to irradiation due to observation in the microscope can enhance defect cluster

formation, thus affecting the final defect parameters observed, and so foils were not inspected prior to irradiation. However when new materials were worked upon, foils were initially checked to determine whether the anneal had been successful and to fine-tune the electropolishing conditions, but to ensure accuracy of results these foils were not subsequently irradiated.

4.4 Chemical etching.

During the study it became clear that the "commercial " grade titanium was in fact polycrystalline in nature and so it was therefore necessary to find a large grain which could then be oriented in the desired crystallographic direction to produce the requisite number of equally oriented discs. This was achieved by etching the crystal using the following solution:

- 50% distilled water
- 40% conc nitric acid
- 10% hydrofluoric acid (40% assay)

The crystal was immersed in this solution at room temperature for eight minutes, achieving a good edge attack to highlight the grains, and careful spark-machining then enabled single crystal S_1 foils to be produced.

4.5 Foil irradiation.

Once polished, the foils were transported to Harwell for irradiation, and to ensure consistency of results all irradiations have been carried out using the same machine (a schematic of which is shown in fig 4.1), a modified commercial "Lintott" ion implantation system. Where possible, irradiations of different materials with the same ion energy, species and dose were performed at the same time to guarantee consistency of irradiation doses. For a complete list of irradiations performed see table 4.3.

In this study, titanium, bismuth and antimony ions have been used for the implantations. Heavy ions such as these are produced by means of an ionising arc sustained by electrons from a heated tungsten filament parallel to an ion extraction

slit. Gas or vapour is introduced into the graphite walled arc chamber surrounding the filament and a small (100 G) magnetic field is applied to minimise discharge instabilities and increase ionisation. The ion beam is then extracted through a 42 mm x 1.5 mm slit by means of a two electrode system producing a wedge shaped beam. This then passes through a magnetic analyser which is a variable isotope separator, and thus the ion beam can be adjusted for maximum transmission and optimum focusing by tilting the source assembly on a vacuum bellows. The ion beam typically passes through the analyser magnet at a standard 30 keV and post-acceleration of the ions to the required energy can take place across a single gap electrode system.

The specimens are irradiated at normal incidence by the use of specially machined aluminium bars to compensate for the seven degree tilt of the target back-plate with respect to the beam. In this manner up to 50 discs can be irradiated at the same time. These bars are loaded and unloaded via a clean room into the target chamber, which can be vacuum isolated from the rest of the machine. The bars are fastened to a plate which traverses continuously, both horizontally and vertically throughout the period of the irradiation. Typical irradiation times for a low dose experiment are around five minutes. In this time approximately forty complete oscillations of the target can take place. This method has the advantage that non-uniformity of the beam caused by undeflected neutral components is completely eliminated (i.e scanning is mechanical not electrostatic) and ion beam heating effects are reduced. The target chamber is pumped independently of the separator and is fitted with a liquid nitrogen cold trap to reduce hydrocarbon vapour pressure, thus reducing specimen contamination. The principal dosage used in this study was 5×10^{11} ions/cm², and at this dose the mean ion spacing on the target is $1/(5 \times 10^{11})^{1/2} = 1.41 \times 10^{-6}$ cm, that is a spacing of 141 Å. Since the dose takes 295 seconds to implant whereas cascade collapse due to individual ions occurs in roughly 10^{-11} seconds, it can safely be assumed that each ion is effectively implanted individually.

4.5.1 Dosimetry Using Ordered Alloys.

At low doses such as 1×10^{11} ions/cm² and below, accurate dose measurements are not possible. The actual implanted dose can only be guaranteed to within 10% (Chivers 1989). With such a large error source a more accurate method of calibration was sought, and to this end T.E.M discs of an ordered alloy Ni₃Al were irradiated alongside the h.c.p foils being studied. Theory suggested that each incident ion would produce one disordered zone (Jenkins and English 1982) in an ordered alloy, and thus by counting the zones observed in the T.E.M it should be possible to make a far more accurate estimate for the dose implanted.

Seiler *et al* (1974) were the first to show that small disordered zones are produced in the ordered alloy Cu₃Au on irradiation with heavy ions. These disordered zones can be imaged in an electron microscope using a strongly excited superlattice reflection, the difference in structure factor between the matrix and the disordered zone being responsible for the observed contrast. Jenkins *et al* (1976) went on to show in two related papers that, apart from extremely light ions such as nitrogen, every incident ion of energy > 10 keV produces one of these disordered zones. Thus a count of the disordered zones should yield very accurate information on the number of incident ions received during an irradiation. Unfortunately, at incident ion energies > 30 keV the onset of sub-cascade formation was noted, and this would obviously negate the value of these irradiations for dosimetry purposes.

Interestingly, Jenkins and English (1982) considered the effect of molecular ion irradiations of Cu₃Au by examining the variations in disordered zones from 50 keV Sb⁺ through to 150 keV Sb₃⁺. This revealed that disordered zone sizes were dependent on total incident ion energy rather than the energy per atom. Thus for instance, the size of the disordered zones for 150 keV Sb₃⁺ molecular ions was similar to the disordered zones produced by 150 keV Sb⁺ single ions, but with a much higher vacancy concentration. Molecular irradiations were seen to produce much more regularly shaped disordered zones than single ions of a similar energy.

In this study the ordered alloy Ni_3Al was used since the onset of subcascade formation noted in Cu_3Au will be detrimental to the accuracy of the dose estimate and it was felt that this onset is likely to be material dependent. Like Cu_3Au , this alloy has the L1_2 structure and so may be expected to behave in a similar fashion. As the primary objective of the ordered alloy irradiations was to more accurately calibrate the received ion dose, the results reported here are far from exhaustive since it soon became apparent that due to extensive sub-cascade formation and significant amounts of overlap between dispersed zones, a simple count of the number of dispersed zones would not yield a viable comparison to the received ion dose at the high energies employed. This can easily be seen from the variations in defect yield for the varying ion energies and masses observed. From these results we see that for the case of Ni_3Al the yield decreases with incident ion energy and on transition to molecular ion irradiation sub-cascade formation becomes frequent. Thus, as distinct from the Cu_3Au case, the dispersed zones for single and molecular ions of the same energy are not equivalent. As the crystal structures are the same this suggests that the materials type has a role to play here, possibly indicating that channelling distances are large in Ni_3Al , thus increasing the probability of high energy secondaries travelling a significant distance from the initial cascade region. However, to pursue this further is beyond the scope of the present study. At these ion energies we note that ordered alloys are not capable of providing an accurate method of dosimetry.

4.5.ii Foil Orientation.

Two distinct crystallographic orientations of foil normal have been irradiated, and the notations for these foil orientations are those originated by Föll and Wilkens (1977) as illustrated in fig 3.1. It is informative to consider the reasons for using these two orientations. The strongly anisotropic nature of h.c.p materials provides the driving force for studying the effects of crystallographic orientation on defect types observed and a few points are worth noting:

- 1.) For the S_1 orientation perfect prism loop loss is minimised since the Burgers vectors are all approximately parallel to the foil surface.
- 2.) The S_2 orientation used by Phythian (1985) has not been considered in this

study since the superficial advantage of the large number of diffraction vectors obtainable is negated by the extremely rapid loop loss observed due to all Burgers vectors being inclined at 45° to the foil surface.

3.) In the S_3 orientation approximately two thirds of the perfect prism loop population could be lost to the foil surface due to image forces, but identification of c-loops is facilitated.

4.) The use of both S_1 and S_3 orientations is necessitated by the shortfall of available diffraction conditions.

4.5.iii Channelling Effects.

From equation 2.9 for the channelling angle equation for low energies, we find that for titanium irradiated with 100 keV Sb^+ ions the channelling angle is approximately six degrees, and thus to reduce channelling effects the titanium single crystals were oriented seven degrees off-axis during spark-machining to prepare the foils. Note that this is the maximum channelling angle for titanium since the angle is inversely proportional to energy and also decreases for molecular ions (Gemmell 1974). For consistency of results each crystal was oriented at seven degrees off-axis but the channelling angles for the other materials irradiated in this study (for the case of 100 keV Sb^+ ions), again calculated from equation 2.9, are listed below and these differences will be taken into account in chapter 7.

Material	Channelling angle (degrees)
magnesium	4.5
titanium	6
cobalt	7.5
ruthenium	8.5
rhenium	10

4.6 Transmission Electron Microscopy.

Electron microscopy has been performed on the JEOL JEM 200B at Liverpool and occasionally on a Phillips EM 400T at Harwell. Specimens were mounted in a double

tilt holder to facilitate foil tilting in all directions. The cobalt specimens, being magnetic, required a special specimen holder to be machined. This employed a threaded gimbal which could prevent the cobalt foil being pulled out of the holder due to the magnetic field of the electron microscope. Specimens were loaded into the electron microscope with the electron exit surface corresponding to the irradiated side of the specimen as indicated by the diamond scribe mark. Thus any gun damage will occur on the electron entry surface on the opposite side of the foil to the implanted damage and can therefore be distinguished and discounted by stereo microscopy depth measurements. Also, superior defect image quality is obtained when the defect lies closest to the electron exit surface.

A full T.E.M geometry analysis for the S_1 orientation entails the imaging of nine different diffraction vectors, namely the three types of each of $g = 02\bar{2}0$, $11\bar{2}0$, $11\bar{2}2$. At the end of the analysis the initial diffraction condition was repeated in case any of the observed loops unfaulted or were lost from the foil during the time scale of the analysis. It should be noted that the $g = 0002$ diffraction condition is unobtainable in this orientation, rendering the unequivocal identification of c component loops much more difficult. Each diffraction condition was imaged under both bright and dark fields with $s_g \sim 0$, and an accompanying diffraction pattern was also taken to ensure the validity of the diffraction vector and also to identify its direction on the diffraction contrast images recorded. For the S_3 case diffraction conditions with $g = 0002$ and also three of the six $11\bar{2}0$ and $20\bar{2}0$ g's were used. Since tilting of the foil in this orientation limits the number of these diffraction vectors which are accessible, this in turn means that a unique determination of the precise Burgers vector of all the prism loops is not possible. This orientation remains interesting however since the 0002 g provides conclusive proof of the existence of basal loops. Information is also to be gained from the effects of changed crystallographic orientation on resultant ion beam damage.

Standardisation of microscopy was ensured by the following procedure. All geometry analyses were performed at 200 keV using an electron-microscope magnification of 95,000 x. Photographic enlargements were produced to a final

print magnification of 530,000 x. For each diffraction condition of interest both a bright field (b.f) and a dark field (d.f) image was taken. Wherever possible all micrographs were taken using an exposure time of five seconds. All microscopy was performed at a foil thickness of approximately 750-1000 Å, this thickness being roughly determined by counting the relevant number of extinction distances in from the edge of the wedge shaped foil (i.e 3-4 extinction distances for $g = 11\bar{2}0$ in titanium). Using thinner areas creates problems of loop loss to both surfaces, depth image ambiguities (i.e is the defect closest to the top or bottom of the foil ?) and foil bending in the electron beam.

The loops produced in this study were all noted to be less than 125 Å in diameter and thus are seen as small black-white images in the T.E.M. Image analysis involves determining the following: loop size, loop type, number of loops, loop depth, and loop habit plane. Each of these is now considered in turn.

a.) Loop size.

This is determined by measuring the length of the black-white interface imaged under two-beam dynamical diffraction contrast for any $g \cdot b \neq 0$. Stathopoulos (1977) showed that the black-white image width corresponds very accurately with loop size for dynamical contrast. All size measurements were taken from dark field $g = 11\bar{2}0$ micrographs at the standard magnification of 530,000 x. These measurements were performed on a Kontron "videoplan", a commercial system consisting of a 300 mm x 300 mm magnetic digitising tablet linked to a personal computer capable of producing two and three axis plots from the statistical input. The point to point resolution from prints at a magnification of 530,000 x corresponds to an accuracy of roughly 2 Å. However, operator error was shown to be a larger influence on the results obtained. By repeatedly measuring a standard 50 Å loop at this magnification, the operator accuracy was found to be only ± 3.5 Å, and thus a true error of ~ 3.5 Å can be expected under these conditions for the range of loop sizes observed. Size measurements were always taken using at least two different $g = 11\bar{2}0$ micrographs of the same area since it is not possible to determine defect size from a $g \cdot b = 0$ "butterfly" image. Care must also be taken not to

measure just the large loops at the expense of the smaller loops and thus influencing the size distribution obtained.

b.) Loop crystallography.

Concurrently with loop size, loop geometry was also investigated. This involved comparing the images obtained from up to nine different dark-field diffraction conditions, with those predicted for each particular diffraction condition by computer simulation. The $\mathbf{g}\cdot\mathbf{b}$ products for any given loop type and for all diffraction conditions used in this study are shown in table 4.4. The groundwork for computer simulated images of dislocation loops was laid by Eyre and co-workers in a series of four important papers {Eyre et al (1977 a & b), Holmes et al (1979) and English et al (1980)}. These papers revealed that earlier work involving the \mathbf{l} vector technique breaks down when the angle between \mathbf{g} and \mathbf{b} is large, and demonstrated the need for a superior method of image simulation. This they set about devising, their studies revealed a link between image symmetry and the following:

- 1.) \mathbf{g} and loop plane normal \mathbf{n} for a particular Burgers vector \mathbf{b} and foil normal \mathbf{z} .
- 2.) \mathbf{z} for a particular combination of \mathbf{g} and \mathbf{n} .
- 3.) the value of $\mathbf{g}\cdot\mathbf{b}$, dependent on crystal thickness, loop depth and loop radius.

The study went on to define the now familiar four types of image contrast to be expected from dislocation loops, i.e no contrast ($\mathbf{g}\cdot\mathbf{b} = 0$), "butterfly" contrast (if the angle between the electron beam and the loop normal is 90° and $\mathbf{g}\cdot\mathbf{b} = 0$), black-white contrast ($\mathbf{g}\cdot\mathbf{b} = 1$) and black-white contrast with structure at the interface ($\mathbf{g}\cdot\mathbf{b} > 1$).

A good match between these predicted images and actual loops has now been observed in a whole host of materials. Further work by Perrin (1981) showed that no significant changes occurred when anisotropy effects were considered, and due to the excellent agreement with experiment this technique has become universally accepted. In this study a slight adaptation of the simulated images for the h.c.p case has been used, details of which can be found in Phythian (1985). The adaption

centres around the non-cubic nature of the lattice, and thus the Miller indices must be changed to the Miller-Bravais notation commonly used for the hexagonal structure as described in section 3.1. Again excellent agreement with experimentally observed loops is achieved.

c.) Loop number.

To determine the defect yield (discussed in detail later), the number of loops present in a micrograph must be accurately determined. To gain a quantitative analysis of both the mean density of loops present and their statistical spread throughout the micrograph, each micrograph was separated into eight equal squares of sides 5.3 cm, and thus corresponding to an area of 10^6 \AA^2 . The loop count from each of these areas can then be summed to provide both a total loop count and the standard deviation of the distribution of the loop numbers over the entire micrograph. The errors quoted in this study for defect yields are therefore the standard deviations (σ_{n-1}) of the counts found from the distinct areas of the micrographs.

d.) Loop depth.

An \mathbf{l} vector can be assigned to a black- white dislocation loop image, defined as the direction joining the centre of the the black lobe to the centre of the white lobe (\mathbf{l} positive). Theory predicts that the sense of \mathbf{l} reverses periodically throughout the foil, at approximately 0.25, 0.75 and 1.25 ξ_g , where ξ_g is the extinction distance. The extinction distances for each of the metals studied have been calculated for all of the diffraction conditions used and these are presented in table 4.5. Thus by accurate determination of the depth of the loop from the surface by stereo microscopy, the layer in which a loop resides can be ascertained, and thus the vacancy/interstitial nature of the loop can be found since in each layer $g \cdot \mathbf{l}$ is complementary for vacancies and interstitials. This is illustrated in fig 4.2. It should be noted that at the top of the foil $g \cdot \mathbf{l}$ will be identical in bright- field and dark field whereas at the

bottom surface it will be opposite. Also in dark- field the sign of $g \cdot l$ is identical at the top and bottom of the foil whereas in bright-field it will be opposite.

To facilitate accurate stereo microscopy, small gold islands were firstly evaporated onto the irradiated surface of the T.E.M disc to be examined. This is achieved by melting a small length (~1 mm) of high purity gold wire in a good vacuum approximately 15 cms from the T.E.M disc, and small islands of gold (about 10 Å across) then coalesce onto the cool surface of the disc. These islands act as a reference plane lying on the irradiated surface of the disc during subsequent stereo analysis. The actual microscopy involves taking two similar dark-field diffraction images lying on the same Kikuchi line. In this case the $11\bar{2}0$ Kikuchi tram line has been used and images were taken at a tilt of 10 degrees either side of the 0001 pole. The T.E.M magnification used was 60,000 x and the final print magnification used was 170,000 x. The micrographs were analyzed on a stereo viewer, a device which accurately measures the parallax between two stereo images. The depth of the defects below the surface is given by the formula:

$$\text{depth}(\text{Å}) = \text{parallax (mm)} \times 10^7 / [2 \times \text{print mag} \times \sin(\theta/2)]$$

where θ = total tilt angle (20°)

Thus a parallax of 1 mm corresponds to a depth of 160 Å, and with care it is possible to achieve an accuracy of .05 mm i.e ~8 Å.

e.) Loop habit plane.

The habit plane of the loops observed, i.e their normal n , has been investigated using the m vector analysis technique. The m vector of a loop is defined as the direction normal to its black-white interface (for a $g \cdot b = 1$ or 2 image), and from the simulations of Eyre *et al* detailed above it is known that for these loops, where b and n lie normal to z , the m vector gives a precise determination of n . Even when b or n is inclined to z by $< 45^\circ$, m still gives a reasonably close approximation to n . When n lies parallel or close to z , m is not related to n , but in this case the rotation of m with g illustrates that n is close to z .

4.7 Interpretation of Data.

Three important parameters to be calculated from the raw data obtained from the micrographs are defect yield (d.y), cascade collapse efficiency (ϵ) and defect retention efficiency (D.R.E). The first two of these parameters were originally defined by Merkle (1966). The defect yield gives a measure of the proportion of incident ions producing cascades which subsequently undergo collapse to form a visible vacancy loop. The cascade collapse efficiency measures the proportion of vacancies which survive recombination and are subsequently present in the observed vacancy loops. The defect retention efficiency is found from the product of the d.y and ϵ and is thus a measure of the proportion of point defects surviving in the foil.

The defect yield is calculated from the equation:

$$d.y = N_L / N_I \quad (4.1)$$

where N_L = the number of vacancy loops observed per unit area.

N_I = the number of incident ions per unit area.

This calculation takes no account of subcascade formation where one incident ion may produce two or more vacancy loops. Jäger and Merkle (1988), introduced the concept of an adjusted defect yield, where loops formed very close together are assumed to be the product of the same incident ion and are thus grouped together and counted as one cascade. Where obvious subcascade formation is occurring therefore an adjusted defect yield $d.y^*$ can also be given. Loops lying in the transition layer may be out of contrast giving a reduction in the observed defect yield, but this difficulty can be overcome by tilting the foil while maintaining the same diffraction contrast so that the "missing" loops will move back into contrast due to their change in apparent loop depth. This was not a problem for titanium since all the defects were observed to lie in layer one.

The cascade collapse efficiency is calculated from the equation:

$$\epsilon = N_{obs}^V / N_{calc}^V \quad (4.2)$$

where N^V_{calc} is the number of vacancies initially generated in the cascade, which is calculated using the N.R.T model outlined in chapter two. The number of vacancies present in a loop (N^V_{obs}) is determined by:

$$N^V_{\text{obs}} = \pi d^2 b / 4 \Omega \quad (4.3)$$

where d = the loop diameter

b = the magnitude of the Burgers vector

Ω = the vacancy volume (taken as the volume per atom = $3 a^2 c / 4$)

Operator error was minimised by conducting all the loop size measurements recorded in this study during a single session on the "video-plan".

4.8 Scanning Transmission Electron Microscopy (S.T.E.M).

Finally, evidence of any segregation of material around the dislocation loops has been sought using the V.G 501 S.T.E.M facility at Liverpool. This scanning T.E.M is capable of imaging defects to a very high resolution (several million times magnification). Single defects were imaged under two-beam bright-field conditions. The electron dispersive x-ray results obtained were then compared with a standard taken from the same material but in an unirradiated condition. To improve accuracy defects very close to the foil edge were imaged so that the column of material analyzed was only about a hundred atoms deep, thus any impurity effect around the loop has a greater chance of showing up against the background.

Material	Furnace type	Heat treatment
Titanium	Ultra High Vacuum.	800°C for one hour
Ruthenium	Ultra High Vacuum	1450°C for one hour
Rhenium	Ultra High Vacuum	1450°C for one hour
Magnesium	Ultra High Vacuum	400°C for one hour
Cobalt	Muffle furnace	Quartz tube at 10^{-5} Torr 400°C for 24 hours
Ni ₃ Al	Muffle furnace	5 hours at 1200°C 15 hours at 1100°C 5 hours at 1000°C 5 hours at 800°C 24 hours at 700°C 24 hours at 600°C 48 hours at 500°C Then leave to furnace cool.

Table 4.1: Table showing the heat treatment received by each material studied.

Material	Solution	Voltage	Current	Temp
(1)	6% perchloric acid (70%)	30 V d.c	60-80 mA	≤-20 C
	59% methanol			
	35% 2-butoxyethanol			
(2)	57% aqueous CaCl ₂ (s _g =1.43)	7 V a.c	230 mA	0 C
	39.5% H ₂ O (deionised)			
	3.5% HCl (conc)			
(3)	70% ethanol	30 V d.c	250 mA	5 C
	20% perchloric acid (70%)			
	10% 2-butoxyethanol			
(4)	23% perchloric acid (70%)	18 V d.c	150 mA	10 C
	77% acetic acid			
(5)	25% nitric acid	9 V d.c	100 mA	-40 C
	75% methanol			
(6)	66% ethanol	23 V d.c	200 mA	10 C
	13% H ₂ O (deionised)			
	10.5% perchloric acid (70%)			
	10.5% 2-butoxyethanol			

(1) Gardner and Partridge (1967)

(2) Snow and Breedis (1974)

(3) Thieringer and Strunk (1969)

(4) Brimhall and Mastell (1965)

(5) Hillairet *et al* (1970)

(6) Mallett (1989)

Table 4.2: Table showing the precise electropolishing solutions for each material studied, together with the source of each condition.

Irradiations

Ion Energy	Ion Species	Materials Irradiated
50 keV	Sb ⁺	Ti (S ₁ and S ₃) and "comm" Ti (S ₁)
	Sb ₂ ⁺	Ti (S ₁ [*]), Ni ₃ Al
	Sb ₃ ⁺	Ti (S ₁ [*] and S ₃)
80 keV	W ⁺	S ₁ Ti (and to 10 ¹² ions/cm ²)
	Ti	Mo & S ₁ Ti (also 10 ¹² & 2x10 ¹² ions/cm ²)
100 keV	Sb ⁺	Ti, Co, Mg, Re, Ru (S ₁ and S ₃), and "comm" S ₁ Ti
	Sb ₂ ⁺	Ti (S ₁ [*] and S ₃)
	Sb ₃ ⁺	Ti (S ₁ [*] and S ₃), and "comm" S ₁ Ti
	Bi ⁺	Ti (S ₁)
150 keV	Sb ⁺	Ti, Co, Mg, Re, Ru (S ₁ and S ₃), and "comm" S ₁ Ti
	Sb ₂ ⁺	Ti (S ₁ [*] and S ₃), and "comm" S ₁ Ti
	Sb ₃ ⁺	Ti (S ₁ [*] and S ₃), and "comm" S ₁ Ti
	Sb ₃ ⁺	S ₁ Ti (to 10 ¹² ions/cm ²)

Table 4.3 The irradiations performed in this study. All irradiations were performed at room temperature and to a dose of 5x10¹¹ ions/cm² except where indicated.

* denotes low dose (nominally 5 x 10¹⁰ ions/cm²) irradiations also performed.

Burgers vector (b)	Diffraction condition (g)									
	$11\bar{2}0$	$1\bar{2}10$	$\bar{2}110$	$11\bar{2}2$	$1\bar{2}12$	$\bar{2}112$	$2\bar{2}00$	$20\bar{2}0$	$02\bar{2}0$	0002
$1/3[11\bar{2}0]$	2	-1	-1	2	-1	-1	0	2	2	0
$1/3[1\bar{2}10]$	-1	2	-1	-1	2	-1	2	0	2	0
$1/3[\bar{2}110]$	-1	-1	2	-1	-1	2	2	2	0	0
$1/2[1\bar{1}00]$	0	$3/2$	$-3/2$	0	$3/2$	$-3/2$	2	1	-1	0
$1/2[10\bar{1}0]$	$3/2$	0	$-3/2$	$3/2$	0	$-3/2$	1	2	1	0
$1/2[01\bar{1}0]$	$3/2$	$-3/2$	0	$3/2$	$-3/2$	0	-1	1	2	0
$1/2[0001]$	0	0	0	1	1	1	0	0	0	1
$1/6[2\bar{2}03]$	0	1	-1	1	2	0	$4/3$	$2/3$	$-2/3$	1
$1/6[20\bar{2}3]$	1	0	-1	2	1	0	$2/3$	$4/3$	$2/3$	1
$1/6[02\bar{2}3]$	1	-1	0	2	0	1	$-2/3$	$2/3$	$4/3$	1

Table 4.4: The possible g.b products encountered in this study.

Diffraction Condition	Extinction Distance (Å)			
	Titanium	Rhenium	Cobalt	Ruthenium
20 $\bar{2}$ 0	1950	692	1288	977
11 $\bar{2}$ 0	822	297	539	415
11 $\bar{2}$ 2	1005	353	659	503
0002	504	189	312	259

Table 4.5: The extinction distances in angstroms at 200 keV for all the metals considered in this study.

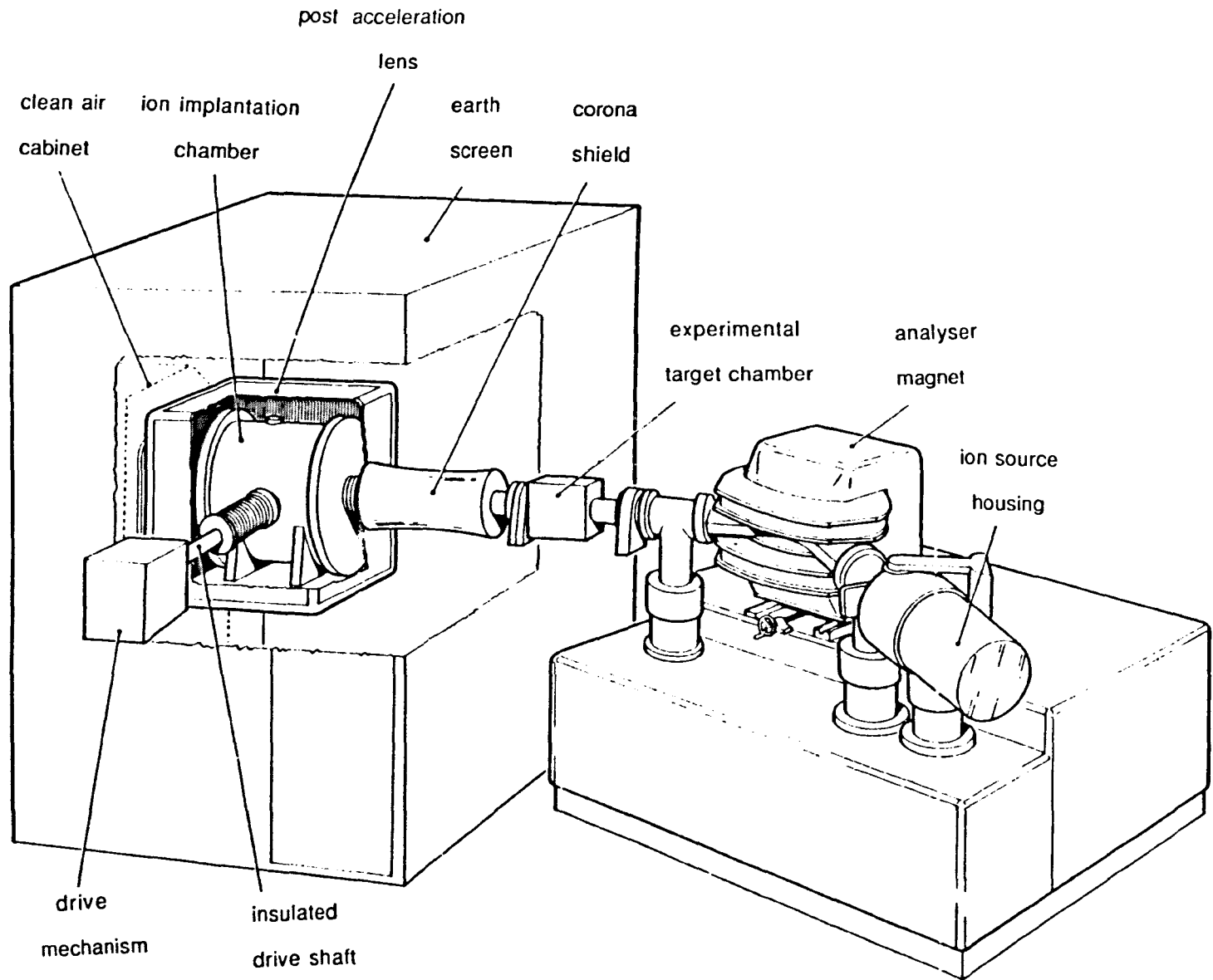


Fig 4.1 : A schematic of an ion implanter.

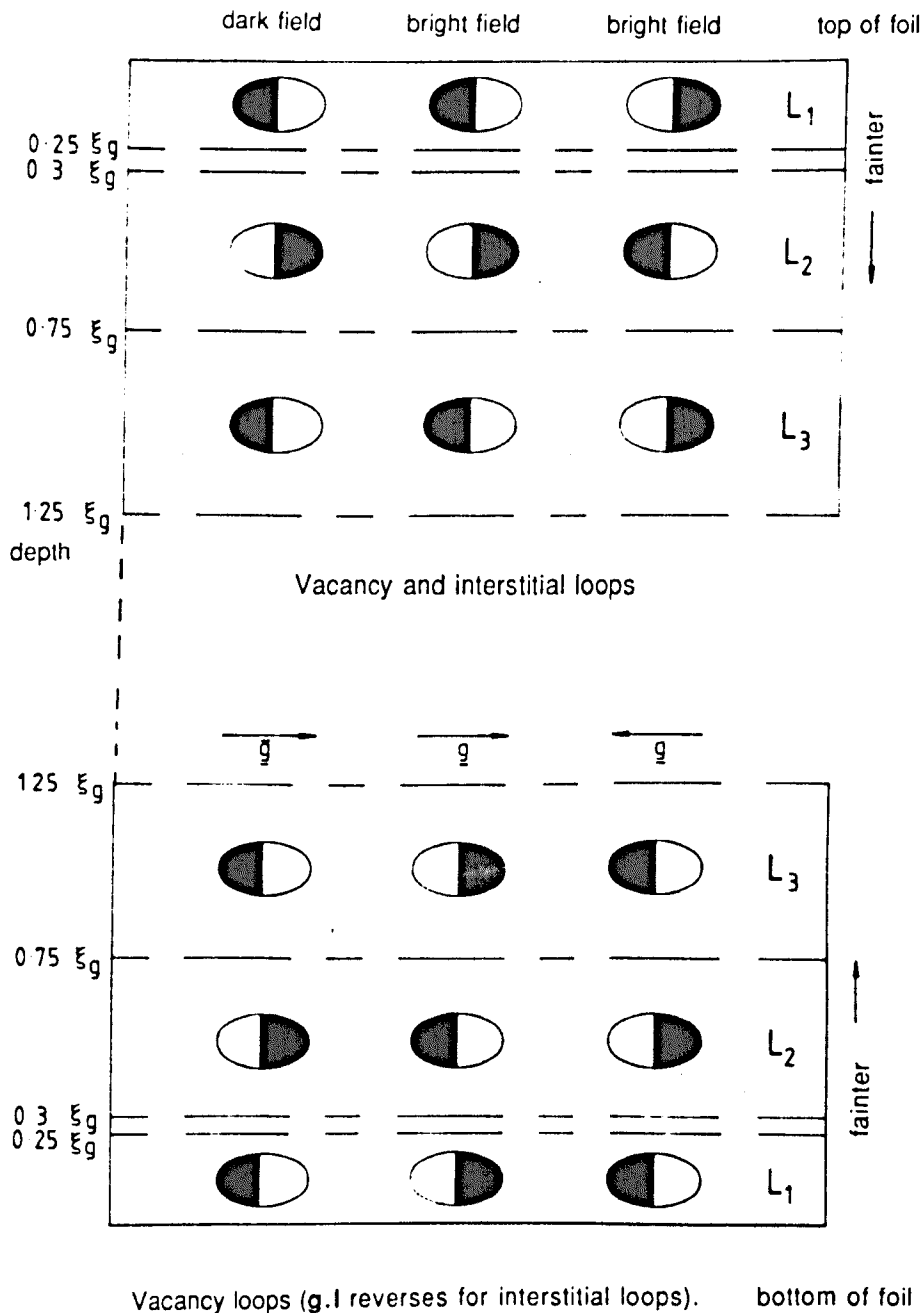


fig 4.2: Reversals due to loop depth as observed in the T.E.M.

Chapter 5

Results.

5.1 Introduction.

The results of the T.E.M investigations performed in this study are presented here. (A full list of all the irradiation conditions used has been detailed in table 4.5). Experimental loop depth measurements, theoretical loop depth calculations, geometry analyses, loop counts and sizing results will be detailed for all the conditions performed in this study. An extremely detailed study of heavy-ion damage in a single h.c.p metal, namely titanium, has been made, and to reflect this the first five sections of this chapter will focus entirely on the results obtained from the iodide titanium samples. The next section details the results obtained from irradiations of commercial titanium, this is important since the influence of interstitial solute atoms can be observed without changing any other material parameter, (except for a slight rise in c/a ratio). Following this a range of h.c.p metals has been irradiated to provide information on the effects due to changes in a number of materials parameters. Again this study is unique in that so many varying metals have been irradiated with the same ion beam and thus direct comparison is possible. Finally the results observed throughout the course of this rigorous study are briefly summarised.

5.2 Atomic Ion Implants.

The obvious starting point for the simulation of neutron damage using heavy ion implantation in any material is a series of self-ion irradiations, since these are the most representative of the cascades produced by energetic neutrons. However preliminary work on titanium revealed no visible defect structures even for fluences as high as 2×10^{12} ions/cm² implanted at 100 keV. To check the validity of this result the highest dose irradiation was repeated for titanium together with some molybdenum foils which are known to yield visible vacancy loops at such a high dose, and indeed loops were observed in the molybdenum foils, confirming that the

probability of cascade collapse in titanium is very low. This is an important result, as will be discussed in the next chapter, but since the purpose of this study is to examine vacancy loop formation it was decided to repeat the work of Woo and Carpenter (1983) who irradiated titanium with bismuth ions, thus producing cascades of higher energy density and defect concentration, which is known to increase the probability of collapse to form vacancy loops. In these irradiations loops were indeed observed, but still not in large numbers even at high doses. For instance irradiation of titanium with 80 keV bismuth ions to a dose of 10^{12} ions/cm² produced a defect yield (the fraction of loops created per incident ion) of only 0.06 ± 0.01 .

5.3 The Antimony Ion Matrix.

The course of irradiations used throughout the rest of the study was thus decided on, namely a series of single and molecular ion antimony irradiations were used to produce very high energy-density cascades and also to facilitate comparison with earlier studies of molybdenum (to illustrate the behaviour of differing crystal systems) using similar incident ions. Throughout the rest of this study the same matrix of single and molecular antimony ion irradiations has been employed and the influence of the increasing mass and energy irradiations are detailed in table 5.1. From this table the advantages of this matrix are obvious since it is possible to vary each irradiation parameter individually while holding the other constant, e.g the energy of the incident ion can be held constant while the density of defects produced is increased (the diagonal shown on the matrix). It is hoped that this will be useful to the reader in understanding the results of the irradiations in titanium.

Originally irradiations were carried out to a dose of 10^{12} ions/cm². However, it soon became apparent that this dose resulted in far too dense a loop concentration, especially for the higher energy-density molecular ion irradiations, thus rendering analysis difficult if not impossible. A lower dose of 5×10^{11} ions/cm² was therefore chosen as the basis for the rest of the study. Low doses are useful since the

probability of overlap is then also small.

5.4 Loop Nature and Depth.

As discussed in chapter four, depth measurements are made to determine the vacancy/interstitial nature of the loops observed. The S_1 titanium depth measurements are shown in table 5.2. A typical defect profile obtained is shown in Fig 5.1, here for the case of 150 keV Sb_3^+ ions implanted into S_1 oriented titanium. This ion species (see table 5.3 and fig 5.2) was found to have the deepest ion range of all those used in this study and since all the defects in this extreme case are seen in layer one with $g \cdot l$ positive we may therefore conclude that all the defects observed are vacancy in nature. All the profiles obtained were roughly Gaussian in nature, as can be seen from the profiles obtained for the other irradiations considered (See Fig 5.2), and no evidence for any deep loops due to channelling effects was found. Further information gleaned from the depth profiles can be found in fig 5.4 in which the theoretical depth calculations (from W.S.S 1970, see chapter two) are compared to the observed depth profiles for the range of irradiations into titanium performed. It can be seen from these results that there is reasonable correlation with predicted depth, however the mean depth increases with both increasing ion energy and with transition from Sb_2^+ to Sb_3^+ . The latter is surprising and will be discussed in the following chapter. An example of the microscopy involved for this analysis is shown in fig 5.2, the diffraction condition used in all cases was the $g = 11\bar{2}0$ Kikuchi line with $s_g \sim 0$.

5.5 Loop Analysis.

As discussed in chapter four, two distinct foil orientations have been irradiated, these will now be discussed in turn for the case of iodide titanium. These results are presented first since this material has been the subject of an extensive study into the effects of variation of irradiation parameters on observed defect structures.

5.5.1 The S_1 Orientation.

An example of a typical series of micrographs from an S_1 analysis of iodide titanium is shown in the series of micrographs comprising fig 5.5.

No loops were observed when S_1 titanium foils were irradiated with 50 keV Sb^+ ions, this result was checked several times for validity. Vacancy dislocation loops were observed for all the other antimony irradiations performed on S_1 iodide titanium foils.

An important result noted is that only prism plane loops have been identified for the S_1 orientation, and these were found to be of both the faulted $b = 1/2\langle 10\bar{1}0 \rangle$ type and the perfect $b = 1/3\langle 11\bar{2}0 \rangle$ type. The distribution of these two loop types observed in titanium along with information on loop sizes, and the associated factors defect yield, cascade efficiency and defect retention efficiency is recorded in table 5.3.

From the analysis of the faulted and perfect loops we find that the faulted loops are present in approximately equal numbers for each of the three possibilities $b = 1/2[10\bar{1}0]$, $1/2[1\bar{1}00]$ and $1/2[01\bar{1}0]$. The habit planes of these were invariably perpendicular to their Burgers vector on the corrugated prism planes. For the perfect loops however, the situation becomes more complicated. Detailed analysis reveals that due to the slightly "off axis" crystallographic direction used and the ensuing loop loss variations the three types of perfect prism loops are not observed in equal numbers. This will be considered further in the discussion chapter. Analysis of loop habit plane using the m vector technique detailed in chapter four shows that these loops deviate by varying amounts from $0-30^\circ$ from the pure edge configuration, i.e $b = 1/3[\bar{2}110]$ and n lying between $[\bar{1}010]$ and $[\bar{1}100]$, thus skewing the images around in the direction of the loop normal. The variations in loop normal for perfect loops for the case of S_1 titanium irradiated with 150 keV Sb_3^+ ions is shown in fig 5.6, and details of the loop normals identified for the other irradiation conditions investigated are given in table 5.4, which shows the variation with irradiation parameter for the three extreme conditions studied for S_1 titanium.

From this the pure edge population is seen to be significantly larger for molecular ions than for single ions.

5.5.II. The S_3 orientation.

Analysis of foils having the S_3 orientation is informative since a full analysis of c component loops is possible. An example of a typical analysis of a foil having this orientation is illustrated in the series of micrographs which comprise fig 5.7. Here, unlike in the S_1 orientation, both basal and prism loops are observed. This is an important result since the basal plane has a higher stacking fault energy and thus loops would be less likely to form on these planes. Interestingly no $b = 1/2[0001]$ loops have been found in this study, for the few c component loops which have been observed are all of the reduced stacking fault energy type $b = 1/6 \langle 20\bar{2}3 \rangle$. It should be noted that in this orientation considerable loop loss may occur due to the attitude of the glissile perfect prism loops to the foil surface facilitating loop glide out of the foil under the influence of image forces. This effective reduction in the observed loop population must be considered and compensated for, and this will be considered in detail in chapter six. The results of the S_3 irradiations are presented for the case of iodide titanium in table 5.5. Comparison of these results with table 5.3 showing the S_1 irradiations reveals that the trends are similar in that perfect and faulted prism loops are observed, but also a small population of basal loops is observed. This population is noted to increase slightly for increasing ion energy and mass.

5.6. Loop Size and Density.

5.6.I. S_1 Foils.

The loop size measurements for the S_1 orientation are shown in table 5.6. One particularly surprising result to arise from this study is that the loop size is almost completely invariant throughout the antimony matrix for the S_1 iodide titanium irradiations. The fact that the measured loop size increases slightly with increasing energy, (possibly due to an increase in mean loop depth) and irradiated metal type as seen in the later studies on a range of h.c.p metals, points to this being a real

effect and not operator error. Further information to be gained from the loop sizing is possible evidence for subcascade formation. If some subcascade formation is occurring then a twin peak should be seen in the loop size distributions, since two loops produced by a single ion are likely to be smaller than a single loop assuming that the efficiency does not vary wildly. This effect has not been noted, as can be seen from fig 5.8 where the loop size distribution is shown for S_1 titanium irradiated with 150 keV Sb_3^+ ions. This distribution is shown since it is the one most energetically likely to exhibit subcascade formation. All the loop size distributions obtained for S_1 iodide titanium are shown in Fig 5.9. These size distributions are seen to be approximately Gaussian in nature, and remarkable in their similarity.

5.6.II. Low Dose Irradiations.

It is important to establish that individual cascades are being created as distinct from possible subcascade formation. At a dose of 5×10^{11} ions/cm² in titanium, the vacancy loops are closely spaced and it is consequently difficult to distinguish whether two loops have formed independently, but at close proximity, from different incident ions or as result of a subcascade occurring. To overcome this difficulty a series of low dose irradiations of S_1 iodide titanium were performed at doses less than 10^{11} ions/cm² (table 5.7). It was experimentally impossible to make an accurate estimate for the received ion dose in this range, but these experiments are of value since the dose is substantially lowered and it is therefore easier to identify subcascade events. The criterion used for identifying subcascade formation was chosen to be two loops occurring within $\sim 200 \text{ \AA}$.

A full geometry analysis of these low dose irradiations was deemed unnecessary, since it would reveal no new information. The central result arising from this analysis was that no evidence for subcascade formation could be found. From the additional evidence of the size distributions it is therefore reasonable to assume that ions are producing individual cascade regions. Additional information on the defect yields, loop sizes and cascade efficiencies measured are shown in table 5.7. The nominal dose used in these irradiations was 5×10^{10} ions/cm², but it seems possible

from the results that the actual received dose was substantially higher, this will be considered in chapter six.

5.6.III. S₃ Foils.

The loop size distributions obtained for S₃ iodide titanium are shown in Fig 5.10 the data can be found in table 5.8. It is interesting to note that a definite increase in loop size with increasing ion energy and mass is noted in this orientation. This effect is possibly due to the increased probability of prism loop loss to the foil surface, resulting in preferential loss of large loops. This perfect prism loop loss can be estimated and in the discussion chapter it will be shown that allowing for increased loop loss in this orientation the S₁ and S₃ iodide titanium results are consistent.

5.7 Quantitative Results.

A graphical representation of the defect yield and cascade collapse efficiency data calculated for S₁ titanium is given in fig 5.11. From this the trends to emerge are that the d.y increases moderately with increasing ion energy and dramatically on transition from single to molecular ion irradiations. The efficiency is seen to decrease with increasing ion energy and remains virtually constant for single and molecular ions. For the S₃ titanium irradiations these trends are broadly repeated, (see fig 5.12), although the matrix is not as complete here. The most notable difference is a decrease in yield and efficiency for low ion energy irradiations possibly due to the proximity of the surface, thus leading to reduced mean loop sizes for the lower energy irradiations. To aid the reader a series of figures (Fig 5.13 and 5.14) show the effects on yield and efficiency of an increase along any of the directions shown in the antimony matrix. These are shown for both the S₁ and S₃ orientation.

5.8 Vacancy Concentration and Energy Density.

The vacancy concentration and energy density of a cascade are very important parameters in considering collapse to form a visible loop. A theoretical estimate for

the energy density for each irradiation condition has been determined from W.S.S calculations (see section 2.6), these also provide spatial information on the size and shape of the cascade and hence the total volume of the cascade can be calculated from the formula:

$$V = 4/3 \pi \langle Y^2 \rangle \sqrt{\langle X^2 \rangle}$$

where $\sqrt{\langle X^2 \rangle}$ and $\langle Y^2 \rangle$ are the mean radii of the cascades parallel and normal to the ion beam direction respectively, determined from W.S.S theory. The energy density (Θ_D) in the cascade can then be found from the formula:

$$\Theta_D = \text{F.D.E} / \text{cascade volume.}$$

where F.D.E = fractional deposited energy (from W.S.S data)

The vacancy concentration (C_v) may also be obtained by combining this information with the N.R.T data giving:

$$C_v = N_d / \text{cascade volume.}$$

The results of the N.R.T point defect production calculations together with the data for cascade volume, vacancy concentration and energy density per atom in the cascade are shown in figs 5.15, 5.16, 5.17 and 5.18 respectively. From these graphs the energy density and vacancy concentrations are seen to be very low for single ion antimony irradiations (and these values are even lower for self-ion irradiations), hence it is not unreasonable that cascade collapse in titanium under these conditions is not noted to readily occur. The energy density and vacancy concentration increase for decreasing ion energy, but this increase is accompanied by a near linear reduction in the quantity of point defects produced. These calculations will be used in more detail in the discussion chapters to help to elucidate the mechanisms behind cascade collapse in h.c.p metals.

5.9 Commercial Titanium Irradiations.

As previously mentioned the advantage of studying the commercial grade titanium single crystal lies in the opportunity it allows to study the effects of interstitial solute content without varying any other parameter. Only S_1 foils of this material

were irradiated and the results of these irradiations are presented in table 5.9. The points of interest to emerge here are :

- 1.) Loop depth is found to be similar to iodide irradiations of equivalent ion species (see Fig 5.2)
- 2.) Only vacancy prism loops have been observed.
- 3.) Both faulted and perfect loops were noted, but the perfect loop population was significantly lower than for S_1 iodide titanium foils.
- 4.) Loop sizes are again invariant over the range of irradiations, but the mean loop size is larger than that observed for the S_1 iodide titanium foils.
- 5.) Defect yield and efficiency values follow the same trends observed in the S_1 iodide titanium foils. Graphs showing these trends for the antimony ion matrix are shown in Fig 5.19.
- 6.) Defect yield and efficiency values are in all cases higher than in the S_1 iodide titanium foils.

5.10. Other Metals.

In addition to titanium, four further h.c.p metals (Re, Ru, Mg and Co) have been irradiated using the same ion species and energies, namely 100 and 150 keV Sb^+ ions.

5.10.1. S_1 Foils.

An example of a typical micrograph obtained from each material studied, irradiated to 150 keV is shown in fig 5.20. It should be noted that cascade collapse to form visible vacancy loops was observed to a greater or lesser extent in all the irradiated materials with the exception of magnesium, in which no loops were observed for either of the irradiation conditions used. A central result to emerge from the loop geometries is that in all cases where vacancy loop formation is occurring in this orientation a twin population of faulted and perfect loops has been noted and even when the basal stacking fault is considerably lower than the prism stacking fault, (cobalt) only prism loops were observed.

The size distributions obtained are shown in Fig 5.21. Here the largest loops are

noted for cobalt. Details of the sizes and number of loops measured can be found in table 5.10. The mean loop size in all cases increases for an increase in ion energy. The yield and efficiency results obtained from irradiating these materials in the S_1 orientation are presented in table 5.11. From these results the materials can be arranged in terms of increasing defect yield as follows:

Magnesium, Iodide and Commercial Titanium, Cobalt, Rhenium, Ruthenium

From the efficiency values an interesting result to emerge is that this value is approximately equal for all the metals with the exception of cobalt where the efficiency is noted to be much higher. The efficiency in all cases decreases with increasing ion energy. The mean loop size varies with irradiated material in the range 25 - 50 Å which implies a large variation in the number of defects present per loop, and a hence the variation in efficiency.

5.10.11 S_3 Foils.

Cobalt, rhenium and magnesium foils were irradiated in the S_3 orientation, and for this orientation one particularly surprising result emerged, no loops at all of any geometry could be found in cobalt foils of this orientation. A high density of c-component dislocation lines were however present due to the problems of obtaining well annealed single crystal foils of this material (see chapter three). This result is surprising since the stacking fault energy for cobalt is much lower in the basal plane than in the prism plane.

Unsurprisingly, as with the S_1 case no loops were observed for S_3 magnesium, adding to the evidence that loops will not be seen in this material at room temperature due to the mobility of the vacancies. Unfortunately it was not possible to analyse rhenium samples of this orientation, so the main corroboration for observation of basal loops in $c/a < \text{ideal h.c.p}$ materials comes from earlier work on ruthenium, (Phythian 1985) to which reference should be made.

5.11 Trends.

From the data presented in this chapter some interesting trends have emerged:

- 1.) Vacancy loop formation is strongly material dependent.
- 2.) Defect yield almost invariably rises for an increase in incident ion energy.
- 3.) For molecular ion irradiations a large increase in defect yield and a moderate increase in damage depth is observed in comparison to monatomic irradiations.
- 4.) Efficiencies are observed to decrease in all cases for increasing incident ion energy.

A detailed discussion of these results will be presented in the following chapter. The preliminary results for titanium, together with a discussion of the observed behaviour of this material under heavy ion irradiation can be found in Yellen *et al* (1989)

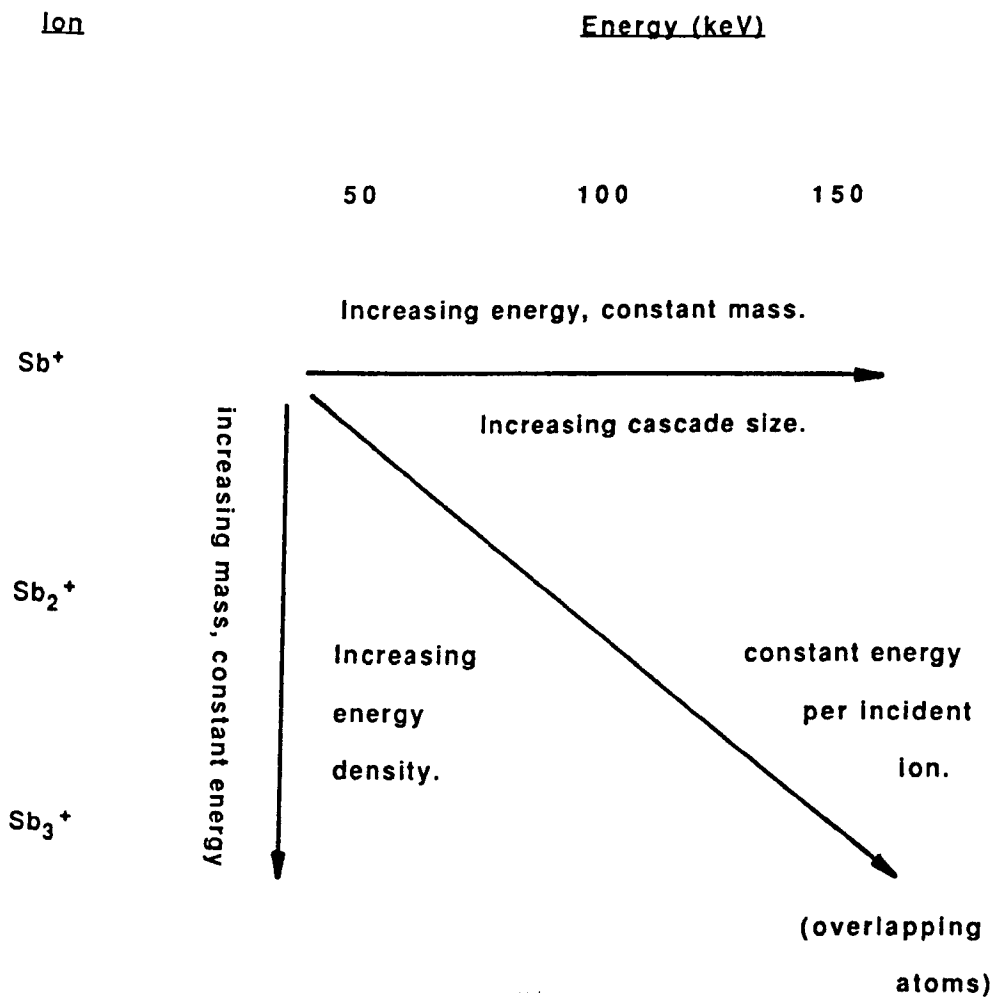


Table 5.1: The influence of increasing mass and energy in the antimony ion irradiation matrix.

Irradiation condition	material irradiated	mean depth(Å)	minimum depth(Å)	maximum depth(Å)	W.S.S (Å)
150 keV Sb ₃ ⁺ ions	iodide titanium	149 ± 18	29	231	125
100 keV Sb ₃ ⁺ ions	iodide titanium	129 ± 14	36	244	94
100 keV Sb ₃ ⁺ ions	commercial titanium	102 ± 10	31	168	94
50 keV Sb ₃ ⁺ ions	iodide titanium	95 ± 8	18	202	57
150 keV Sb ₂ ⁺ ions	iodide titanium	139 ± 15	24	227	170

Table 5.2: Loop depth measurements for S₁ titanium.

Ion	Energy	50 keV	100 keV	150 keV
Sb ₁ ⁺	D.Y	0	0.05 ± .02	.03 ± 02
	ε	0	0.25	0.09
	D.R.E	0	0.013	0.03
	size (Å)	0	33 ± 4	26 ± 4
	faulted	0	74 %, (32)	80 %, (23)
	perfect	0	26 %, (38)	20 %, (44)
Sb ₂ ⁺	D.Y	0.39 ± .04	0.41 ± .04	0.48 ± .05
	ε	0.38	0.27	0.12
	D.R.E	0.15	0.11	0.06
	size (Å)	33 ± 2	34 ± 2	32 ± 3
	faulted	80%, (32)	75%, (33)	75%, (28)
	perfect	20%, (41)	25%, (42)	25%, (42)
Sb ₃ ⁺	D.Y	0.62 ± .05	0.66 ± .05	0.82 ± .06
	ε	0.38	0.29	0.13
	D.R.E	0.24	0.19	0.11
	size (Å)	33 ± 2	35 ± 2	33 ± 2
	faulted	76%, (27)	73%, (26)	71%, (27)
	perfect	24%, (43)	27%, (41)	29%, (42)

Table 5.3 : Data for iodide TI irradiated in the S₁ orientation to a dose of 5x10¹¹ ions/cm², mean sizes are given in brackets.

Pure and non-edge loop
populations.

Irradiation
condition.

150 keV Sb⁺

	loop count	Normalised (%)
Pure edge (0-10°)	20	22
(10-20°)	45	50
Non-edge (20-30°)	25	28

50 keV Sb₃⁺

	loop count	Normalised (%)
Pure edge (0-10°)	84	47
(10-20°)	50	28
Non-edge (20-30°)	46	25

150 keV Sb₃⁺

	loop count	Normalised (%)
Pure edge (0-10°)	84	48
(10-20°)	52	31
Non-edge (20-30°)	38	21

Table 5.4 : The observed and normalised pure and non-edge prism plane loop populations in iodide S₁ titanium. The angular variations between n and b are indicated.

Ion Energy		50 keV	100 keV	150 keV
Sb ⁺	D.Y	0		0.04 ± .02
	ε	0	irradiation	0.08
	D.R.E	0	not	0.003
	size (Å)	0	performed	24 ± .3
	% prism			100
	% basal			
Sb ₂ ⁺	D.Y		.38 ± .04	0.41 + .05
	ε	irradiation	0.15	0.12
	D.R.E	not	0.06	0.05
	size (Å)	performed	29 ± 3	32 ± 3
	% prism		99.75	not
	% basal		0.25	analysed
Sb ₃ ⁺	D.Y	0.44 ± .06	0.45 ± .06	0.50 ± .07
	ε	0.23	0.17	0.14
	D.R.E	0.1	0.077	0.07
	size (Å)	26 ± 2	30 ± 2	34 ± 3
	% prism	not	99.54	99.48
	% basal	analysed	0.46	0.52

Table 5.5 : Data for iodide Ti irradiated in the S₃ orientation.

Ion Energy		50 keV	100 keV	150 keV
Sb ⁺	maximum	0	64.1	56.2
	minimum	0	8.7	7.9
	mean	0	32.7 ± 3.9	26.4 ± 3.6
	loops counted	0	68	55
Sb ₂ ⁺	maximum	61.7	68.3	63.3
	minimum	8.4	8.6	11.7
	mean	33.1 ± 2.0	33.7 ± 1.9	32.2 ± 2.6
	loops counted	272	305	184
Sb ₃ ⁺	maximum	60.4	68.6	85.1
	minimum	8.6	7.4	10.5
	mean	32.6 ± 1.8	35.1 ± 2.4	33.5 ± 2.1
	loops counted	296	221	321

Table 5.6: Loop size distributions in Å for S₁ iodide titanium.

Ion	Energy	50 keV	100 keV	150 keV
Sb ⁺	D.Y	0	Irradiation	Irradiation
	ε	0	Not	Not
	size (Å)	0	Performed	Performed
Sb ₂ ⁺	D.Y	0.9 ± 0.2	0.8 ± 0.2	1.2 ± 0.2
	ε	0.39	0.23	0.14
	size (Å)	34	35	33
Sb ₃ ⁺	D.Y	1.1 ± 0.2	1.0 ± 0.2	1.6 ± 0.2
	ε	0.39	0.18	0.14
	size (Å)	34	34	35

Table 5.7 : Data for iodide Ti irradiated in the S₁ orientation at room temperature to a nominal low dose of 5 x 10¹⁰ ions/cm².

Ion	Energy	50 keV	100 keV	150 keV
Sb ⁺	maximum	0	irradiation	46.8
	minimum	0	not	7.8
	mean	0	performed	24.1 ± 3.3
	loops counted	0		54
Sb ₂ ⁺	maximum	irradiation	52.9	45.9
	minimum	not	9.0	9.8
	mean	performed	28.8 ± 2.7	30.4 ± 2.9
	loops counted		112	108
Sb ₃ ⁺	maximum	42.0	58.1	71.3
	minimum	8.6	10.4	9.9
	mean	25.9 ± 2.4	29.8 ± 2.0	33.6 ± 2.5
	loops counted	120	210	179

Table 5.8: Loop size distributions in Å for S₃ iodide titanium.

Ion	Energy	50 keV	100 keV	150 keV
Sb ⁺	D.Y	0	0.06 ± .02	0.05 ± .02
	ε	0	0.27	0.13
	D.R.E	0	0.016	0.007
	size (Å)	0	34 ± 3	29 ± 3
	% faulted		not	not
	% perfect		analysed	analysed
Sb ₂ ⁺	D.Y			0.64 ± .06
	ε	irradiation	irradiation	0.14
	D.R.E	not	not	0.09
	size (Å)	performed	performed	34 ± 2
	% faulted			79%, (32)
	% perfect			21%, (50)
Sb ₃ ⁺	D.Y		0.75 ± .06	0.98 ± .08
	ε	irradiation	0.20	0.17
	D.R.E	not	0.15	0.17
	size (Å)	performed	36 ± 2	37 ± 2
	% faulted		89%, (38)	88%, (36)
	% perfect		11%, (39)	12%, (41)

Table 5.9 : Data for commercial Ti irradiated in the S₁ orientation at room temperature to a dose of 5 x 10¹¹ ions/cm², mean sizes are given in brackets.

metal	Antimony Ion Energy	100 keV	150 keV
Irradiated			
Co	maximum	104.6	122.7
	minimum	8.4	13.5
	mean	47 ± 3	50 ± 3
	loops counted	210	226
Ru	maximum	72.7	81.4
	minimum	13.0	12.1
	mean	35 ± 2	41 ± 4
	loops counted	210	122
Re	maximum	65.0	65.8
	minimum	6.4	10.6
	mean	31 ± 2	37 ± 3
	loops counted	173	143

Table 5.10: Loop size distributions in Å for ruthenium, rhenium and cobalt.

S_1 c/a	TITANIUM (48) 1.587		COBALT (59) 1.623		RUTHENIUM (101) 1.582		RHENIUM (186) 1.615	
ENERGY (keV) (Sb ⁺ ions)	100	150	100	150	100	150	100	150
D.Y	0.05	0.03	0.13	0.22	0.32	0.4	0.21	0.31
EFFICIENCY	0.25	0.09	0.58	0.45	0.28	0.26	0.28	0.27
D.R.E	0.012	0.003	0.075	0.1	0.09	0.10	0.06	0.08
LOOP SIZE	33 ± 4	26 ± 4	47 ± 3	50 ± 3	35 ± 2	41 ± 4	31 ± 2	37 ± 3
LOOP TYPE F (SIZE) P	68% (32)	80% (23)		87% 47		34% (38)		60% (35)
	24% (38)	20% (44)		4% 112		32% (45)		21% (48)
NUMBER	68	55	210	226	210	122	173	143
S.F.E THEORY P		110		230		520		600
	B	290		45		875		540
S.F.E EXPT P		129-184		281-377				795 - 1120
	B	>272						

Table 5.11: Results of the 100 & 150 keV Sb⁺ ion irradiations into a range of h.c.p metals to a dose of 5×10^{11} ions / cm². Magnesium irradiations omitted since the defect yield in all cases was found to be zero.

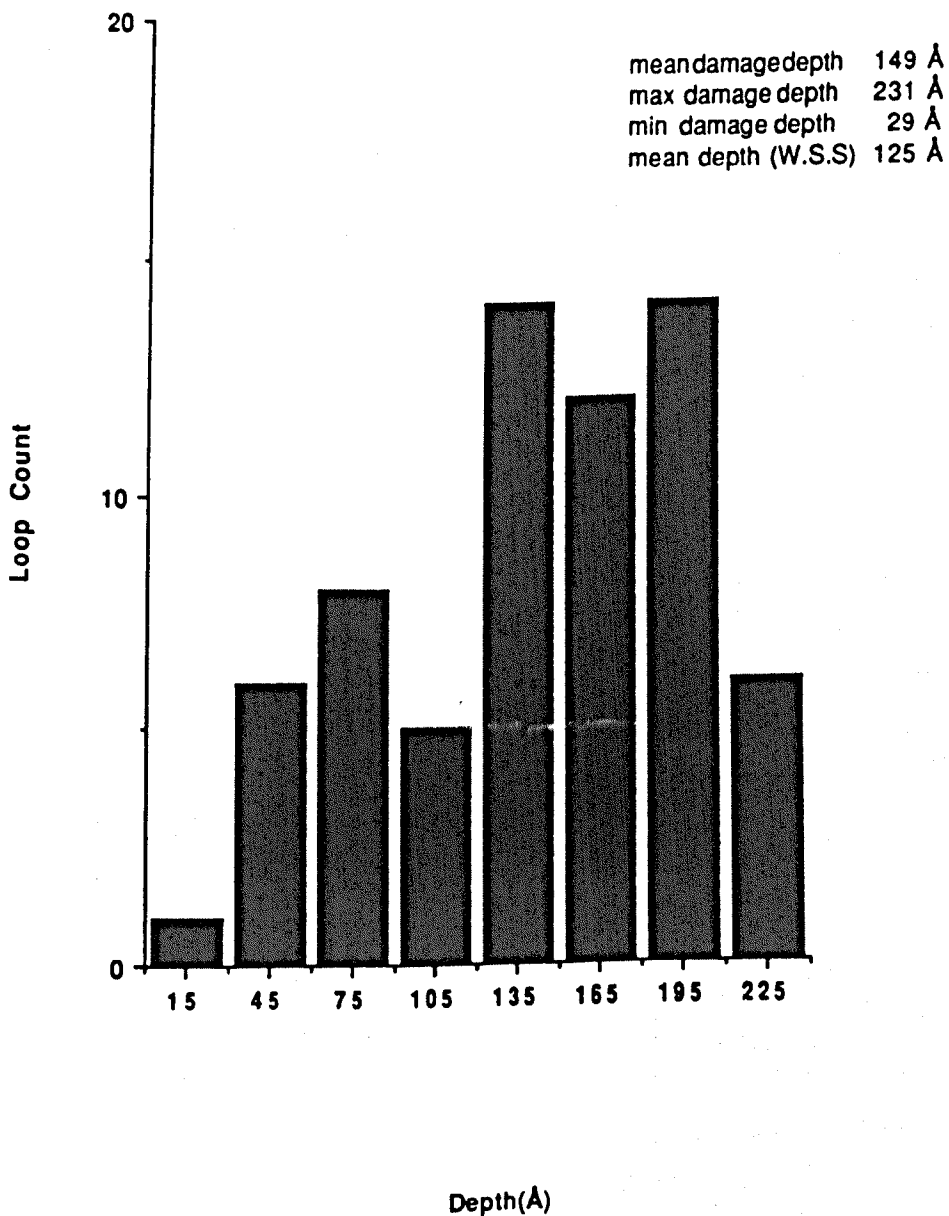
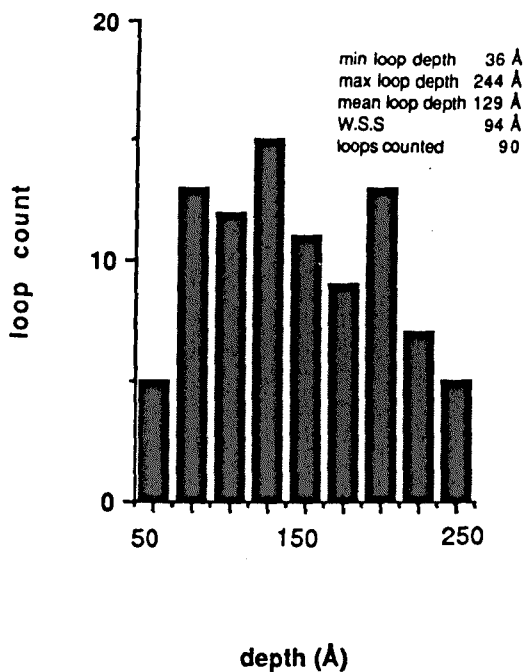
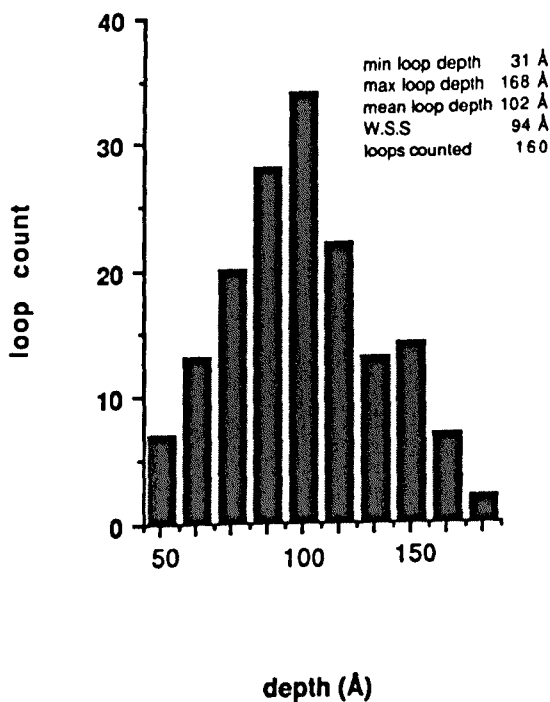


Fig 5.1: Depth distribution for 150 keV Sb_3^+ ions in S_1 iodide Ti.

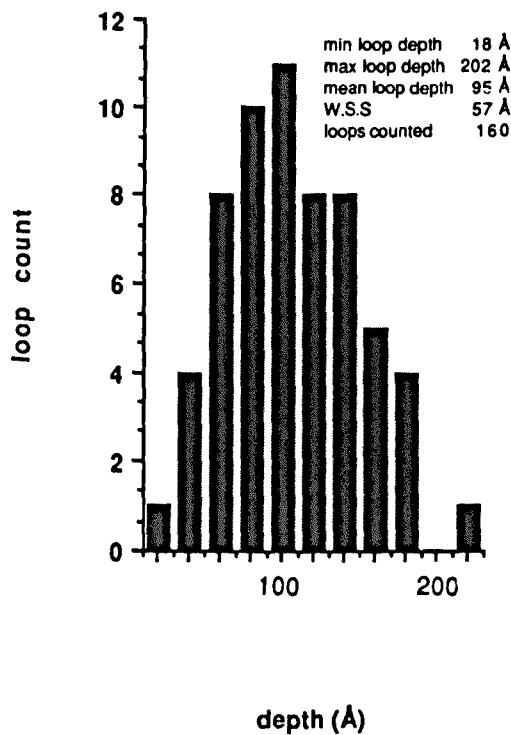
100 Sb3+ into S1 Ti



100 Sb3+ Into S1 commercial Ti



50 Sb3+ into S1 Ti



150 Sb2+ Into S1 Ti

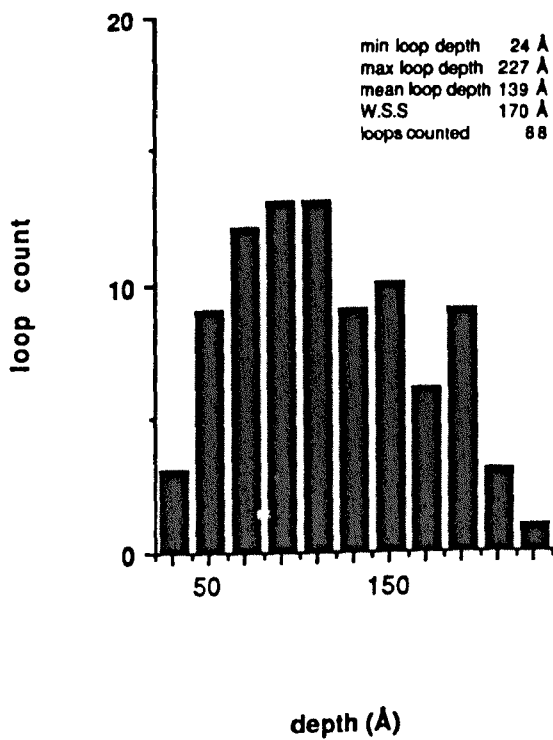


Fig 5.2: Depth distributions for S₁ Ti.

Mean Damage Depth (W.S.S) vs Ion Energy

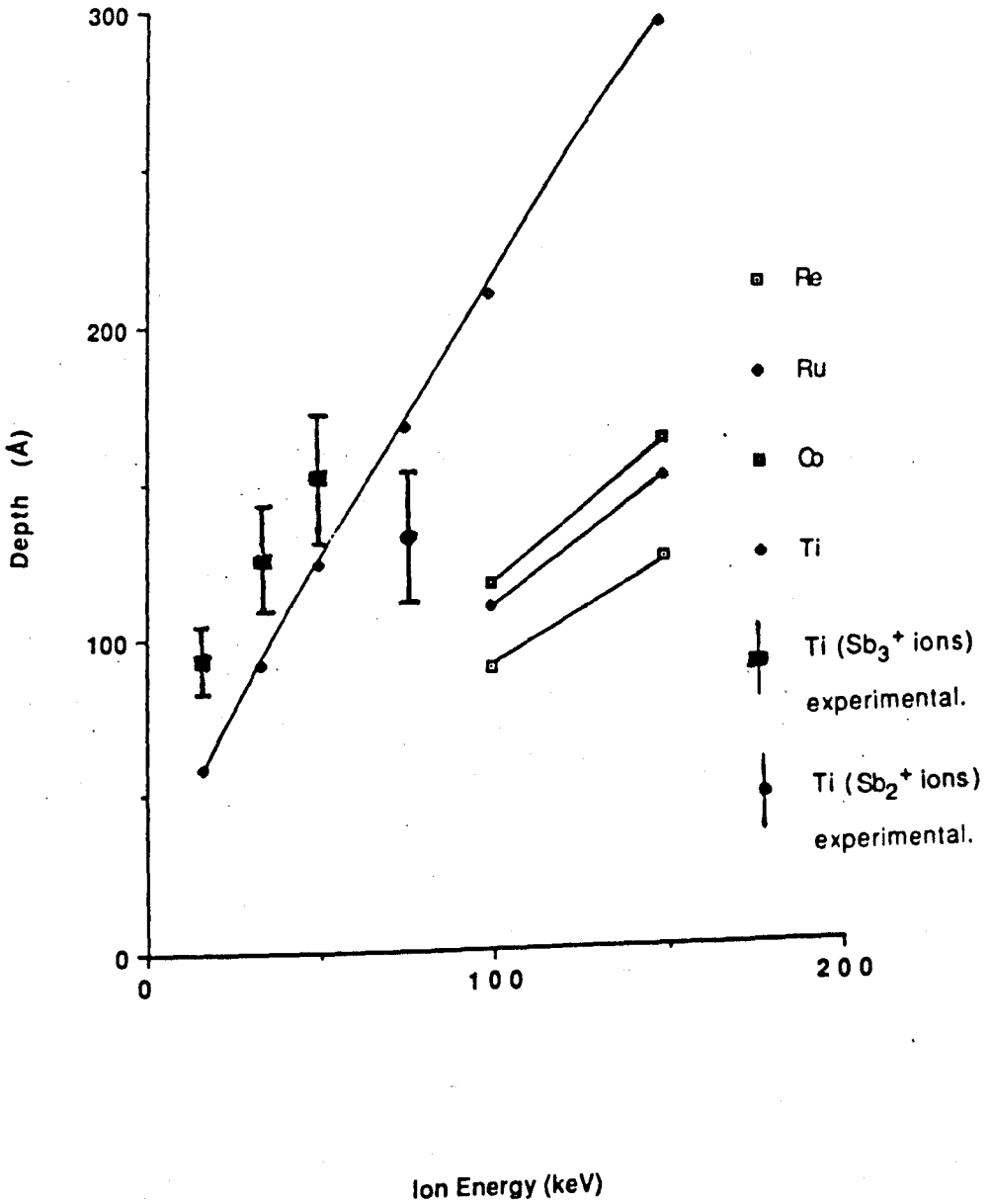
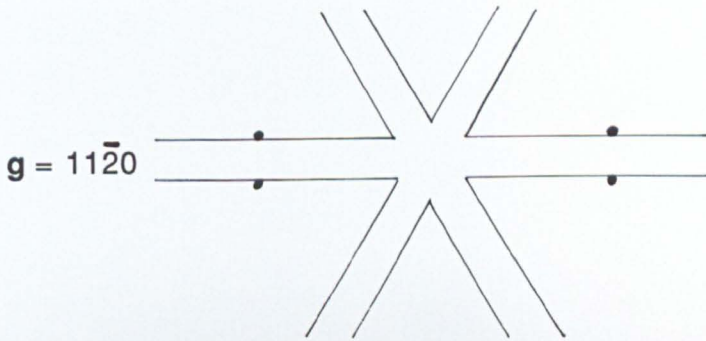


Fig 5.3: W.S.S theoretical depth chart.

The following page shows figure 5.4, a typical pair of micrographs from a stereo pair analysis of S₁ α-titanium.

The irradiation condition shown is 150 keV Sb₃⁺ ions implanted to a dose of 5 x 10¹¹ ions / cm².

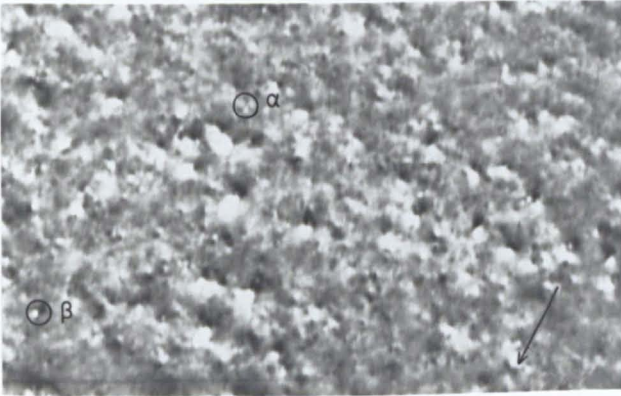
To ease analysis the irradiated side has been decorated with gold islands.



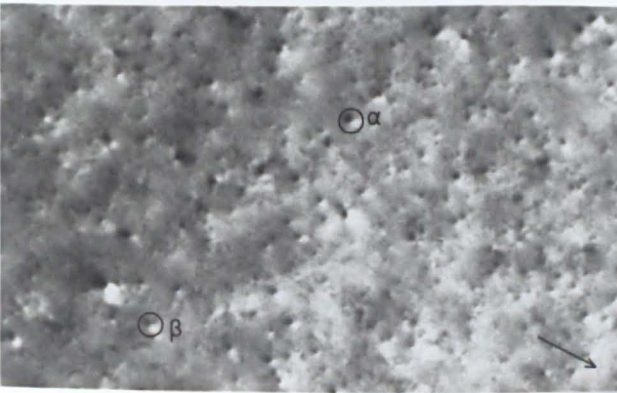
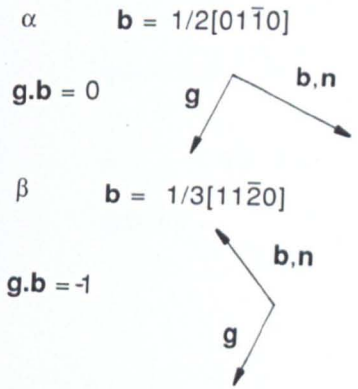
1000Å

The following pages comprise figure 5.5 showing a typical series of micrographs for an analysis of S₁ α-titanium.

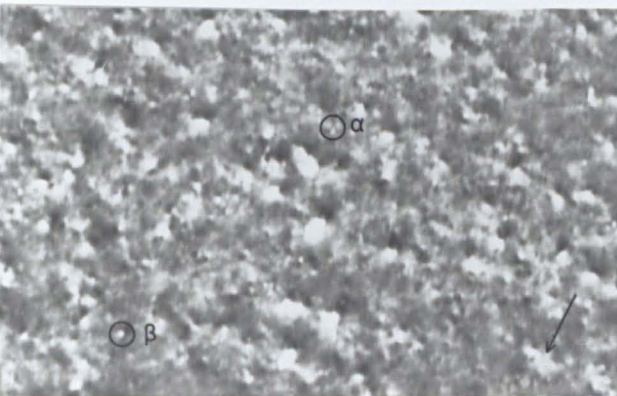
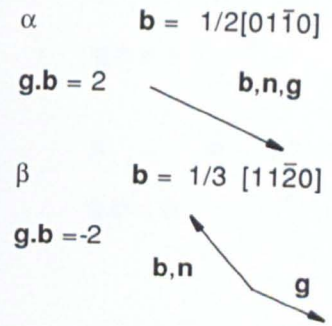
The irradiation condition shown is 150 keV Sb₃⁺ ions implanted to a dose of 5×10^{11} ions / cm².



$g = \bar{2}110$

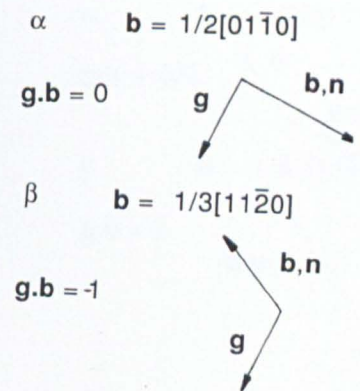


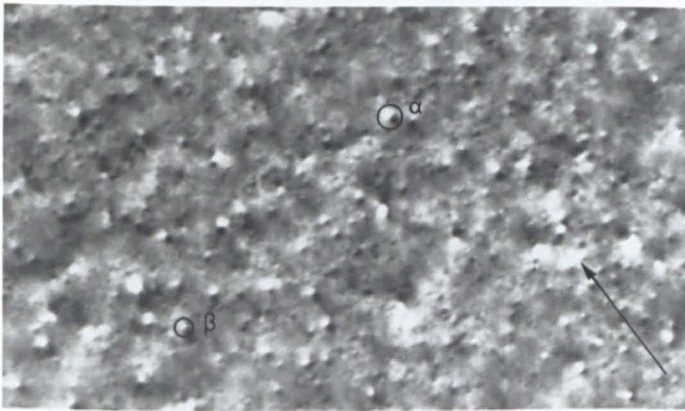
$g = 0\bar{2}20$



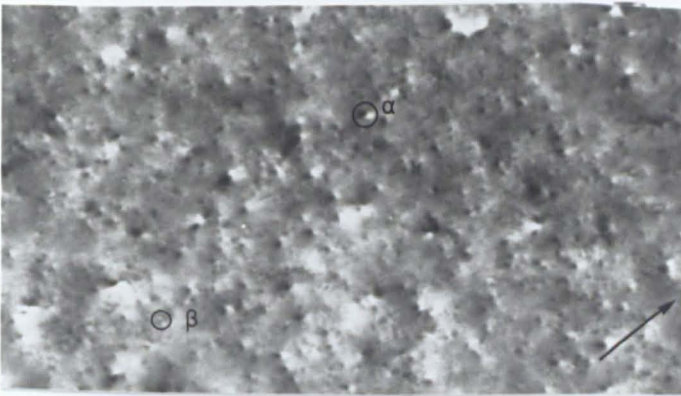
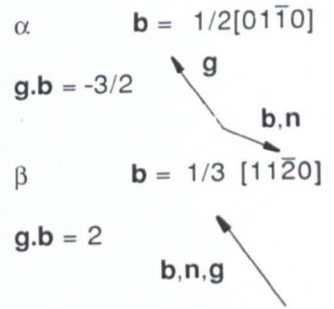
$g = \bar{2}112$

1000 Å

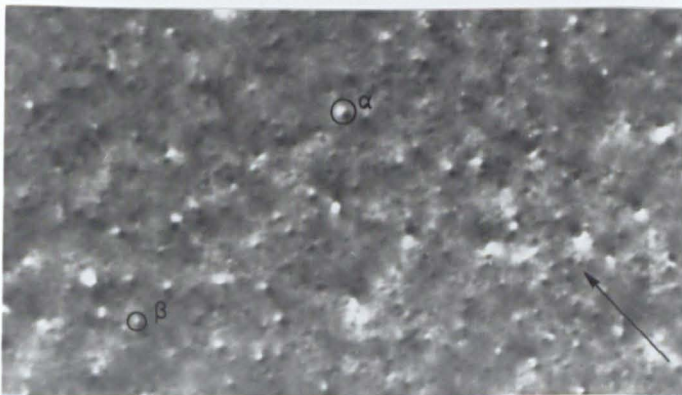
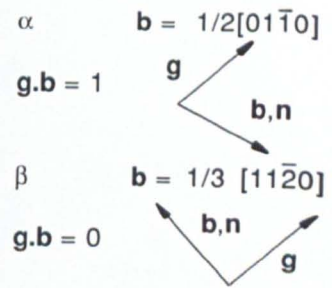




$g = 11\bar{2}0$

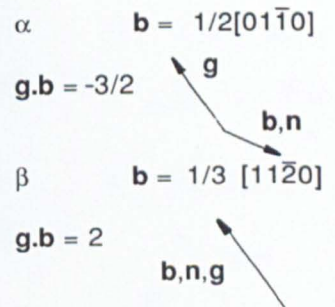


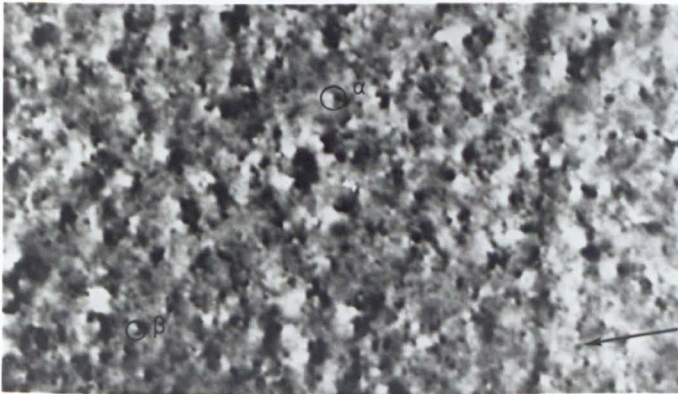
$g = 2\bar{2}00$



$g = 11\bar{2}2$

1000 Å

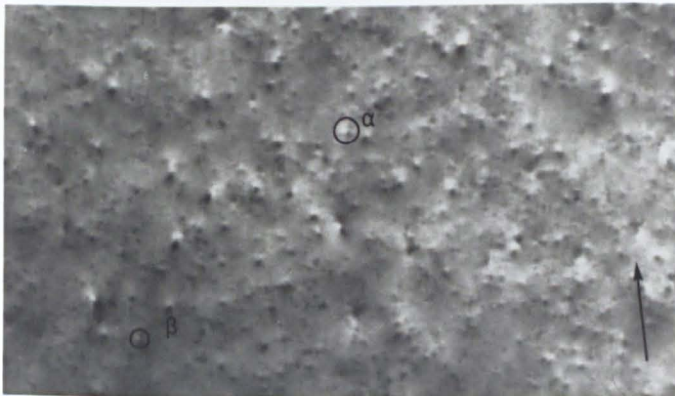




$g = \bar{1}2\bar{1}0$

$\alpha \quad b = 1/2[01\bar{1}0]$
 $g \cdot b = -3/2$ g b, n

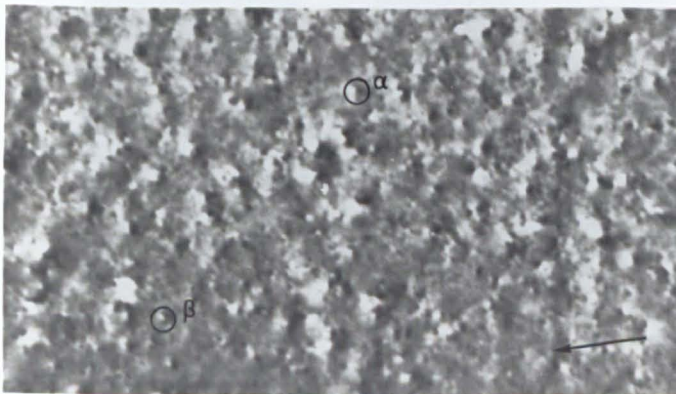
$\beta \quad b = 1/3 [11\bar{2}0]$
 $g \cdot b = 1$ g b, n



$g = \bar{2}020$

$\alpha \quad b = 1/2[01\bar{1}0]$
 $g \cdot b = -1$ g b, n

$\beta \quad b = 1/3 [11\bar{2}0]$
 $g \cdot b = 2$ g b, n



$g = \bar{1}2\bar{1}2$

$\alpha \quad b = 1/2[01\bar{1}0]$
 $g \cdot b = -3/2$ g b, n

$\beta \quad b = 1/3 [11\bar{2}0]$
 $g \cdot b = 1$ g b, n

1000 Å

Loop normals for the perfect population in titanium irradiated with 150 keV Sb_3^+ ions.

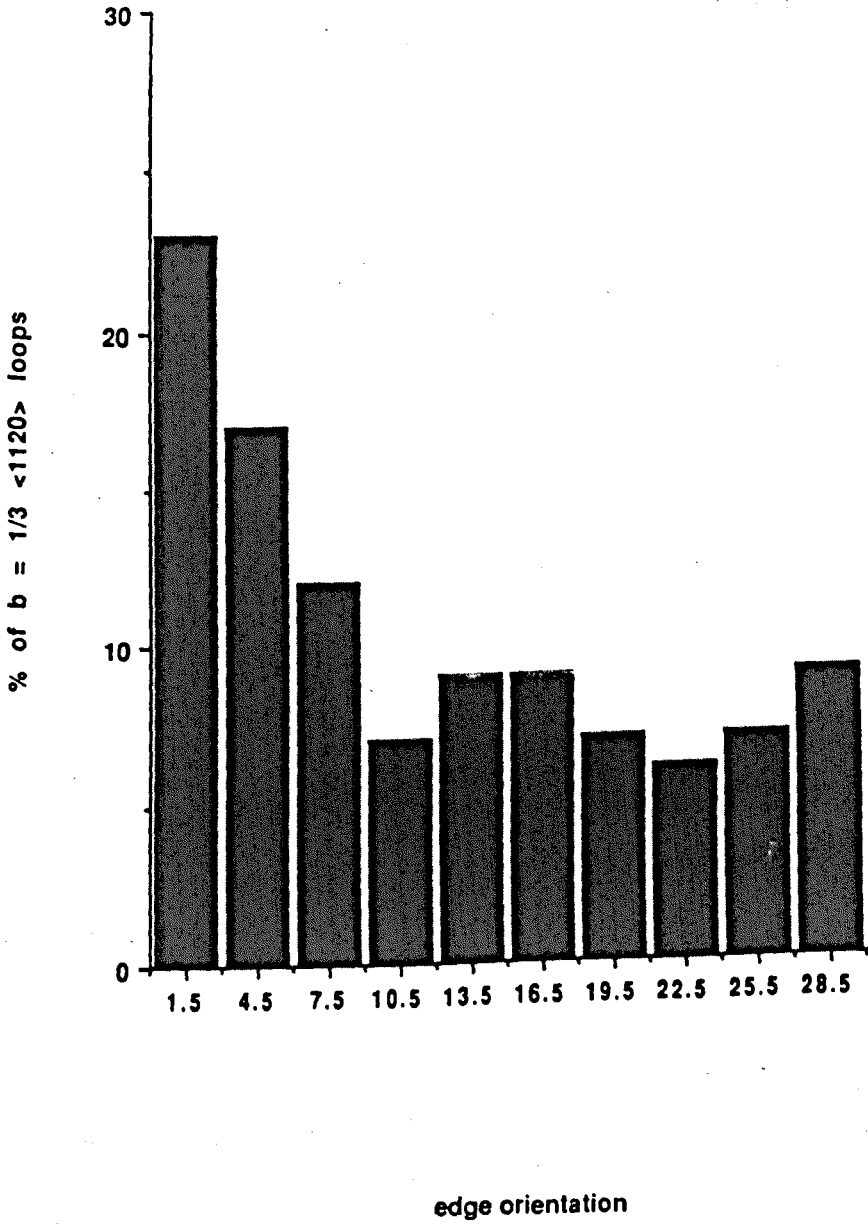
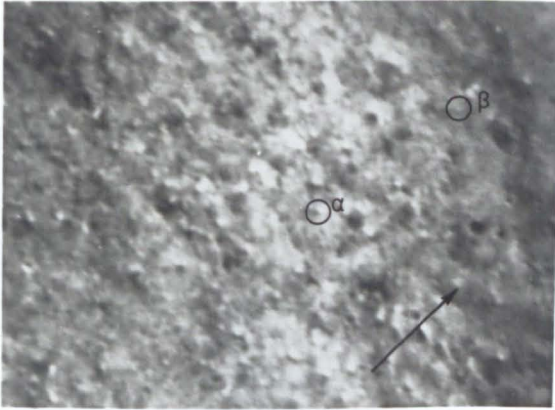


Fig 5.6: Loop normals.

Fig. 5.7. A typical series of micrographs for an S_3 analysis of α -titanium.

The irradiation condition shown is 150 keV Sb_3^+ ions implanted to a dose of 5×10^{11} ions / cm^2 .



$$g = 2\bar{1}\bar{1}0$$

$$\alpha \quad b = 1/2[10\bar{1}0]$$

$$g \cdot b = 3/2 \quad \nearrow \quad b, n, g$$

$$\beta \quad b = 1/6 [02\bar{2}3]$$

$$g \cdot b = 0 \quad \begin{array}{l} \nearrow g \\ \searrow b, n \end{array}$$



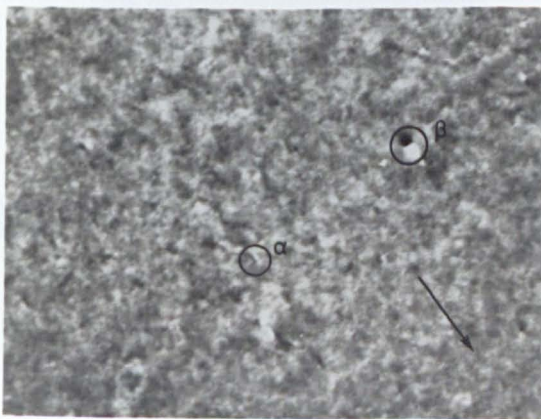
$$g = 20\bar{2}0$$

$$\alpha \quad b = 1/2[10\bar{1}0]$$

$$g \cdot b = 2 \quad \nearrow \quad b, n, g$$

$$\beta \quad b = 1/6 [02\bar{2}3]$$

$$g \cdot b = 2/3 \quad \begin{array}{l} \nearrow g \\ \searrow n \\ \quad \quad \quad \searrow b \end{array}$$



$$g = 0002$$

$$\overbrace{\hspace{2cm}} \\ 1000\text{\AA}$$

$$\alpha \quad b = 1/2[10\bar{1}0]$$

$$g \cdot b = 0 \quad \begin{array}{l} \nearrow b, n \\ \searrow g \end{array}$$

$$\beta \quad b = 1/6 [02\bar{2}3]$$

$$g \cdot b = 1 \quad \begin{array}{l} \nearrow b \\ \searrow n, g \end{array}$$

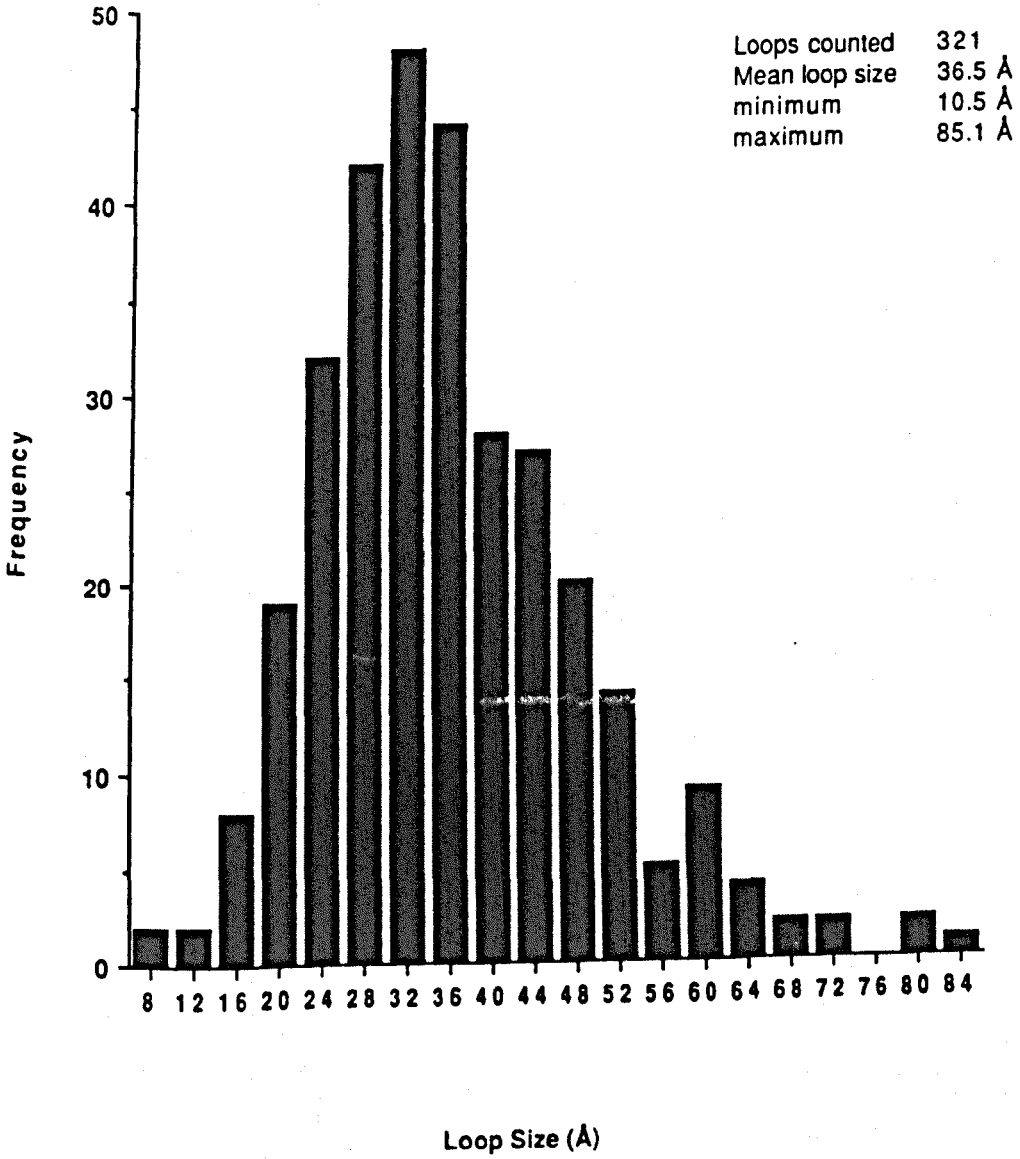


Fig 5.8 Loop sizes for 150 keV Sb_3^+ ions in S_1 iodide Tl.

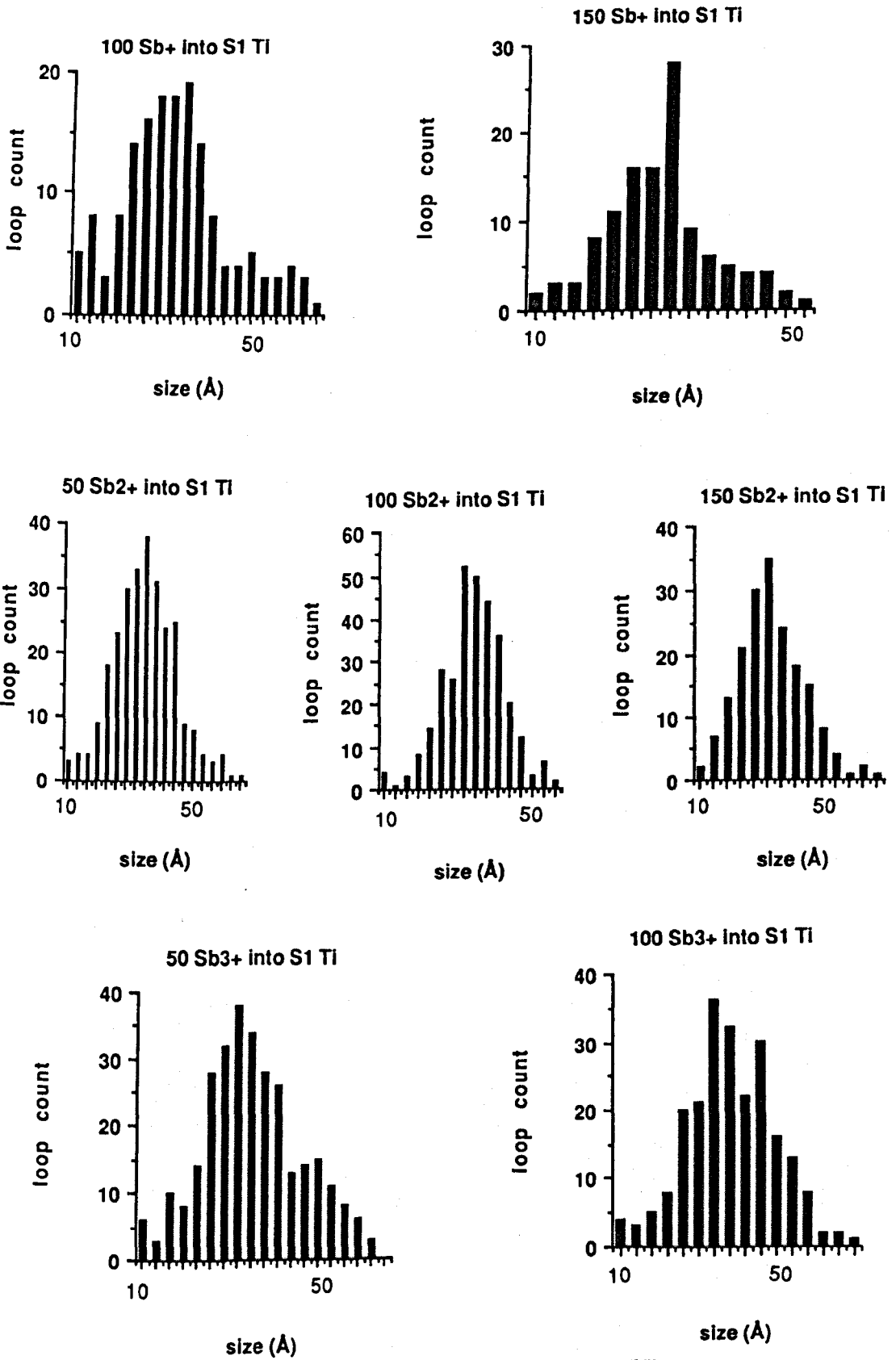
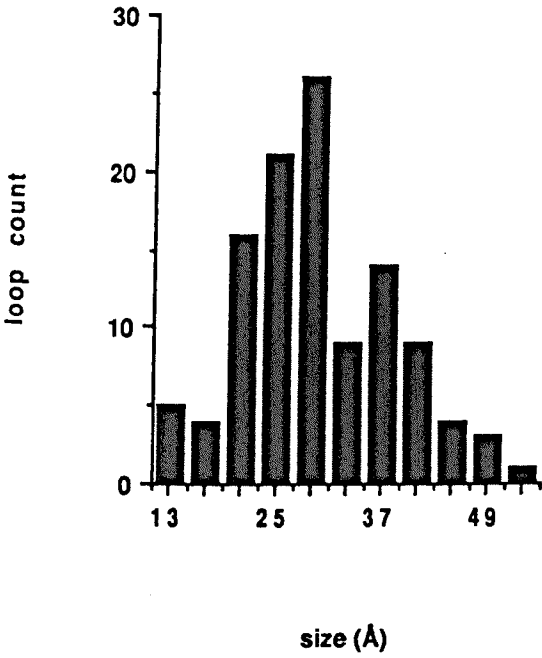
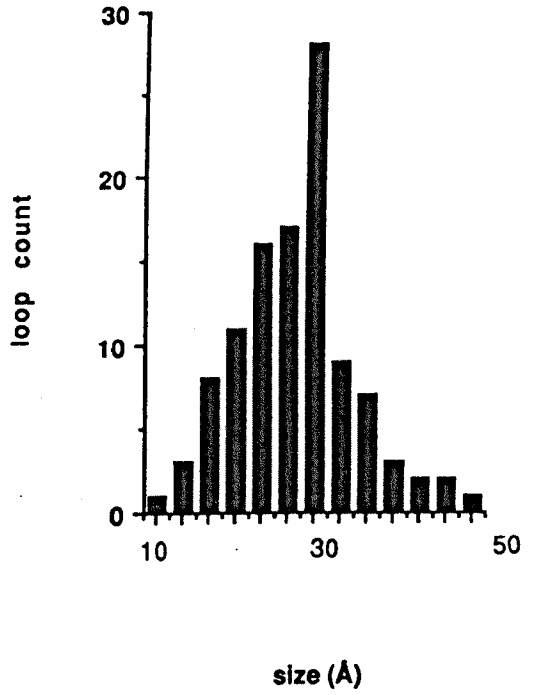


Fig 5.9: Loop sizes for S₁ iodide Ti.

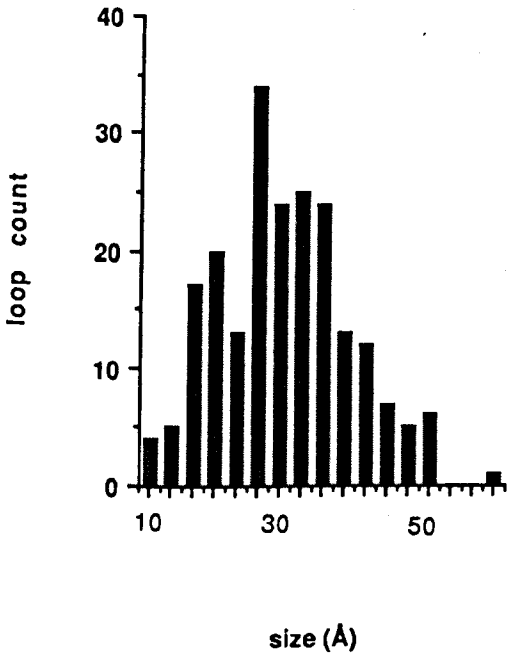
100 Sb²⁺ into S₃ Ti



150 Sb²⁺ into S₃ Ti



100 Sb³⁺ into S₃ Ti



150 Sb³⁺ into S₃ Ti

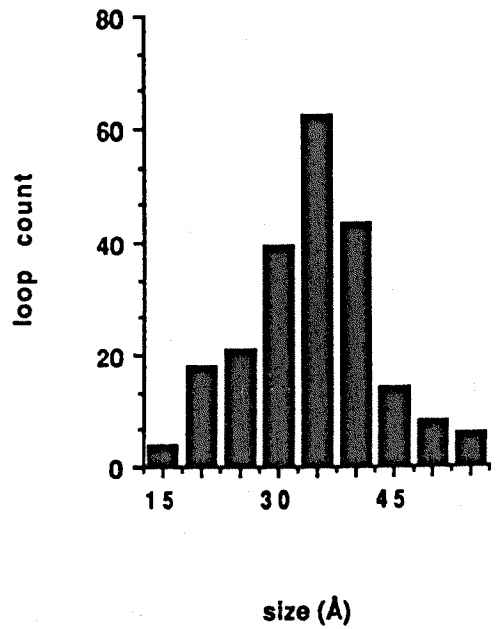


Fig 5.10: Loop sizes for S₃ iodide Ti.

Yield and efficiency for S1 iodide titanium

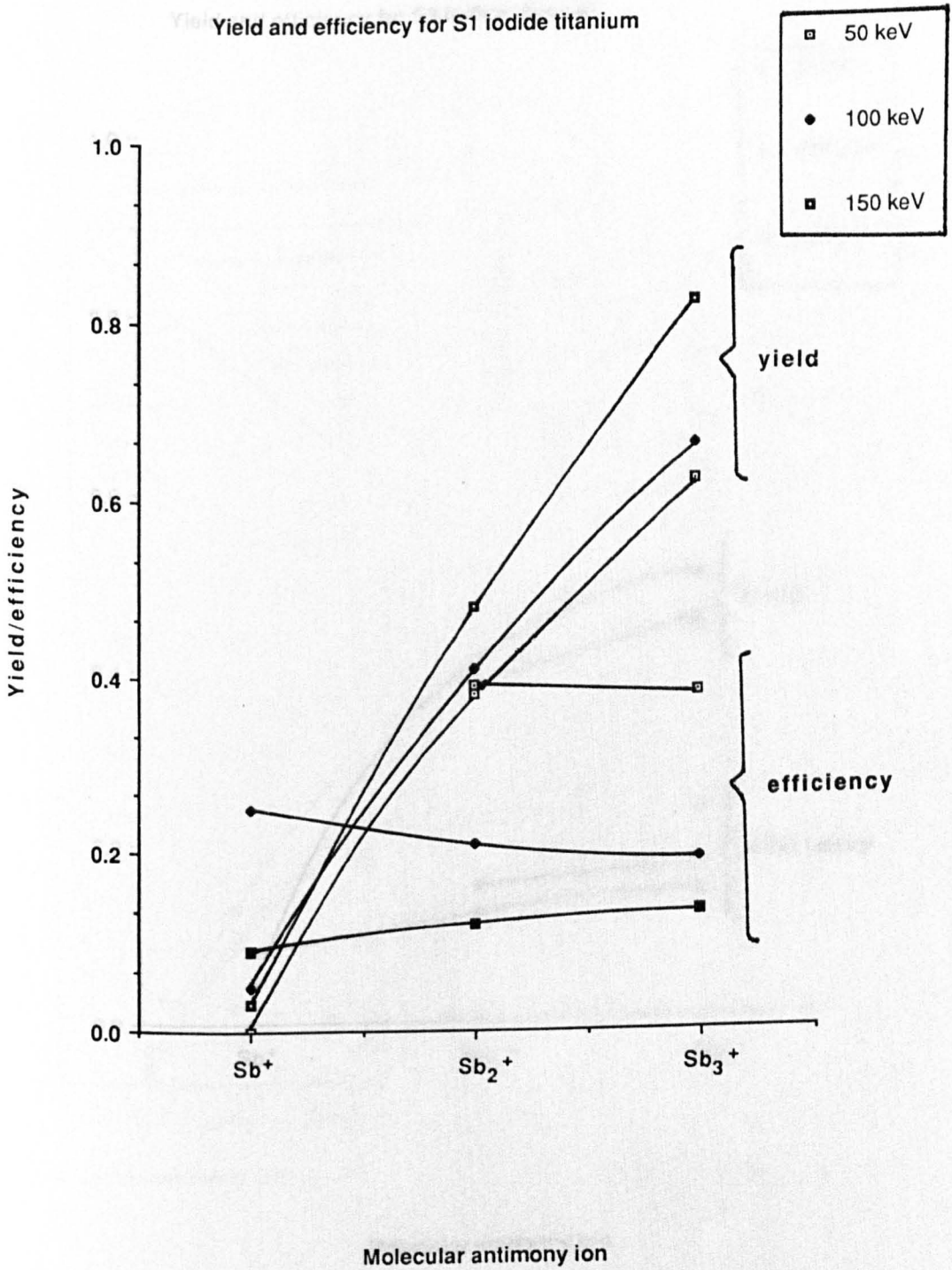


Fig 5.11: Chart of d.y and e for Ti (S_1).

Yield and efficiency for S3 iodide titanium

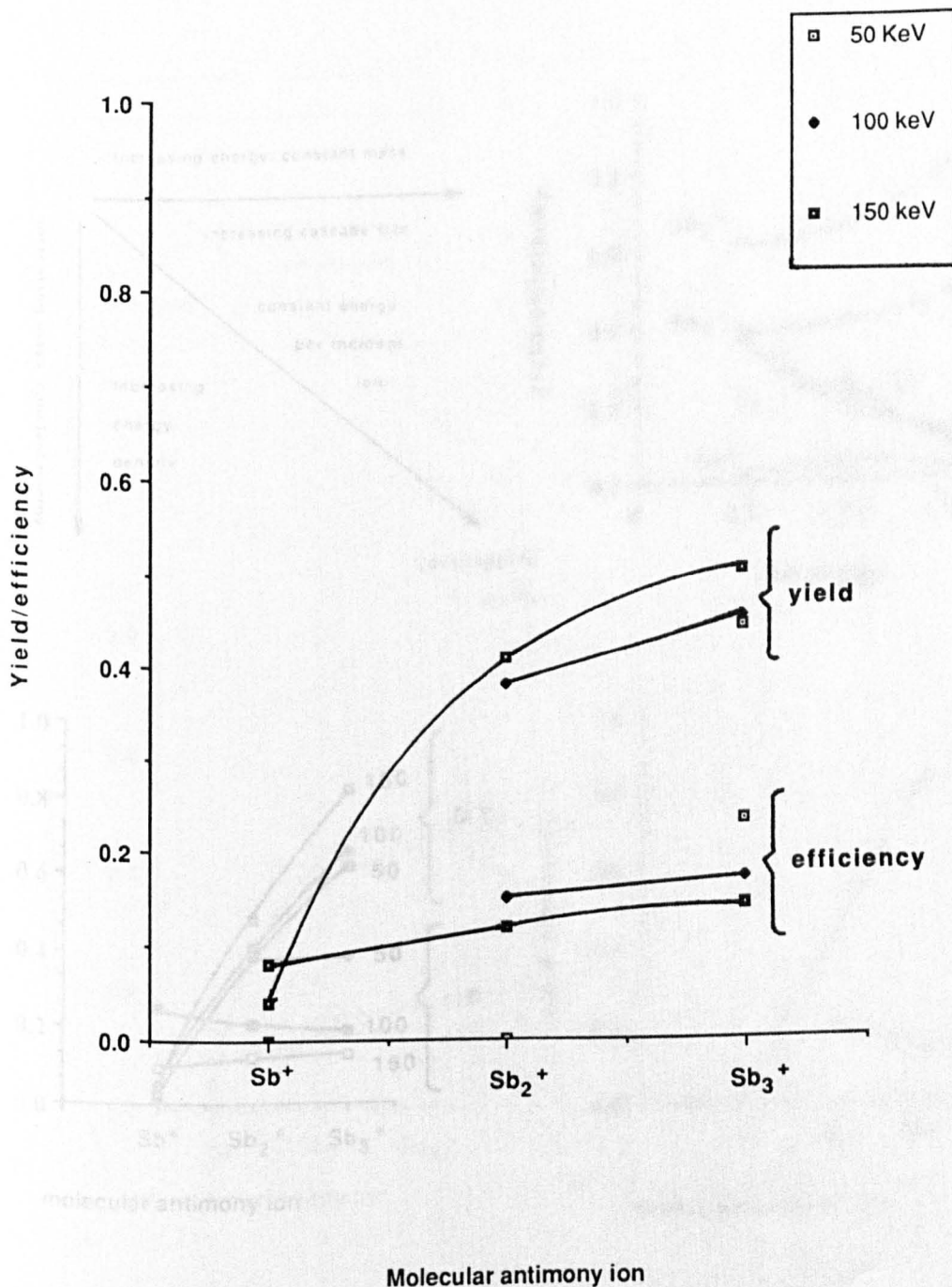


Fig 5.12: Chart of d_y and ϵ for Ti (S_3).

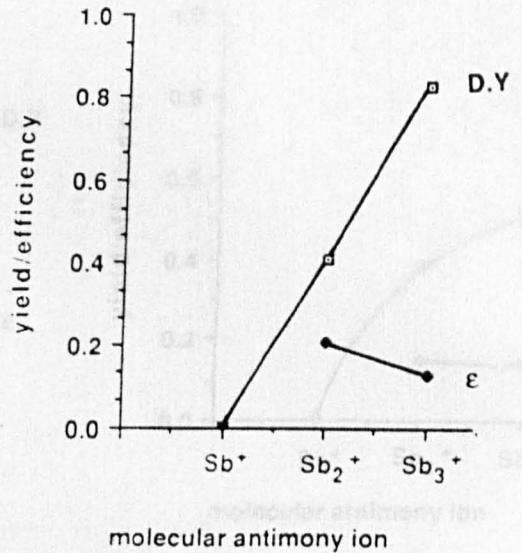
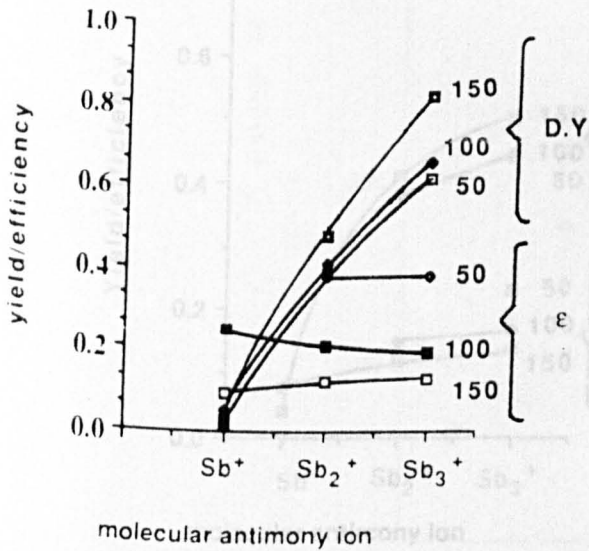
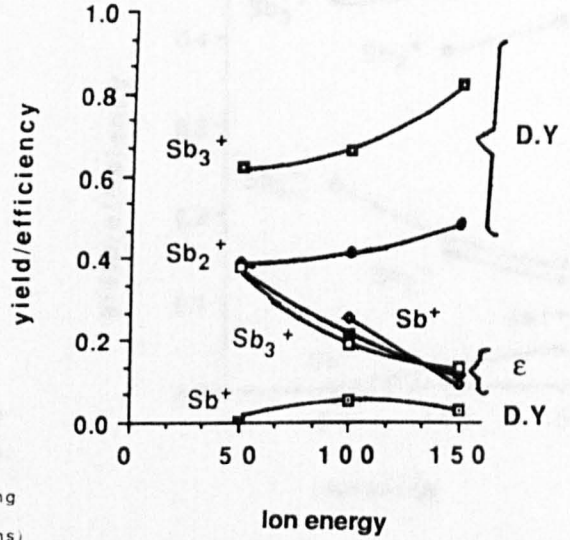
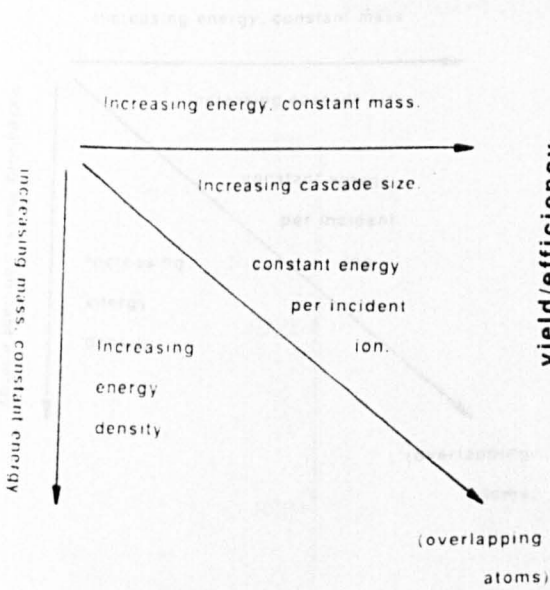


Fig 5.13: Irradiation parameters vs d.y and ϵ for S_1 iodide Ti.

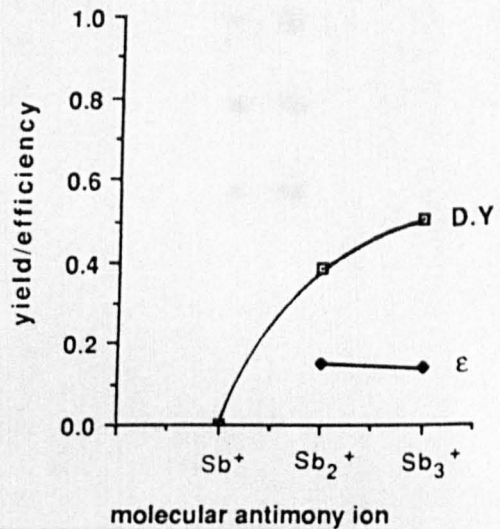
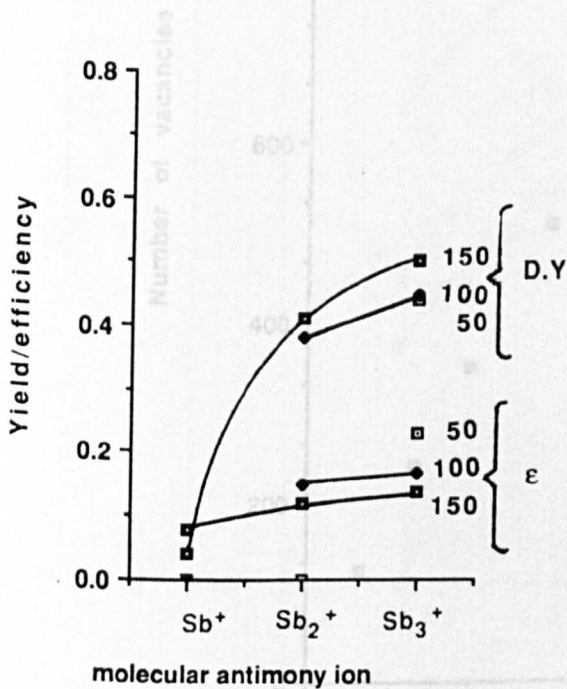
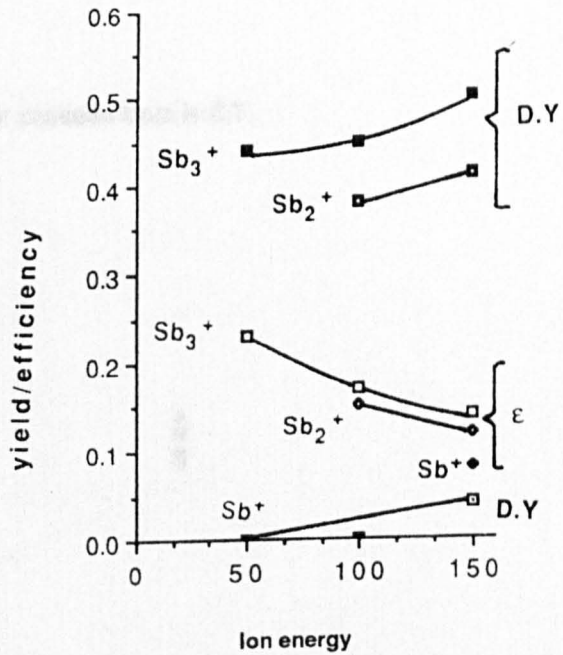
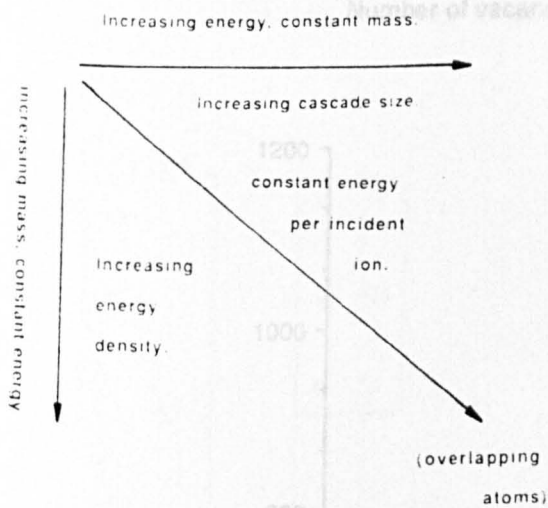


Fig 5.14: Irradiation parameters vs d.y and ε for S₃ iodide Ti.

Cascade Number of vacancies per cascade from N.R.T

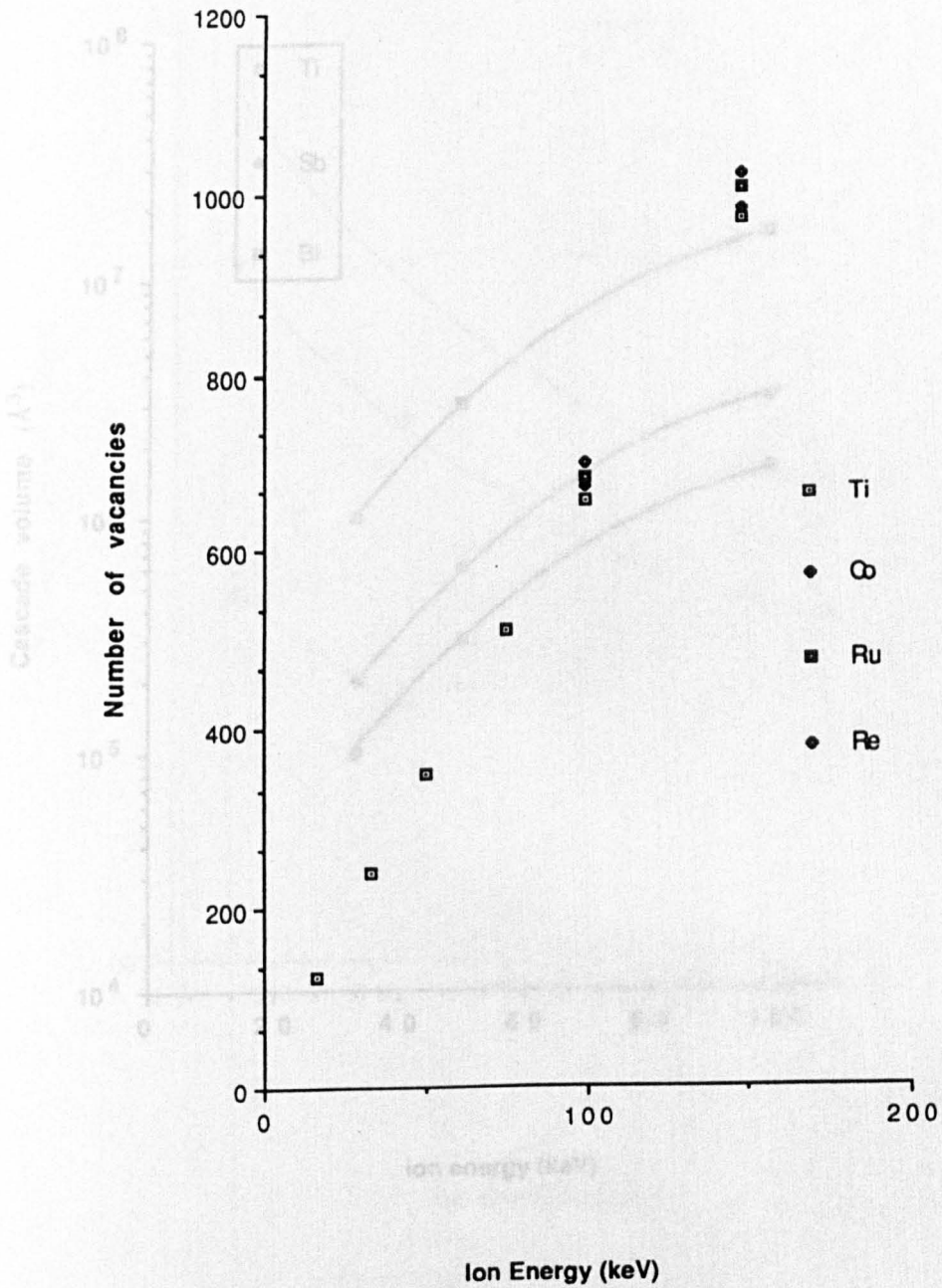


Fig 5.15: N.R.T theoretical damage estimates.

Cascade volume for titanium irradiated with various ions.

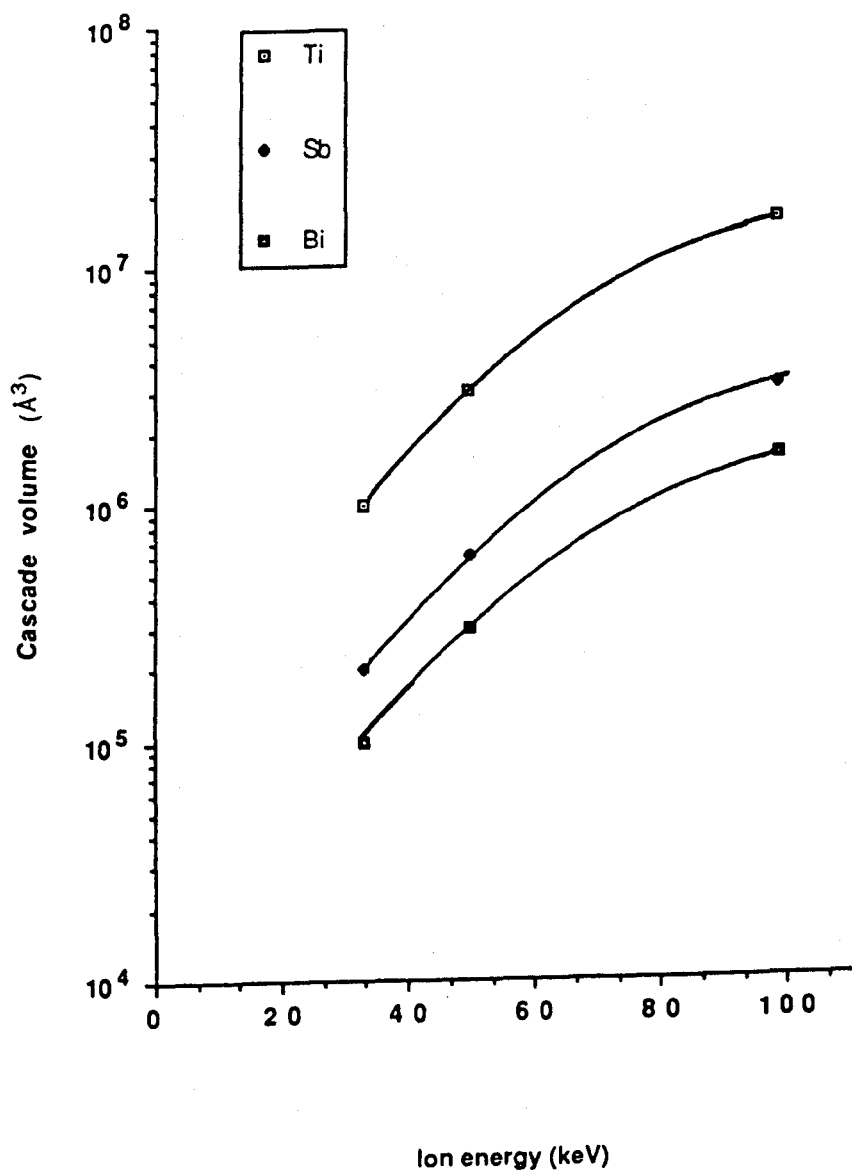


Fig 5.16: Cascade volume per ion for Ti.

Vacancy Concentration vs Ion Energy for various Incident Ions

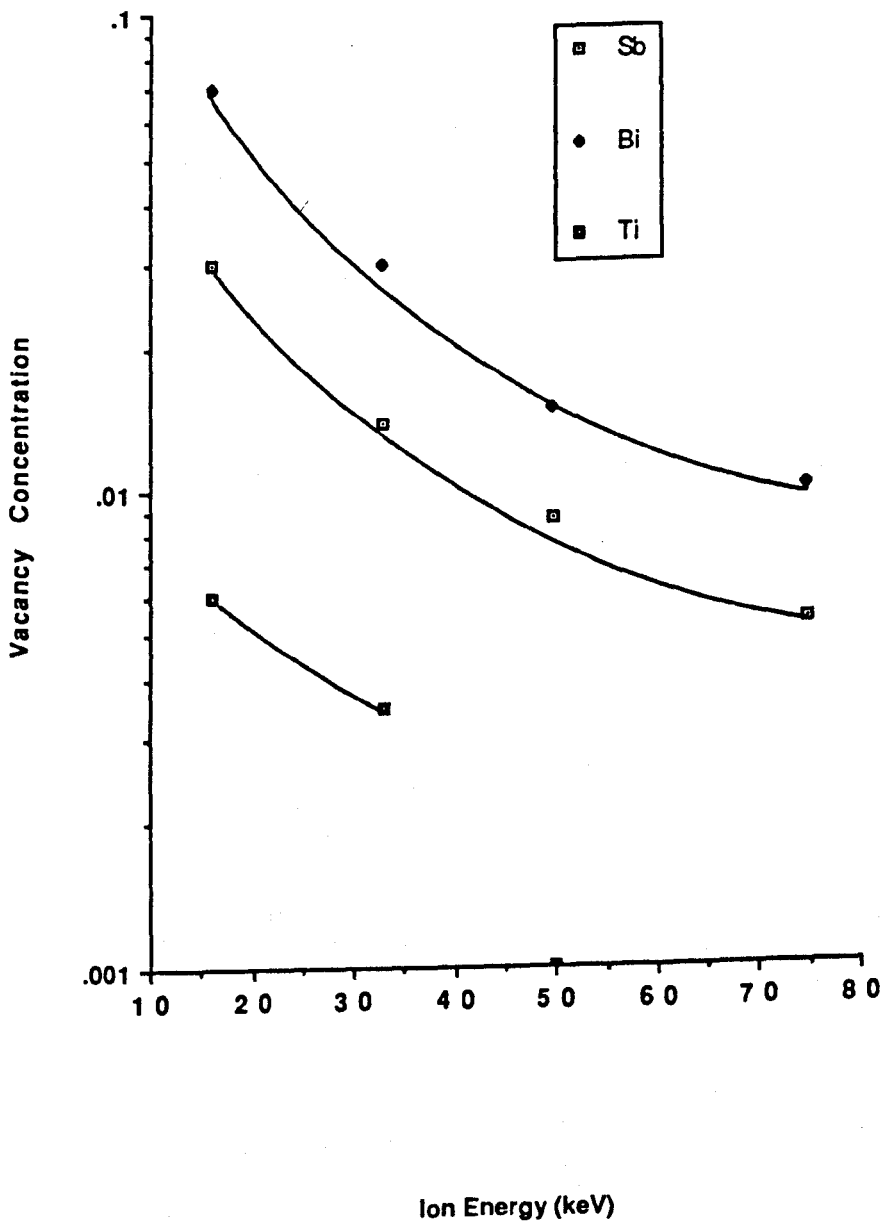


Fig 5.17: Vacancy concentration per ion for Ti.

The following micrographs comprise figure 5.20, showing a typical micrograph for each metal irradiated, here for the case of 150 keV incident ions.

Energy Density vs Ion Energy for various Incident Ions

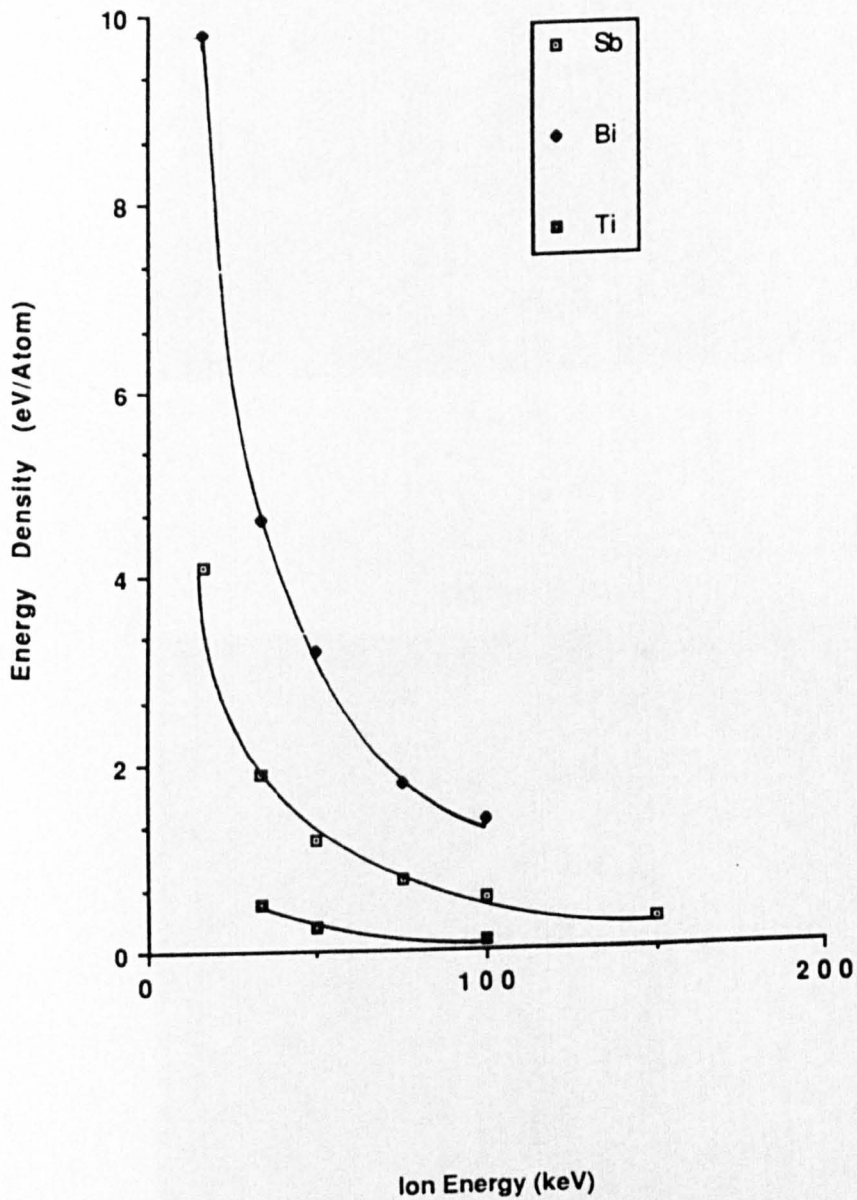
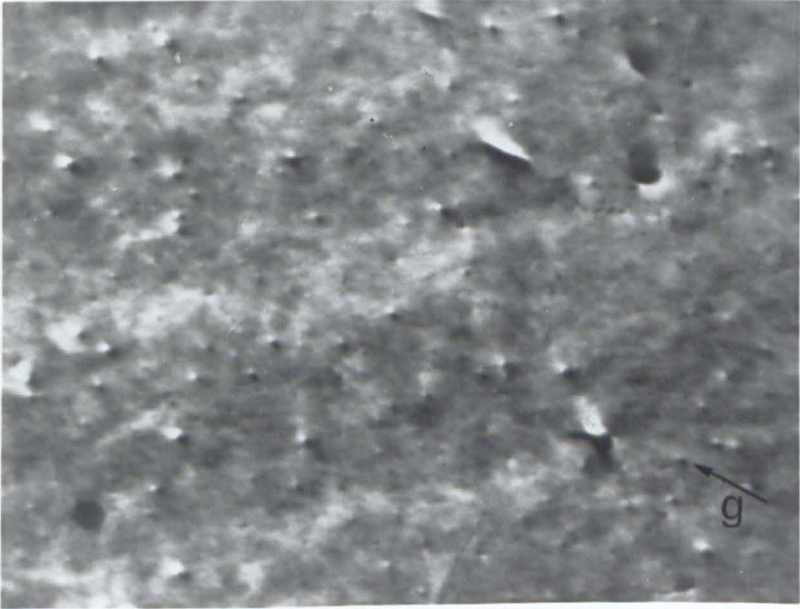


Fig 5.18: Energy density per ion for Ti.

The following micrographs comprise figure 5.20, showing a typical micrograph for each metal irradiated, here for the case of 150 keV antimony ions.

Cobalt



1000Å



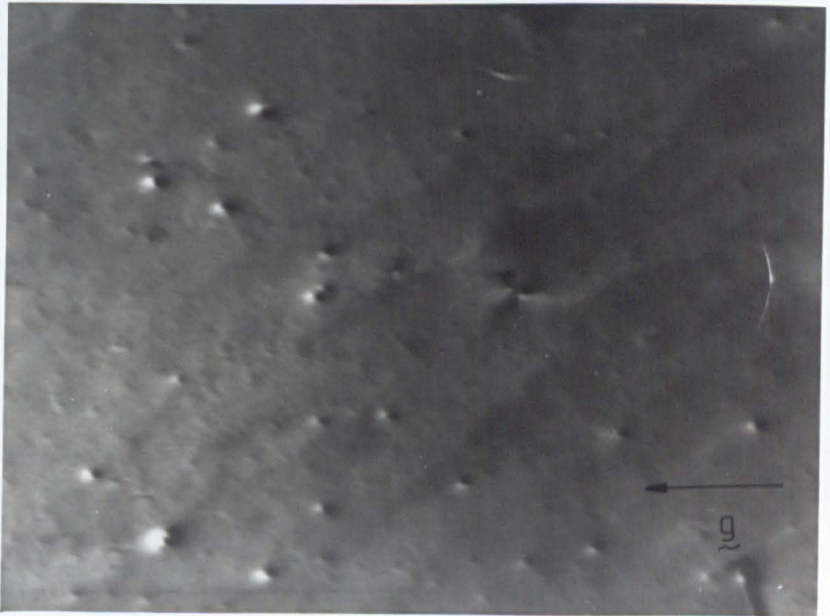
Magnesium



Rhenium



1000Å



Ruthenium

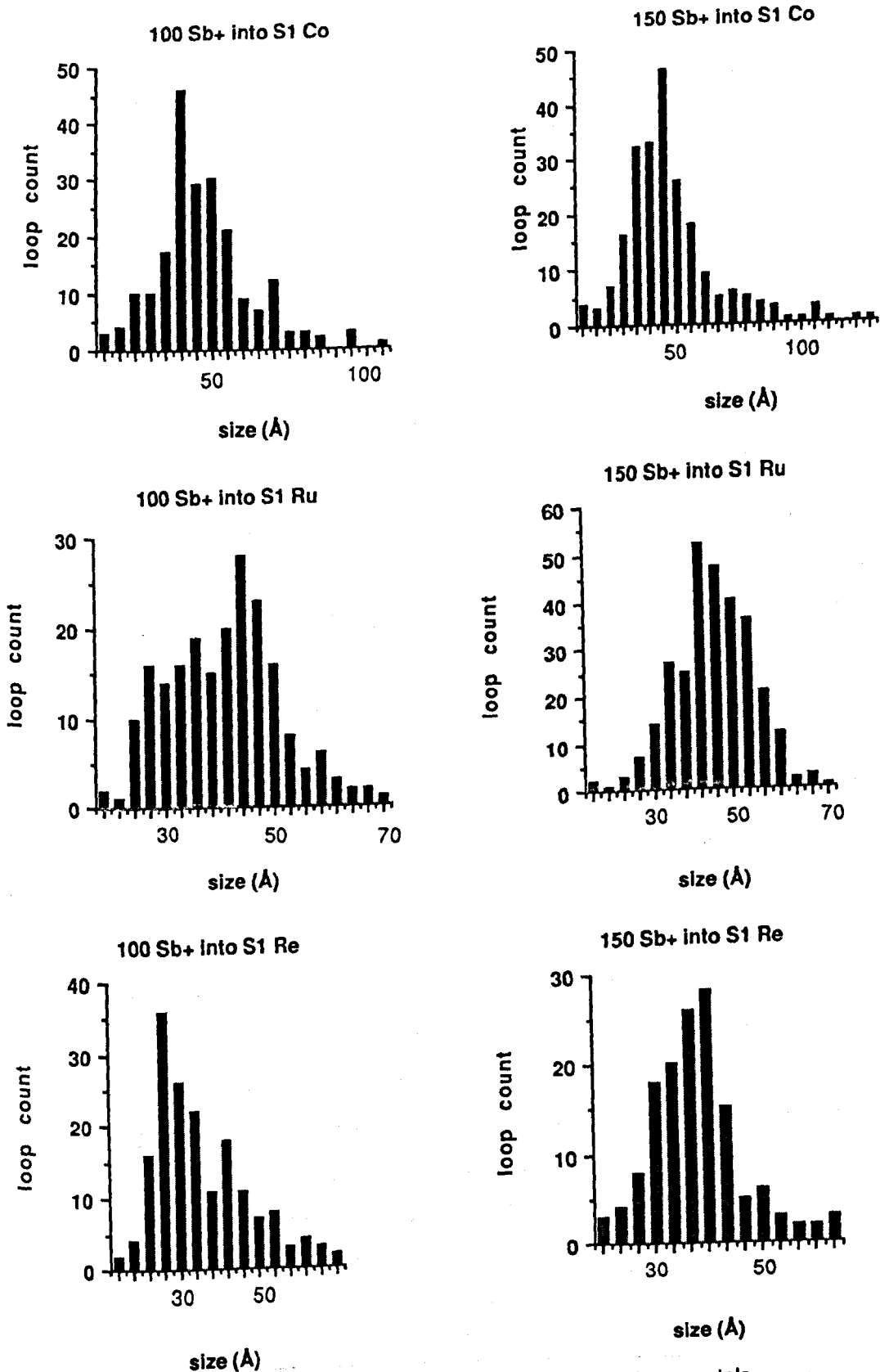


Fig 5.21: Loop sizes for the range of h.c.p. metals.

Chapter 6 Cascade collapse in titanium.

6.1 Introduction.

In this chapter the results of the irradiations performed on titanium will be discussed and explanations for the observed behaviour will be proposed based on the existing cascade models. A thorough investigation into cascade collapse in iodide α -titanium has been made and the variations in the amount and type of damage observed with incident ion energy and type will be discussed. The further results encompassing a range of h.c.p metals will be considered in chapter seven.

Initially, self-ion irradiations were utilised, since these are representative of the p.k.a's produced by neutron irradiation. However, these irradiations produced no visible damage, even for 100 keV implants at doses as high as 10^{12} ions/cm², suggesting that titanium may behave in a similar fashion to iron, in that cascade collapse is difficult to produce, but above a critical cascade energy density loops may form. As the primary aim of this study was to investigate the vacancy component of radiation damage, it was therefore decided to raise the energy density of the cascades produced by bombarding with heavier ions rather than to merely continue raising the dose, which would eventually result in the formation of interstitial loops. In an attempt to ensure the production of visible dislocation loops, the conditions used by Woo & Carpenter (1983) in their brief investigation of bismuth-ion irradiated titanium were repeated. Irradiation to a relatively high ion dose of 1×10^{12} ions/cm² of bismuth ions resulted in only a very low observed defect yield of ~ 0.05 . At this early stage it became clear that for meaningful analyses of the varying loop populations, it would be beneficial to use conditions which could produce a greater range of defect densities while still producing visible dislocation loops. To increase the probability of cascade collapse to form dislocation loops, and thus create a higher density of dislocation loops, the energy density of the individual cascades must be increased, and this was achieved through the implementation of a programme of

molecular antimony ion irradiations. This species was chosen since molecular ions up to Sb_3^+ are easily attainable in the Lintott ion implanter. This method of investigation also provides the inherent advantage of allowing direct comparison with a different crystallographic system, since a series of molecular antimony ion irradiations of molybdenum have been performed by English and Jenkins (1987). Consideration will be taken of the fact that molecular ions dissociate on impact with the lattice and thus do not behave in exactly the same manner as single ion irradiations of equivalent mass later in this discussion.

6.2 Loop Depth.

From the depth measurements recorded for S_1 irradiated iodide titanium, all the damage seen lies within the first layer (i.e within 0.25 of an extinction distance of the surface). From the sign of the $g \cdot I$ product the loops were therefore determined to be vacancy in nature. It should be noted that in zirconium, hydride precipitates produce contrast very similar in nature to that seen for small dislocation loops. However the fact that in the present work contrast is only seen in a narrow band close to the ion-beam entry surface where the cascade damage is expected from range calculations, and later as confirmed by experimental depth measurements, coupled with the absence of black-white contrast in well annealed unirradiated foils, demonstrates that both hydride formation and electron damage are not problematic in titanium. A rigorous identification confirming the vacancy nature of the observed contrast in each irradiation case was therefore deemed unnecessary. Onset of interstitial loop types will be betrayed by the presence of reversals of the black-white images on the micrographs, so care was taken to check for any evidence of this in all the irradiations performed.

The damage depth distributions observed were in all cases Gaussian in shape, as illustrated in Fig 5.2 for the S_1 iodide titanium irradiations, the metal found to have the greatest range of those used in this study. The experimental depth measurement trends are in broad agreement with those predicted by the W.S.S theoretical

calculations (fig 5.3). In all cases the damage depth turns out to be larger than that predicted by W.S.S for the Sb_3^+ irradiations, the difference being larger than the calculated error. This may be indicative of the presence of an oxide layer formed after irradiation and hence resulting in an artificially high observed depth. Additional evidence for a post-irradiation oxide layer stems from the absence of any defects within the first 40 Å of the surface in all of the foils examined. However up to this distance from the surface the forces on the loops may well be large enough for all these loops to be lost by glide, thus resulting in the observed defect free zone (it is extremely unlikely that climb will occur, it can be calculated that it would take more than 10,000 years per atomic jump for a loop under no external stress to climb out of the foil in titanium). Alternatively the observed damage depth may be increased due to the loss of all loops within a certain distance of the surface. This would produce the effect that the ions producing the shallowest loops will vary the most in a comparison of W.S.S calculation and experimental observation since more near surface loops will be lost. From the results it can be seen that there is some evidence that this is occurring. However the Sb_2^+ irradiations are seen to lie significantly below the range calculations, thus pointing to a molecular ion effect. Interestingly Jäger and Merkle (1988) note that the damage depth increased in gold for 20 keV Bi_2^+ irradiations in comparison with the equivalent 10 keV Bi^+ irradiations. This increase in depth was also noted to occur in silicon and germanium by Ruault and Jäger (1980) as well as being observed in the present study of titanium. Thus this effect is not attributable to one specific crystal structure. It appears that as the incident ion disociates on impact into its constituent atoms, one atom will in general collide with the lattice fractionally ahead of the others, and this atom appears to "clears a path" since the lattice atoms will now be in motion (generally away from the incident ions due to conservation of energy). This could allow the other atoms of the molecule to penetrate deeper into the foil before the cascade process occurs by facilitating easier access to channelling and quasi-channelling directions. This effect would be associated with subcascade development

since one atom of the ion will produce collapse much closer to the surface. A different result is seen in titanium however since single ions are unlikely to produce cascade collapse, and complete dissociation of an Sb_2^+ ion is likely to lead to no visible loop formation, while dissociation of an Sb_3^+ ion to an Sb_2^+ and a single atom may lead to one vacancy loop being formed deeper in the foil. Thus subcascade formation due to this effect may only be observed for Sb_4^+ ions, which are not achievable at present. As noted earlier, Gemmel (1974) predicts a shorter range for molecular ions in comparison to single ions, and since his calculations vary from the real case in that they cannot allow for this molecular effect of clearing a path, the increase in depth due to this effect must actually be even larger than is at first apparent. It therefore seems unlikely that this effect is in any way attributable to experimental error. No deep loops were observed in titanium as opposed to Jägers' observations in gold. Again this points to the absence of subcascade formation in titanium. It is also possible from this evidence that R.C.S and channelling distances may be shorter in h.c.p materials, and further proof for this behaviour from the loop sizes and lack of sub-cascade formation will be discussed later in this chapter

Any high energy density cascades occurring close to the foil surface may result in a "crater" type structure as observed by English and Jenkins (1987) in their high energy molecular ion irradiations of molybdenum. This effect has not been noted in this study, suggesting that the energy densities achieved in titanium are not high enough for this phenomenon to occur.

Woo and Carpenter (1983) in their earlier study of heavy-ion damage in titanium did not perform any depth measurements, but were reliant on theoretical range calculations for their erroneous assumption that the damage lay in the second layer, and this may well have been their downfall. A full set of extinction distance calculations for the range of h.c.p metals are given in table 4.4 and from this we see that the second layer corresponds to a depth of at least 585 Å for iodide titanium imaged using the $\mathbf{g} = 20\bar{2}0$ diffraction vector. Since no damage was measured to lie further than 250 Å into the foil this leads to the conclusion that Woo and Carpenter

were either observing interstitial loops or they had wrongly assigned their g vector. Since these results are therefore in some doubt and also as the starting material was of unknown purity and polycrystalline in nature, they will not be considered further.

6.3 Loop Geometry.

Having established that the contrast obtained in the electron microscope is exclusively due to the presence of vacancy dislocation loops, attention now turns to the varying loop geometries observed in heavy-ion irradiated titanium. As described earlier this process involves the comparison of computer generated simulations with a variety of T.E.M images of varying g 's, which enables us to determine the geometry and habit plane uniquely for each observed loop.

6.3.1 Faulted and Perfect Loops..

Considering firstly the case of the S_1 orientation, the dislocation loops are seen to consist exclusively of prism plane loops. In the light of previous studies this is unsurprising since the c/a ratio of titanium is less than ideal. Furthermore, as observed by earlier workers on h.c.p metals (e.g Föll and Wilkens 1977, Phythian 1985), a twin population of both perfect and faulted prism loops was observed, and as expected the main variation of loop type occurs due to loop size. The smaller loops were noted to be mostly of the faulted type while the larger ones were predominantly perfect, and this is consistent with the accepted picture of loops initially forming on the densely packed $\{10\bar{1}0\}$ planes as faulted $b = 1/2\langle 10\bar{1}0 \rangle$ loops and then, if energetically favourable, unfauling to form $b = 1/3 \langle 11\bar{2}0 \rangle$ perfect loops. From elastic energy considerations the larger loops will be more likely to unfault, thus producing the observed variance in size of the two populations.

From table 6.1 it can be seen that there is a remarkable consistency in the ratio of perfect to faulted loops produced by each irradiation condition, especially when the populations have been adjusted to allow for perfect loop loss (the adjustment calculations are discussed in section 6.6.ii). That is the ratio of perfect to faulted loops in titanium is not sensitive to incident ion energy and mass. Systematic loss of

large perfect loops in every condition studied cannot be ruled out at this stage, and this will be discussed later in relation to the observations in S_3 iodide titanium. The established trends that loops nucleate on the closest packed planes, initially faulted, and that loop size is the decisive factor in determining whether unfauling may occur have been confirmed here for iodide titanium.

6.3.11 Loop Normal.

The m vector technique described in chapter 4 has been used to analyse the loop normal for the perfect loop populations observed in this study. Assuming that all of the $b = 1/3\langle 11\bar{2}0 \rangle$ type loops have formed as a result of an unfauling reaction from $b = 1/2\langle 10\bar{1}0 \rangle$ loops then these perfect loops will initially be 30° non-edge, that is they will retain the normal of the original faulted loop. These loops can rotate towards a pure edge orientation, if it is energetically favoured by a reduction of the self energy of the loop. The proximity of the foil surface will influence this reaction and Jäger and Wilkens (1975) have studied this effect in a detailed study of 60 keV gold ion irradiations of tungsten. They applied Häusserman's (1972, a and b) model to explain the unfauling and subsequent rotation to pure edge orientation of the dislocation loops observed. They showed that large loops close to the foil surface are the most likely to unfault and also to subsequently rotate to the pure edge configuration (loops larger than 20 Å in tungsten). In the present study the loop normals for the perfect prism loop population were assessed for the three extremes of irradiation considered, namely high mass and high energy, high mass and low energy and low mass and high energy. (Note that no damage at all is observed for low mass and low energy irradiations.) These were shown in table 5.5. Here we note only a slight trend towards increased pure edge population with increased ion energy but a sharp increase in the ratio of pure edge loops observed on the transition from single ion to molecular Sb_3^+ ion irradiations. This highlights the effects of increasing ion mass by the use of molecular ion irradiations. Molecular ion cascades are noted to be much more likely to result in the production of pure-edge loops. This may be due to the higher energy density of the cascade resulting in a longer thermal spike lifetime

and hence the loops have longer to rotate towards a pure-edge orientation. It is far more difficult however to find a correlation between loop size and the number of pure edge loops observed since these large loops are then by definition likely to be lost to the foil surface prior to analysis. Indeed careful measurement of the size of pure edge and non-edge loops for the case of 150 keV Sb_3^+ ion irradiations reveals no obvious trends (see table 6.2), but since rotation to pure edge perfect loops may occur due to internal stresses produced by imperfections in the crystal indicates this is not completely unexpected. To conclude, these observations are consistent with the behaviour for glissile loops and it seems likely that loop rotation is attributable to thermal spike lifetime rather than loop size and loop depth.

6.3.iii Basal Loops.

The driving force behind studying the S_3 orientation is that it provides the ability to identify any anisotropic behaviour of the material under irradiation due to its crystallographic orientation. Legrand (1984) calculated the stacking fault energy in the basal plane as 290 mJ/m^2 compared with 110 mJ/m^2 for the prism plane, and it is therefore energetically favourable for vacancy loops to agglomerate on the prism planes. Indeed prism loops are observed to constitute the vast majority of loops seen in this orientation. However basal loops have also been identified both in titanium and ruthenium and the reasons for this will be considered here, and also with reference to the results for the range of h.c.p metals in chapter 7.

A full identification of all of the basal plane c-loops is facilitated in this orientation and assimilation of their presence is of great importance in considering current models for irradiation growth in zirconium. The present study has revealed the presence of a very small population of $1/6\langle 20\bar{2}3 \rangle$ vacancy basal loops, not exceeding $\sim 0.5\%$ in any of the irradiations performed. The occurrence of c-loops only in the S_3 orientation is consistent with Phythian's findings in ruthenium.

Griffiths *et al* (1983) speculate that this crystallographic dependence of c-loop formation, first observed in zirconium, can be attributed to a stress relief mechanism arising due to the presence of a surface oxide layer. For materials having

coherent oxides which grow with a volume expansion, tensile stresses will exist in the material due to the oxide. It should be noted that the stress induced by the oxide layer will be far too small for stress-induced preferential nucleation (S.I.P.N) to occur, stress induced preferential absorption (S.I.P.A) of point defects is much more energetically favourable. This implies that if the surface oxide has a role to play in determining the observed loop populations then sub-microscopic c-loops must exist which can then grow due to S.I.P.A in the energetically favoured orientations. This is certainly consistent with the proposed models for growth mentioned earlier (see chapter three), where a contraction in the c-axis together with an expansion in the a-axis implies nucleation of interstitial prism plane loops and vacancy basal plane loops, since large quantities of visible c-loops have not been observed using T.E.M.

Brager *et al* (1977) observed a five hundred per cent increase in the total area of Frank interstitial loops in 316 stainless steel for loop orientations perpendicular to a resolved tensile stress of $\sim 0.3 \text{ GN/m}^2$, thus confirming that internal stresses can have a profound effect on the observed loop populations. The sense of the stress imposed by an oxide on its parent metal is determined from the Pilling-Bedworth ratio (P.B.R), where:

$$\text{P.B.R} = \frac{\text{metal ion volume in oxide}}{\text{metal atom volume in metal}} \quad (6.1)$$

The surface oxide will be in compression if this ratio exceeds one, resulting in a tensile force in the metal acting parallel to the surface, which will favour interstitial loop formation on planes perpendicular to the stress axis. The P.B.R for titanium calculated from powder diffraction data for TiO_2 is ~ 1.75 , thus the oxide film will not induce c-loop formation in the S_3 orientation. This helps to explain the very small number of c-loops observed in the S_3 orientation. Interestingly there is an increase in c-loop population associated with an increase in ion energy and mass, which is as expected since as the ion energy and mass increases so the depth of the dislocation loops beneath the surface also increases thus attenuating the effect of the surface induced stress, in the S_3 case reducing the favourability of prism plane over basal plane vacancy loops.

Some energy barrier may therefore exist inhibiting c-loop formation, especially since c-loops are only observed above a certain critical size which is noted to be much larger than that due to the resolvable size of loops visible in the electron microscope. English *et al* (1980) in a study of molybdenum note that the energetically unfavourable $b = \langle 100 \rangle$ loop is formed more frequently on irradiation with 180 keV Sb_3^+ ions compared with the usual population of $b = 1/2\langle 111 \rangle$ loops observed on irradiation with lighter ions, and indeed energy barriers have been estimated by computer simulation for the b.c.c metals (Matthai and Bacon 1984).

A further possible explanation for this anisotropic behaviour revolves around the observation of double loops (see chapter three) to give perfect glissile c-component Burgers vectors i.e $1/2[0001] + 1/2[0001] = [0001]$, which can be formed by the condensation of a second layer of vacancies onto an existing c-loop. These can then glide out of the foil in the S_1 orientation but may remain in the foil in the S_3 orientation due to the small component of the Burgers vector towards the foil surface. These loops have been observed in electron irradiated cadmium and zinc (Whitehead *et al* 1978), and more pertinently White (1983) detected double $\langle 20\bar{2}3 \rangle$ loops in commercial purity titanium irradiated with 1 MeV electrons at 725 K. Phythian (1985) noted that some c-loops were lost during the analysis of S_3 ruthenium foils. This is inconsistent with their identification as faulted loops since climb to the surface is not feasible during the comparatively short length of time involved in a T.E.M analysis, suggesting that these loops may well be of the unfaulted double loop variety. This could occur if vacancies from an uncollapsed cascade became mobile due to beam heating and thus condensed on an existing c-loop. It should be noted that no such c component loop loss has been observed in titanium, but very few c-loops were observed and since Phythian noted that only 1% of c-loops were lost in this manner in ruthenium, it is statistically probable that further investigation may elucidate this mechanism in titanium.

W.S.S straggling data suggests that the initial cascade region is not circular, but is in fact elongated in the ion beam direction. This could lead to preferential

nucleation of dislocation loops on planes parallel to the ion-beam direction i.e prism plane loops in the S_1 orientation and basal loops in the S_3 orientation. It should be noted however that both computer simulation (Hienisch, 1981 applying the MARLOWE code to copper) and experimental evidence (Pramanik and Seidman, 1983 from F.I.M analysis of tungsten) exists showing that the initial cascade shape is in fact very irregular. Jenkins and English (1982) note from disordered zone analysis that although the cascade becomes more irregular as the ion energy increases, irradiation with molecular antimony ions as used in this study tends to produce more regular cascade regions than comparative single ion irradiations. Preferential loop orientation due to cascade shape seems unlikely though, since it would not account for the observation of c-loops in single-ion irradiated ruthenium although it is consistent with the observation of increasing c-loop population on transition from single to molecular ions seen in titanium. This explanation also fails since we would then also expect a decrease in c-loop population with increasing ion energy whereas exactly the opposite behaviour is in fact observed.

Finally, it is possible that c-loops are not observed in the S_1 orientation simply due to a combination of high loop loss (the Burgers vector points straight towards the foil surface) and poor image quality of basal loops in any of the diffraction vectors available in the S_1 orientation.

6.4 Stacking Fault Energy.

Having determined the relevant populations of the perfect and faulted loop populations, it is possible to make an estimate for the stacking fault energy (S.F.E) of the prism plane in titanium by estimating the critical loop size at which the perfect loop configuration becomes more energetically favourable. To achieve this plots have been made of loop radius versus the probability of finding a faulted loop with a radius larger than the given size in each of the irradiation conditions used. Little difference in unfauling behaviour is noted for the varying irradiation conditions used, and from this constancy it can be concluded that these results are therefore statistically meaningful. It has been assumed that the perfect loops are

produced from an unfauling reaction rather than as a result of some irradiation energy density barrier being surpassed. Thus, by summing the information obtained from every analysis undertaken for each of the crystallographic orientations studied and by taking the critical radius to be that at which 95% of the loops have unfauled, the basal and prism stacking fault energies may be estimated. The 95% limit has been chosen since local strain fields due to imperfections in the crystal can increase the probability of unfauling thus artificially lowering the apparent critical radius. The proximity of the foil surface will also act to increase the likelihood of early unfauling. However with the loop normals almost perpendicular to the foil normal this effect will be minimal and has thus been ignored, although it should be borne in mind that the effect of the surface would be to increase the experimental estimate of the S.F.E.

6.4.1 The Prism Plane S.F.E of Titanium.

The critical radius for 95% of the prism loops to have unfauled in the case of S_1 iodide titanium is found to be $\sim 23\text{\AA}$ (see fig 6.1) using this method, and substituting this value into equation 3.6 together with the following materials parameters for titanium:

$$G = \text{shear modulus} = 45.6 \text{ GPa}$$

$$b_s = a/2 = 1.475 \text{ \AA}$$

$$\nu = \text{Poissons ratio} = 0.34$$

$$r_o = \text{core radius} = 2.95 - 5.9 \text{ \AA}$$

the S.F.E is determined to lie within the range $129 - 184 \text{ mJ/m}^2$. The major source of error here comes from the uncertainty in the value for the core radius. This is at present unavoidable and so the two extreme values are used, and this gives the range estimate for the S.F.E. Two workers have also recently made estimates for the S.F.E on the prism plane in titanium. Legrand (1984) used tight binding calculations to produce a theoretical estimate of 110 mJ/m^2 and more recently Naka *et al* (1988) obtained an experimental estimate from cross-slip data of 132 mJ/m^2 . These values are very encouraging as far as the validity of the present technique is concerned

since they lie well within the experimental errors applicable to the range obtained here.

6.4.II The Basal Plane S.F.E of Titanium.

Only the $b = 1/6\langle 20\bar{2}3 \rangle$ type basal loops with a reduced S.F.E have been observed in titanium, and it is therefore impossible to pinpoint the critical radius at which $1/2\langle 0001 \rangle$ loops will unfault. However, the smallest basal loops identified have a radius of 20 Å, and so we can therefore calculate a lower limit for the S.F.E since the critical unfaulting radius must be smaller than 20 Å. Using equation 3.6 where b_s corresponds to the partial $1/3\langle 10\bar{1}0 \rangle$ and is therefore $a/3$, we find that the basal plane stacking fault energy must be in excess of 136 mJ/m² for the I_1 stacking fault since all of the $1/2[0001]$ loops have unfaulted at this radius. This corresponds to a stacking fault energy > 272 mJ/m² for the I_2 stacking fault, since the basal fault I_2 is approximately twice I_1 in energy (see chapter two). Again this tallies with Legrands calculation which estimates the basal fault I_2 energy to be 290 mJ/m².

6.5.S₁ Orientation Commercial Titanium.

The interest in examining this high oxygen content material arises from the differences observed in loop sizes, populations and numbers due to the presence of a much higher impurity concentration. An increase in oxygen content will effect the characteristics of the material. The α - β transition temperature rises with increased oxygen content, the $[0001]$ lattice parameter c increases by 0.015 per atomic % oxygen content, thus raising the c/a ratio slightly (Finlay and Snyder 1950) and there is a small increase in the melting point of the material. It should also be noted that oxygen is soluble in titanium up to $\sim 10\%$, and thus at the low levels examined in this study no precipitation will occur. Gallagher (1970) found that the stacking fault energy for a large range of nominally pure f.c.c metals decreases with increasing impurity. This behaviour is confirmed for the h.c.p case later in this chapter by utilising calculations based on the loop sizes for the two prism loop

populations observed (see below).

6.5.i Loop Depth.

One condition was analysed, the results can be found in Fig 5.2, where the depth observed is smaller than for similar irradiations of iodide titanium but the two are within experimental errors. No real effect of impurity content can therefore be noted.

6.5.ii. Loop Geometry.

As in the case for the iodide S_1 orientation, both faulted and perfect vacancy prism plane loops were observed after irradiations in this material. Here, however, the loop size is noted to be slightly larger while the perfect loop population is significantly smaller than for iodide titanium. This suggests that the impurity content inhibits unfaulting either by directly reducing the stacking fault energy or by restricting the nucleation of Shockley partials for unfaulting to occur.

6.5.iii Stacking Fault Energy.

Returning to the method used for calculating the S.F.E, we find by summing the data for all the S_1 irradiations performed on commercial grade titanium (see fig 6.1), that the critical size for 95% of the loops to have unfaulted has risen to 28.5 Å. Placing this value into equation 3.6 and assuming all other parameters remain constant the value for the stacking fault energy of the prism plane fault in commercial grade titanium is calculated to lie in the range 119-141 mJ/m². This value is lower than that obtained for iodide titanium which is as expected due to the presence of a high level of oxygen.

English *et al* (1977) performed a systematic study on molybdenum doped with nitrogen and discovered that a nitrogen impurity content of only 17 appm reduced the yield by a factor of five and also halved the efficiency. Similarly Robinson and Jenkins (1981) reported that in 321 stainless steel the yield was observed to decrease significantly in comparison to a ternary alloy of similar composition, thus suggesting that minor alloying or impurity elements can drastically influence the final structure. It is interesting to note that no such trend has been observed either

here or in any other study for h.c.p materials, where a slight impurity concentration may profoundly affect the type of damage structure observed but will not drastically reduce the yield. It is not as yet clear precisely why there is an increase in defect yield with oxygen content, but the anisotropy of the crystal system is again influencing the cascade process. Unfortunately time did not allow for a study of S_3 oriented commercial titanium as it would be interesting to observe whether the yield of basal loops increased. Alternatively the sharp decrease observed in defect yield from pure to very slightly impure metals may occur in h.c.p metals, but was not elucidated here since impurity levels in titanium with its strong affinity for oxygen are very high (see chapter four for impurity levels).

6.6. Defect Yield and Efficiency Calculations.

As outlined in section 4.7 the defect yield and cascade collapse efficiency values are very useful parameters for categorising the precise quantity of damage caused by each individual irradiation, and to gain accurate figures for these values it is obviously important to have as precise an estimate as possible for the exact number of ions implanted into a sample. As has already been mentioned, the calibration of the ion implanter used in this study can only estimate the received ion dose to an accuracy of 10%, and since disordered zone production in ordered alloys has been shown to be unsatisfactory in this energy range all doses are to within 10%.

6.6.1 Sub-Cascade Formation?

It is important to determine whether subcascade formation is occurring to illustrate whether loop formation is the result of a discrete cascade, for this has important implications on defect yield calculations. In order to ease identification of sub-cascade formation in titanium a series of low dose irradiations were performed. Since dosimetry becomes extremely unreliable on the Lintott ion implanter for doses below $\sim 10^{11}$ ions/cm², the exact implanted dose cannot be reliably quoted, but the equipment was set to nominally implant 5×10^{10} ions/cm² for these low dose experiments. The resulting defect yields and loop sizes were given in table 5.7 and an

example of the loop densities observed in these low dose irradiations is shown in fig 6.2. If subcascades were occurring we would expect to find pairs of loops in close proximity, so it is evident from the wide spacing of the observed dislocation loops no subcascade formation is occurring even at the highest energies and masses utilised in this study. Interestingly, there is no notable variation in loop size for each irradiation condition studied at this low dose in comparison with the 5×10^{11} ions/cm² results. This implies that even at the higher dose, visible collapsed vacancy loops form as a result of discrete heavy-ion induced cascades, and overlap of two cascades does not occur since this would result in a small population of much larger loops being observed due to the higher number of point defects present in the original cascade. It is interesting to note that although the defect yields are unreliable at this very low dose, the trends of the defect yields with increasing mass and energy encouragingly mirror the behaviour of these parameters for the higher dose investigations.

Further evidence for the lack of subcascade formation comes from the loop size distributions obtained. If some subcascade formation was occurring then a twin peak population would be expected since an incident ion producing two loops will produce smaller loops than an ion which only results in the formation of one loop. No evidence for this effect could be found in any of the loop size distributions obtained (see fig 5.8).

6.6.ii Corrections to Measured Parameters.

Perfect loops are glissile and may glide out of the foil due to mirror image forces, thus affecting the resultant measured loop population and yields. This behaviour may be confirmed crudely by estimating the number of perfect loops lost to the foil surface in each irradiation considered. This was achieved by considering the quantity of each of the three $\mathbf{b} = 1/3\langle 11\bar{2}0 \rangle$ loops present in each analysis. Assuming that collapse to each of the three types of Burgers vector is equally probable, we can then interpolate the discrepancy in numbers between the three types due to loop loss. This loop loss will obviously be more severe in certain directions due to the "off axis"

nature of the foil normal to reduce channelling effects. Equating three times the number of the largest population of the $1/3\langle 1120 \rangle$ types observed to the total population of perfect loops originally present we can obtain a reasonable estimate for the perfect loop loss and an adjusted defect yield (the yield which would be seen in the bulk of the material where surface effects do not come into play), and the initial perfect to faulted Burgers vector population may be quoted. The results of these calculations are shown in table 6.3.

In the S_3 orientation we can expect to lose two thirds of the perfect prism loop population to the foil surface since their Burgers vector will have a considerable component towards the foil surface, and it is therefore necessary to adjust the observed defect yields to allow for this phenomenon. The defect yields for the S_3 orientation irradiations, adjusted assuming that only one of the three types of perfect prism plane loops are observed in the electron microscope have been calculated and are presented in table 6.4.

6.6.iii. Defect Yield Trends.

Once a consistent estimate has been made for the received dose the defect yields can be calculated, and the results of these calculations have been detailed in table 5.3. The most striking effect observed is the transformation from a very low probability of cascade collapse to form visible loops for the case of single ion irradiations (d.y ~ 0.05) to a far higher probability for the case of molecular ion irradiations of similar ion dose and energy (d.y > 0.4). This significant rise in the probability of loop formation can be most easily ascribed to the large associated increase in energy density and vacancy concentration per atom in the cascade.

It is interesting to note that self-ion irradiations result in no visible damage and although single-ion tungsten irradiations produce cascades of equivalent energy density to the molecular antimony irradiations the observed defect yields are far lower. This effect was also seen but to a lesser extent in molybdenum (English and Jenkins, 1987), and thus the implication is that molecular and single ion irradiations are not directly comparable due to the dissociation of the molecular ions on impact with the surface. The first atom of the molecule generates a cascade and

thus the subsequent atoms are incident on atoms already in motion. M.D should provide some interesting insights on the precise effect of this phenomena and investigations are at present underway at Harwell into this behaviour (Foreman,1990).

For the case of S_3 irradiations the adjusted defect yield is in all but one case lower than the adjusted yields extrapolated from the S_1 data. However, once errors (see chapter 5) are taken into consideration the defect yields for the two orientations are broadly consistent. It is worth noting that only three of the six prism diffraction vectors $20\bar{2}0$ and $11\bar{2}0$ are achievable in the S_3 orientation, and it is therefore feasible that some prism plane loops are overlooked in an S_3 analysis. The criterion used in this study for counting observed contrast as a dislocation loop was for it to be present on at least two micrographs. Hence poor focussing and/or weak contrast could lead to some loops being missed. An alternative explanation for the lower defect yields observed in the S_3 orientation could be that double basal loops are forming preferentially in this orientation and since these loops are perfect they are lost to the surface by glide prior to observation in the electron microscope.

Otherwise the yield behaves in a conventionally accepted fashion, increasing with increasing ion energy and ion mass. No tailing off of this increase is observed, unlike the case for ruthenium (see next chapter), and the S_1 and S_3 data are in rough agreement once surface effects have been taken into account. The yields lie within the range 0-1 and no T.E.M evidence exists to suggest sub-cascade formation is occurring.

6.6.iv Loop Size and Cascade Efficiency.

The cascade collapse efficiency (ϵ) is a measure of the proportion of vacancies which survive the cascade process and are subsequently visible in the observed dislocation loops. As such this factor is primarily governed by the amount of recombination which occurs and also the rate at which the thermal spike cools, since this will determine the time scale over which vacancies are mobile and will

therefore determine the distance over which they can migrate to form dislocation loops before being frozen into the foil, either individually or as sub-microscopic agglomerates and thus overlooked in a T.E.M analysis. In titanium the efficiency increases with increasing ion mass and decreasing ion energy. The reason for this behaviour is related to the vacancy concentration and energy density of the cascades produced (figs 5.16 and 5.17). It is clear that the more diffuse are the vacancies in the cascade, then the more vacancies will recombine with interstitials and the lower will be the probability of collapse to form a dislocation loop. Here we note that as the loop size observed in S_1 titanium is virtually constant, ϵ decreases due to the larger number of point defects created in the higher energy irradiations. The reason for the constancy in observed loop size in the S_1 orientation is not immediately apparent, but the accuracy of the loop sizing is corroborated by the evidence from the S_3 data, where the average loop size is lower but rises with loop depth (i.e with increasing energy and molecular number) until it reaches a value almost equal to the sizes observed for the S_1 orientation. This behaviour can be explained by the loss of larger loops near to the surface due to the inherently larger image forces acting on them. This effect points against the systematic loss of large loops in the S_1 orientation suggested earlier.

By plotting the ϵ values against vacancy concentration and energy density it is possible to extrapolate the minimum values of vacancy concentration and energy density necessary to produce visible vacancy loops in titanium. This is shown in figs 6.3 and 6.4 respectively. From these graphs we note that the minimum energy density required to produce a visible dislocation loop is approximately 0.25 eV per atom and the minimum vacancy concentration required is approximately 0.03 vacancies per atom. This goes a long way to explaining the absence of vacancy loops in self-ion irradiated titanium since these conditions will be satisfied only for irradiations of < 18 keV. At 18 keV, N.R.T predicts 116 Frenkel pairs will initially be produced in the cascade, and thus assuming an efficiency of around 0.3 then the average loop size would be around 16 Å which is close to the resolution limit of the

JEM 200 B microscope. Furthermore it is likely that at this threshold the efficiency will be much less than 0.3 and will not rise rapidly enough with falling ion energy to compensate for the inherent reduction of point defect production. An efficiency of less than 0.12 at 18 keV would result in loop sizes of less than 10 Å and thus these loops could not be observed by conventional electron microscopy. It is also highly unlikely that vacancies of such small sizes will form into loops during the thermal spike lifetime.

Returning now to the surprising observation that for molecular ion irradiations of titanium loop size is almost invariant with irradiation condition, it is obvious from the graphs of cascade efficiency versus energy density and vacancy concentration that far fewer point defects are surviving the cascade process to eventually coalesce as part of the visible loops with increasing ion mass. One reason for this could be the dissociation of the constituent parts of the molecular ions on impact with the surface, the resulting cascades occurring in close proximity to each other. This may lead to enhanced point defect recombination since as noted earlier each cascade will consist of a vacancy rich core surrounded by a mantle of interstitials, and as these will lie next to each other it is feasible that one vacancy rich region may overlap with the part of the interstitial mantle produced close by. Obviously this effect will be largest for Sb_3^+ irradiations and indeed we note a marked increase in the energy density required to produce equivalent cascade efficiencies on progression from Sb^+ to Sb_3^+ ions. An estimate for the extra overlap occurring can be made as follows.

Assuming that the incident ions are equally spaced from each other then the fraction of overlap, x , which will result in increased recombination (see fig 6.5) can be calculated from the observed reduction in ϵ . For Sb_2^+ ions a reduction of $x/2$ will occur and for Sb_3^+ ions a reduction of $2x/3$ will occur. Thus from the graph of ϵ versus energy density we find $x = 0.3$. It is interesting to note that this value remains virtually constant for the range of energy densities considered. This

suggests that the degree of molecular ion dissociation on impact is material dependent since English and Jenkins (1987) irradiated molybdenum with molecular antimony ions and found the efficiency actually increased from 50 keV Sb^+ up to 150 keV Sb_3^+ ions, thus indicating that larger loops are produced in this material. This may also explain the absence of surface craters in titanium (which were observed in high energy molecular irradiations of molybdenum by English and Jenkins 1987) since the required vacancy concentration near to the surface may not be achieved. It should be noted that this is a very crude model since the subsequent atoms of a molecular irradiation are incident on atoms already in motion and thus the real situation is complex. Thermal spike lifetime cannot explain this maximum loop size since the spike lifetime will be longer for the Sb_3^+ irradiations.

The lack of subcascade formation, the apparent existence of a maximum loop size and the absence of any very deep loops as observed in molecular ion irradiated gold all point to the possibility that r.c.s and channelling distances may be shorter in the h.c.p system. Obviously interstitials must be capable of travelling far enough to prevent spontaneous recombination, but a limiting effect on the size of the loop and thus also the cascade seems to be at play, and also there is a definite barrier to the formation of subcascades, again suggesting a limit to the distance secondaries can travel.

The defect retention efficiency (D.R.E) calculated by multiplying the yield and efficiency values is a good guide concerning the quantity of point defects remaining in the foil following irradiation. This parameter will be considered in detail in the following chapter for the range of h.c.p metals. For the case of titanium the D.R.E is seen to increase for increasing ion mass and decreasing ion energy, and this is consistent with the behaviour observed for the high mass (W) irradiations performed by Phythian on ruthenium.

6.6.v Yield and Efficiency In Commercial Titanium.

For the commercial titanium the materials analysis reveals that ~ ten impurity atoms will be present in the disordered zone, and this increase in impurity content is

seen to manifest itself by a significant rise in defect yield, an increase in loop size and a decrease in perfect loop population for all irradiation conditions investigated. This behaviour may be explained by the calculated decrease in the S.F.E, (see section 6.4) which is thought to increase the probability of loop formation. The additional impurity elements may also act as preferred nucleation points, thus enhancing loop formation. The increase in loop population is linked to the decrease in S.F.E, since for a lower S.F.E the critical loop size for unfauling will rise and so fewer large loops will be lost to the surface. This explains the decrease in perfect loop population since fewer loops will attain the critical size necessary for unfauling to occur.

6.7 Segregation.

Griffiths *et al* (1982) irradiated high purity (0.035 at.% Fe) polycrystalline titanium with 1 MeV protons at ~ 750 K to a dose of 1 d.p.a and found vacancy loops on the [1011] planes which were analysed using an S.T.E.M to be rich in iron (0.2 at.%) compared to the background matrix count. S.T.E.M work was therefore undertaken on the heavy-ion irradiated titanium discs examined in this study. However, even for the most energetic conditions employed no evidence of any increase in iron concentration around the loop could be found, suggesting that the segregation of iron occurring in Griffiths' work is due to the high d.p.a of the irradiations used, and the purity of the material irradiated.

Ion	Energy	50 keV	100 keV	150 keV
Sb⁺ % faulted		0	68%	73%
% perfect		0	32%	27%
Sb₂⁺ % faulted		72%	71%	71%
% perfect		28%	29%	29%
Sb₃⁺ % faulted		71%	70%	69%
% perfect		29%	30%	31%

Table 6.1: The adjusted and normalised loop populations for S₁ iodide titanium, allowing for perfect prism loop loss to the foil surface.

Loop size (Å)	Pure edge (%)	Non-edge (%)
20-25	49	51
25-30	53	47
30-35	73	27
35-40	45	55
40-45	68	32
45-50	49	51
50-55	63	37
55-60	51	49
60-65	72	38
65+	63	37
Overall	60	40

Table 6.2 : Loop size versus pure and non-edge type loops observed in the case of iodide S_1 titanium irradiated with 150 keV Sb_3^+ ions. The populations have in all cases been normalised.

Ion Energy		50 keV	100 keV	150 keV
Sb ⁺	D.Y	0	0.06 ± .02	0.04 ± .02
	ε	0	0.25	0.09
	D.R.E	0	0.02	0.004
Sb ₂ ⁺	D.Y	0.42 ± .04	0.43 ± .04	0.51 ± .05
	ε	0.38	0.21	0.12
	D.R.E	0.16	0.09	0.06
Sb ₃ ⁺	D.Y	0.66 ± .05	0.69 ± .05	0.84 ± .06
	ε	0.38	0.19	0.13
	D.R.E	0.25	0.13	0.11

Table 6.3: Adjusted defect yield and efficiency values for S₁ iodide Ti.

Ion Energy		50 keV	100 keV	150 keV
Sb ⁺	D.Y	0	irradiation	0.05 ± .02
	ε	0	not	0.08
	D.R.E	0	performed	0.004
Sb ₂ ⁺	D.Y	irradiation	0.47 ± .05	0.50 ± .05
	ε	not	0.15	0.12
	D.R.E	performed	0.07	0.06
Sb ₃ ⁺	D.Y	0.55 ± .06	0.56 ± .06	0.64 ± .07
	ε	0.23	0.17	0.14
	D.R.E	0.13	0.10	0.09

Table 6.4: Adjusted defect yield and efficiency values for S₃ iodide titanium.

Loop Diameter vs Probability of Finding an Unfaulted Loop.

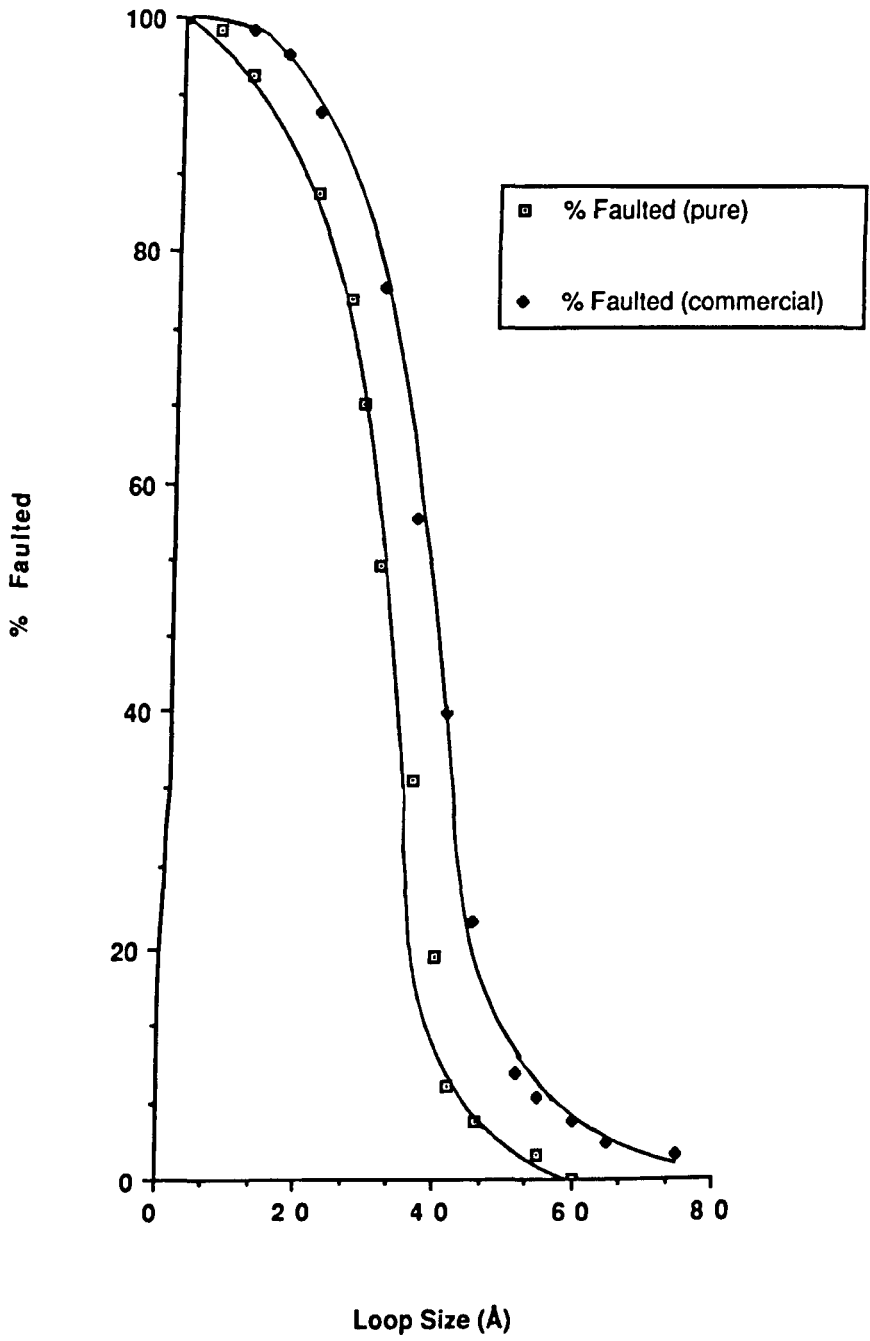
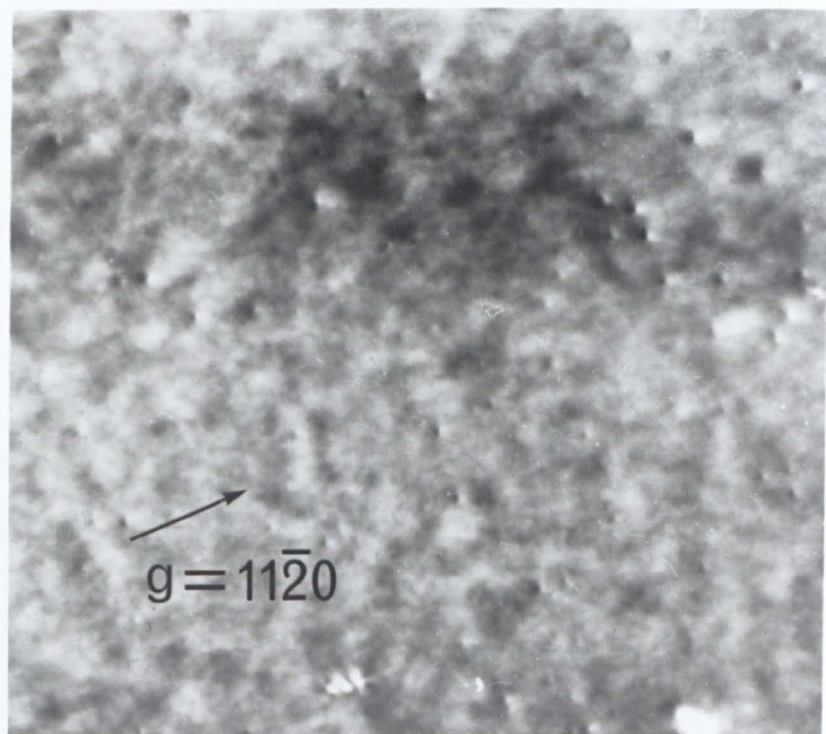


Fig 6.1: Pure and commercial TI unfaulting probabilities.

The following page shows figure 6.2, a typical micrograph of a low dose irradiation into α -titanium.

The irradiation condition shown is 150 keV Sb_3^+ ions



1000 Å

Vacancy concentration vs efficiency for titanium

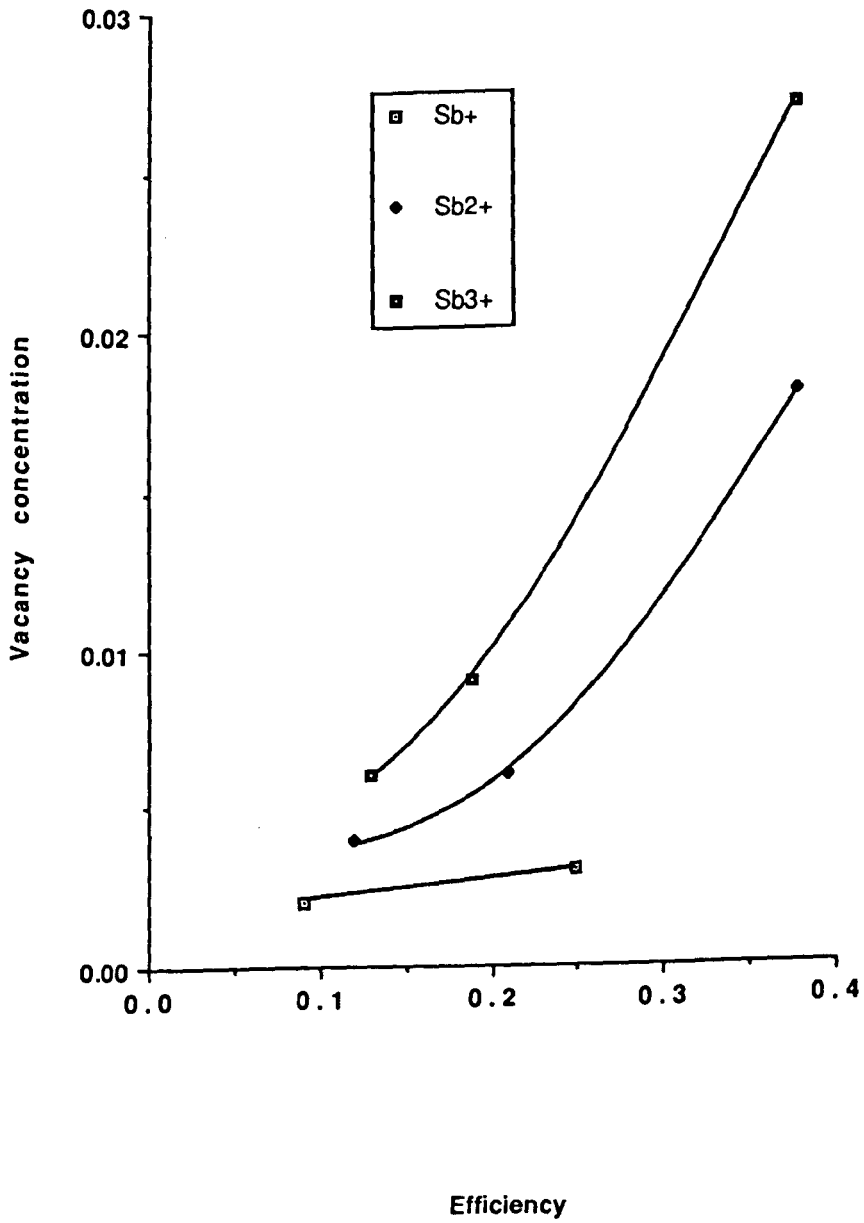


Fig 6.3: Efficiency vs vacancy concentration.

Energy Density vs Efficiency for titanium

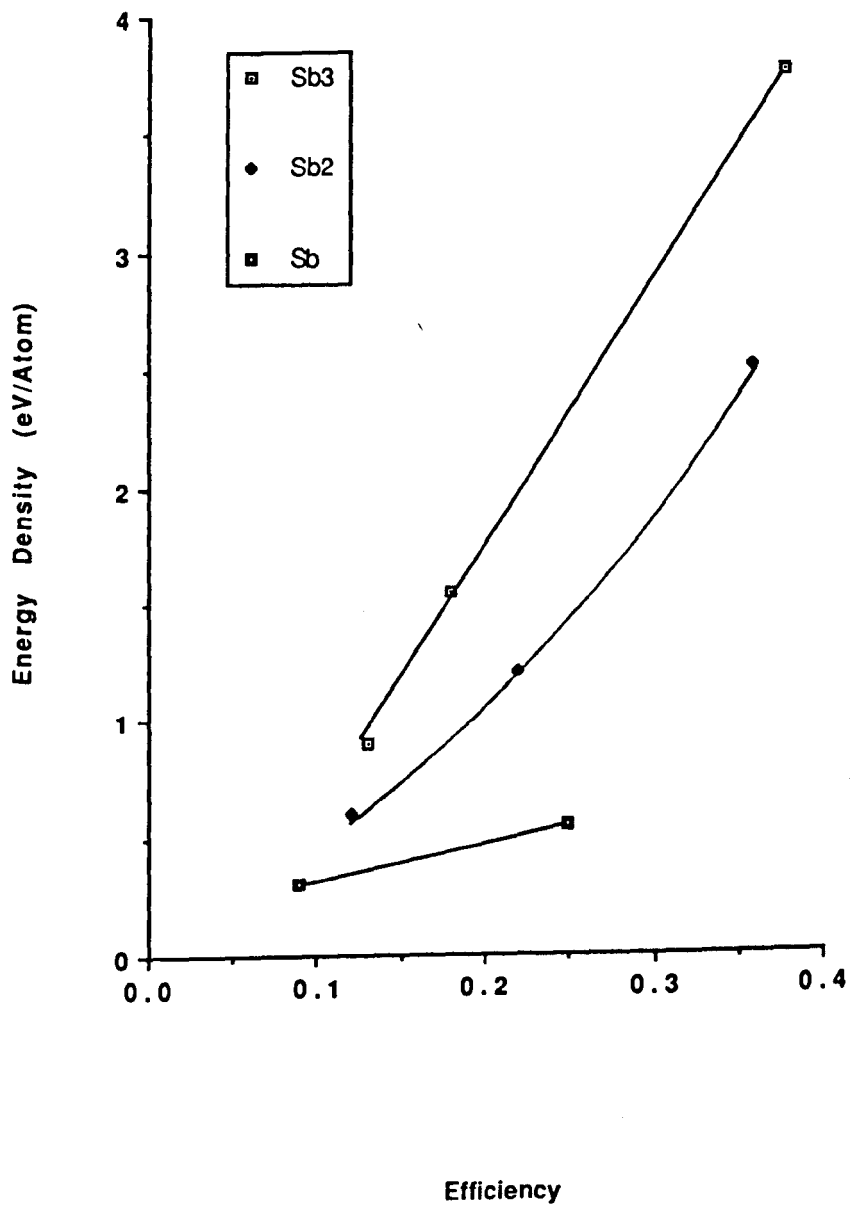
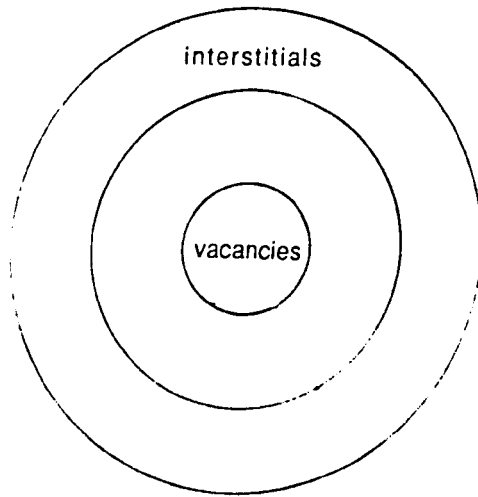
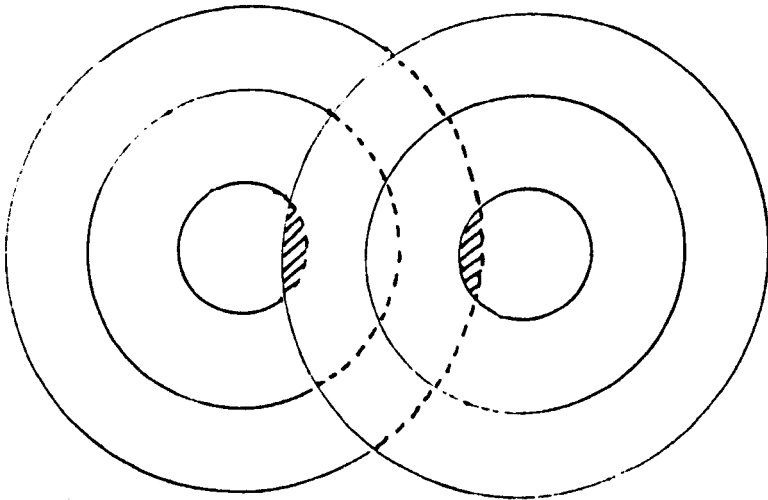


Fig 6.4: Efficiency vs energy density.



The accepted picture of a single-ion implant consisting of a vacancy rich core surrounded by a mantle of interstitials.

Two superimposed cascades showing the possibility of overlap of a vacancy rich region with an interstitial rich region leading to enhanced recombination.



 = Area of overlap.

Fig 6.5: Molecular Ion recombination effects.

Chapter 7 Cascade Collapse in h.c.p Metals.

7.1 Introduction.

In this chapter the trends elucidated for the range of h.c.p metals examined will be discussed in terms of the irradiation parameters previously outlined. An attempt to explain the variations observed in terms of the properties of the various materials will be made. Each metal irradiated will be considered in turn, and then a comparison of the behaviour of these h.c.p materials to the well-documented characteristics noted to govern irradiation behaviour in the cubic materials will be made. Finally, the results will be discussed in terms of their implications for applications of these materials in a reactor environment.

On examining thinned foils using T.E.M it is obviously important to determine whether any damage is occurring due to the high energy electrons (up to 300 keV) used for inspection. Bradley (1987) has calculated the threshold energies required for an electron to produce a Frenkel pair in any pure solid element at room temperature, for the metals examined in this study these are:

Metal	Threshold electron energy (keV)
magnesium	79
cobalt	355
titanium	386
ruthenium	726
rhenium	775

Thus only magnesium would be expected to exhibit gun-damage due to the electron-beam, and this could present problems for the low temperature irradiations proposed later in this chapter. At 100 keV, however, T.E.M should not produce much damage at low temperatures in magnesium since, firstly, these energies are threshold values and most electrons will not therefore create a Frenkel pair, and also Urban *et al* (1982) calculated that E_D increases with decreasing temperature.

Bond *et al* (1987) found that “sub-threshold” damage occurs in aluminium charged with hydrogen but not in pure aluminium. They explain this behaviour as the result of electrons colliding firstly with hydrogen in the aluminium foil, followed by the excited hydrogen atom colliding with a lattice atom. In this way, due to a reduction in the mass difference it is possible to transfer a greater amount of energy from the electrons to the lattice atoms. In the present study this effect would be most appreciable in titanium where a large impurity concentration is present. From equation 2.2 it can be calculated that a 200 keV electron (as used throughout the study) can transfer up to 4.5 eV in a direct collision with a titanium atom, and this is appreciably smaller than the energy required to displace the atom (about 25 eV in this case, see White 1983), whereas by colliding firstly with a hydrogen atom up to 215 eV may be transferred, then on a subsequent collision between this hydrogen atom and a titanium atom (from equation 2.1), up to 17.5 eV may be transferred. So we may conclude that electron damage will not be observed in this study.

7.2 Materials Parameters, Their Relation to the Defect Density.

The loop geometries observed throughout this study are consistent with the idea of faulted prism loops forming and consequently unfauling if energetically favourable. However, as can be seen from the graphs (Figs 7.1 -7.6), of the various materials parameters, melting point, atomic mass, *c/a* ratio, stacking fault energy, vacancy concentration and energy density plotted against the observed defect yields, efficiencies and defect retention efficiencies, no one parameter is dominant in determining the defect structures observed. This is discussed in greater detail below:

7.2.1 Melting Point.

Figure 7.1 shows the effects of melting point. Rhenium has a very high melting point (3450 K) and this would seem the only factor capable of explaining the lower yields observed in rhenium than in ruthenium ($T_m = 2520$ K). This seems reasonable since a high melting point will effectively lead to a rapid quenching of the thermal spike reducing the time-scale over which vacancy migration is possible and

hence reducing the probability of loop formation. It is interesting to note that titanium, which has a similar melting point to cobalt has a much lower yield, thus implying that melting point does not solely govern the behaviour. From these trends a low melting point can be seen to lead to large loops (cobalt) and hence more vacancy migration to the core, thus also resulting in a higher defect yield.

7.2.ii Atomic Mass.

From Fig 7.2 it can be seen that apart from rhenium the yield increases with atomic mass. The anomalous behaviour may be due to its very high melting point leading to a severely curtailed thermal spike lifetime. Examining the properties of the various h.c.p metals (table 3.1) the easiest way to confirm this trend would be to irradiate hafnium with antimony ions since this material has a similar mass(178.5) to rhenium (186.2) and a similar melting point (2423K) to that of ruthenium (2520 K), thus we would expect to see a defect yield higher than any observed so far for the same irradiation conditions. The prism S.F.E of hafnium is also much lower than that of rhenium (185 mJ/m^2 compared with 600 mJ/m^2) and this may also affect the yield (see later).

7.2.iii c/a ratio.

Fig 7.3 shows that the c/a ratio has no appreciable effect on the quantity of damage observed. This is fairly unsurprising since the maximum variation in the c/a ratio is from 1.587 (titanium) to 1.623 (cobalt) which is only a 2% change. A trend emerges however if the titanium results are discounted due to the very low vacancy concentrations produced in this metal resulting in a very low defect yield. We then find an increase in yield for a decrease in the c/a ratio. However, for the high c/a ratio metals zinc and cadmium, this trend could well reverse, i.e a low in defect yield occurring for ideal stacking. Unfortunately these metals are difficult to investigate due to their low melting point and consequently low annealing temperature. Again hafnium would be interesting due to its low c/a ratio, however a high yield is also predicted due to its high mass and moderate melting point. Oh and

Johnson (1989) using an embedded-atom method many-body model maintained all other parameters and investigated the relationship between stacking fault energy and c/a ratio. They found that as the c/a decreased from ideal the stacking fault energy increased (the range investigated was from 1.58 to 1.63 due to the limitations of the model used), thus the expected trend would be for this increased stacking fault energy to reduce the defect yields and hence the yield should decrease with decreasing stacking fault energy, almost the exact opposite effect has been seen in this study. For clarity the experimental values for the prism stacking fault energies noted in this study are plotted against c/a ratio (Fig 7.7) and it is clear that no trend has emerged. To conclude then, the evidence from the titanium results implies that the c/a ratio does not play a major role in determining the quantity of damage observed.

7.2.iv Stacking Fault Energy.

From Fig 7.4 it can be seen that the S.F.E (here Legrand's 1984 values are used) is not the dominant force in determining the quantity of damage observed, since ruthenium (520 mJ/m^2) has a much higher stacking fault energy than cobalt (230 mJ/m^2) and yet exhibits a much higher defect yield. Indeed the yield actually increases (except for rhenium) with increasing S.F.E which is exactly opposite to the expected behaviour. The S.F.E may however, make a small contribution since the defect yield is lower in rhenium than in ruthenium corresponding to a decrease in yield for an increase in S.F.E. Here a study of yttrium may be informative since this metal has the lowest prism stacking fault (60 mJ/m^2). It seems reasonable that the S.F.E is not the dominant force since the cascade process is catastrophic in nature destroying the local symmetry of the crystal and thus the S.F.E will only effect the evolution of the cascade once a considerable amount of cooling of the thermal spike has occurred.

7.2.v Energy Density and Vacancy Concentration.

The lowest defect yields are noted for the single antimony ion irradiated titanium foils, and these foils are unique in that an increase in defect yield is seen for a

decrease in irradiation energy (from 150 to 100 keV). This trend does not continue for 50 keV Sb⁺ irradiations presumably because there are simply not enough vacancies produced for collapse to form a visible loop to occur. Some threshold vacancy concentration for the onset of cascade collapse therefore seems likely, and reference to fig 5.17 indeed shows that the vacancy concentration is very low. It is also revealing that on transition to molecular-ion irradiations there is a huge jump in the observed defect yield. Thus it may be speculated that a vacancy concentration somewhere between the ranges achieved for titanium (where collapse does not readily occur) and cobalt, the next lowest vacancy concentration where collapse readily occurs, must be achieved before cascade collapse to form visible loops may occur. A further pointer to this behaviour is that contrary to all the other observations in titanium, for the case of 150 keV Sb⁺ ions implanted in titanium the loop size is seen to be significantly smaller, thus suggesting cascade collapse is very difficult at these low vacancy concentrations. A minimum value of not less than 0.025 and not more than 0.075 vacancies per atom therefore seems reasonable and careful tailoring of the irradiation parameters should elucidate the exact value quite easily. Calder (1989) calculates using a Monte-Carlo program that for 50 Å discs placed randomly to an areal density of $5 \times 10^{11}/\text{cm}^2$ the amount of overlap occurring will be approximately 3%. Thus the observed loop population may correspond to the few cases where overlap of two cascades has occurred, thus indicating that a vacancy concentration of around 0.05 vacancies per atom is required for loop formation to occur. Similarly it has been speculated that some threshold energy density may exist below which cascade collapse to form visible loops will not occur. Following the same logic as before we can conclude from fig 5.18 that this threshold value will be approximately 0.6 eV/atom. Once this threshold value has been passed we might expect to see the yield and efficiency values rise with vacancy concentration and quantity of defects produced. However inspection of Figs 7.5 and 7.6 show that this is not the case. For completeness the vacancy

concentrations and energy densities produced by the ions in each of the metals studied can be found in Figs 7.8 and 7.9 respectively.

7.2.vi Electron-Phonon Coupling.

Electron-Phonon coupling has been proposed as a mechanism by which heat can be removed from the cascade regions by means of the free electrons, thus leading to drastically reduced thermal spike lifetimes. It is difficult to determine the exact contribution of this phenomenon due to the absence of any information on the Fermi velocity in the metals of interest (needed to calculate the Debye temperatures of the metals). To date evidence for the role of electron-phonon coupling (see chapter two) stems from the metals copper and nickel. These two metals have extremely disparate critical temperatures for coupling to occur. This wide variety does not exist in the h.c.p metals examined in this study.

Agnew (1989) has developed a model for estimating the electron-phonon interaction in a metal. He calculates ξ , from $\xi = T_d/\gamma$ (7.1)

where γ is the electronic heat capacity constant.

This model relies on the proximity of elements in the periodic table for accuracy since varying cascade sizes will effect the accuracy of the estimates, however the following ratios have been determined:

$$\xi_{Cu}/\xi_{Ni} = 30$$

$$\xi_{Ag}/\xi_{Pd} = 70$$

$$\xi_{Re}/\xi_{Co} = 4.4$$

$$\xi_{Ru}/\xi_{Re} = 0.8$$

$$\xi_{Ru}/\xi_{Ti} = 6$$

Thus we see that huge differences occur for copper and nickel. In the h.c.p case however, only small differences exist, the largest of which is between titanium and rhenium where coupling should be greatest in titanium. This trend may not hold true though since the smaller cascade size in rhenium due to its higher mass will favour a

stronger interaction as will the inherently higher initial energy density (again due to the difference in mass of the two elements). Agnew notes that a difference of ~ 30 is required for a difference in irradiation behaviour to emerge. Fig 7.10 shows the variations of the yields and efficiencies with the ratio of their electron-phonon coupling values. Broadly speaking the quenching effects should be greatest in cobalt/titanium and least in rhenium/ruthenium, which is the observed behaviour for the defect yield, but not the efficiency or defect retention efficiency. Due to the small differences in the values obtained for ξ and the large mass differences involved, however it is difficult to draw definite conclusions from the results of this study.

7.2.vii Unification of the Material Parameters.

It would obviously be desirable to predict the behaviour of a metal under irradiations purely from its material parameters. Since four materials have been studied, four parameters may be considered. The four variables used are mass, melting point, vacancy concentration and S.F.E since these seem to be the parameters which have the largest effect. By assuming that temperature and S.F.E have an inverse effect since an increase in these parameters is expected to lead to a decrease in yield, a set of four simultaneous linear equations against defect yield values here for the case of 100 keV irradiations may be solved:

	Mass	S.F.E	Vac conc	T_m	
Ruthenium:	101	$W + 3.87 \times 10^{-4} X$	$+ 0.0145 Y$	$+ 1.92 \times 10^{-3} Z$	$= 0.32$
Cobalt:	59	$W + 5.67 \times 10^{-4} X$	$+ 0.0125 Y$	$+ 4.35 \times 10^{-3} Z$	$= 0.13$
Rhenium:	186	$W + 2.81 \times 10^{-4} X$	$+ 0.023 Y$	$+ 1.67 \times 10^{-3} Z$	$= 0.21$
Titanium:	49	$W + 5.13 \times 10^{-4} X$	$+ 0.003 Y$	$+ 9.0 \times 10^{-3} Z$	$= 0.05$

giving:

$$d.y = -730/T_m + 37/\gamma + 0.0016 M + 27 C_v$$

This equation fails since the melting point does not correspond to theory. Any "Grand

unifying theory" involving these four parameters must clearly be a complex power law which is beyond the scope of the present study to predict, and also other factors such as electron-phonon coupling may be important, hence more metals need to be considered.

7.3 Individual Characteristics of the Metals Studied.

Apart from the possible differences already discussed for each metal there are also other factors unique to each of the metals studied and these are considered in the following section:

7.3.1 Magnesium.

In all cases the defect yield for magnesium was found to be zero at room temperature. Delaplace *et al* (1968) investigated the recovery of neutron irradiated magnesium and found that single vacancy migration became possible at around 240 K, thus at room temperature any vacancy loops which form will anneal by vacancy emission. T.E.M observation of damage at room temperature is therefore unlikely. Vacancies are not mobile at room temperature in any of the other metals investigated, and thus the magnesium results are not comparable with the others. It was, however, useful to perform this experiment to confirm the behaviour of this material at room temperature.

It is unfortunate that room temperature irradiations of magnesium are not comparable to the rest of the data since it is the only h.c.p metal with a Pilling-Bedworth ratio less than one (0.81 from MgO data). Legrand (1984) did not calculate the exact stacking fault energy values but quotes R (the ratio of the basal to the prism stacking fault energy) as 0.25, i.e the basal stacking fault is one quarter that in the prism plane. Thus the S_3 and S_1 orientations should yield some interesting results on the effect of the stacking fault energy and the role of stress due to surface oxides. It would thus be useful to perform some low temperature in-situ irradiation and T.E.M observations at liquid nitrogen temperatures where vacancies would no longer be mobile. Interestingly, Delaplace *et al*, noted from resistivity

measurements, that at low temperatures where irradiation resulted in the production of point defects, the quantity did not noticeably vary with impurity content. This tallies with the earlier observations in titanium, where, contrary to the case for cubic materials, the defect yield did not fall for an increase in impurity content.

7.3.ii Cobalt.

Cobalt undergoes a martensitic phase transformation at 420°C to the f.c.c structure, making growth of large single crystals using the standard zone refining technique extremely difficult. Unannealed specimens contain a very high concentration of dislocations and heat treatment is of little use here since the transformation temperature is very much lower than the melting point.

The stacking fault energy of the basal plane is very much lower than that of the prism plane and we would therefore expect to see a large amount of c-component damage. T.E.M investigation of the material, however, failed to reveal any c-component damage at all, and in the S_3 orientation very little damage of any type could be found. Hitzenberger *et al* (1985) observed a high line defect density in unirradiated S_3 orientation single crystal cobalt. They identified these defects as virtually exclusively c-component in nature, as observed in the present study, and may explain the puzzling absence of dislocation loops in S_3 cobalt. It is possible that some loops created in the S_3 orientation are lost before an analysis can be performed, due to the presence of a line dislocation acting as a vacancy sink.

Cobalt is of interest in the present work since it was anticipated that the basal S.F.E would be far lower than the prism S.F.E. Legrand's (1984) theoretical estimates are: $\gamma_{\text{basal}} = 45 \text{ mJ/m}^2$ $\gamma_{\text{prism}} = 230 \text{ mJ/m}^2$.

Hitzenberger *et al* (1985) calculated the basal S.F.E from weak-beam T.E.M observation of the splitting width of Shockley partials to be $\gamma_{\text{basal}} = 27 \pm 4 \text{ mJ/m}^2$.

In this study the prism plane S.F.E has been calculated using the same method as outlined in chapter 6 for the case of titanium, giving good agreement with Legrand's

estimate, as γ_{prism} was found to be between 280 - 370 mJ/m².

It is interesting to note that to date no study of h.c.p single crystals has revealed basal loops in the S_1 orientation. This suggests that some mechanism exists by which either prism plane loops preferentially nucleate or all basal loops are lost to sinks such as the surface.

Previously the absence of c-loops could have been explained by the relatively poor contrast obtainable from these defects in the S_1 orientation, but the evidence from this study seems to point to the total absence of this loop type in cobalt since prism loops were unexpected and rather a large basal loop population was anticipated, which would therefore have revealed itself even in the S_1 orientation. This returns us to the idea that anisotropy of the cascade due to the ion-beam direction has a role to play and it would be informative to irradiate S_3 titanium or ruthenium (where both basal and prism loops are observed) at a large (45° or greater) angle to the foil surface. If c-loops were then not found it would be possible to attribute their formation to the shape of the original cascade.

Loop loss seems unlikely since although the basal plane loops would have their Burgers vectors pointing directly at the foil surface, only faulted loops would be expected and climb is not possible during the lifetime of these experiments. "Doubling up" of the loops to form perfect loops and consequent glide out of the foil seems intuitively unlikely, but in-situ irradiations could be performed to check for this behaviour assuming that loop loss can be observed, i.e it is not virtually instantaneous.

Maury *et al* (1970) found from resistivity measurements that the damage (defect production) rate for oriented single crystal cobalt irradiated with 450 keV electrons at 7K was highest in the S_1 orientation and lowest in the S_3 orientation. They went on to determine the threshold displacement energies and found $E_D = 22$ eV in the $\langle 0001 \rangle$ direction rising to 25 eV in the $\langle 11\bar{2}0 \rangle$ direction. In a contemporary paper Howe (1970) found conflicting evidence suggesting that $E_D = 23$ eV in the

$\langle 11\bar{2}0 \rangle$ direction rising to 33 eV in the $\langle 0001 \rangle$ direction. This finding has not since been substantiated and the large difference between the two values in Howes work suggests some experimental error, and indeed Maury proposed that the $\langle 0001 \rangle$ threshold may well in fact corresponded to a true threshold of 22 eV along the $[10\bar{1}4]$. It is worth noting that in titanium, White (1984) found $E_D = 23.8$ eV in the $\langle 0001 \rangle$ direction rising to 25.4 eV in the $\langle 11\bar{2}0 \rangle$, which is very similar to Maury's findings.

Cobalt is a strongly anisotropic ferromagnetic material, featuring a large magnetic component in the S_3 orientation, and this could have some effect on the observed defect structure. One effect is that micrograph quality is significantly poorer in the S_3 orientation due to the large stigmatic effect of the magnetic field. However the resolution of the microscope in this orientation can be shown to be satisfactory by imaging of line dislocations with widths as small as 20 Å. It can therefore be said with confidence that the absence of loops in the S_3 orientation is not attributable to poor image quality. The magnetic domains present in the material might be thought to have some effect. However, Korner and Karnthaler (1983), in studying glide dislocations in cobalt, reversed the objective lens current and hence also the polarity of the domains, but the defect structures remained constant. Similarly the splitting width of a dislocation does not change on passing through a domain wall, and thus it would appear that the magnetic properties of the material have no effect on the defect structures observed.

7.3.III Ruthenium.

The behaviour of ruthenium under heavy ion irradiation has been well categorized by Phythian (1985), and Phythian *et al* (1987, 1990). The trends observed have been documented in chapter three. Estimates for the S.F.E of ruthenium are as follows:

$$\text{Legrand (1984)} \quad \therefore \gamma_{\text{basal}} = 520 \text{ mJ/m}^2 \qquad \gamma_{\text{prism}} = 438 \text{ mJ/m}^2$$

$$\text{Phythian } et \text{ al (1987)} : \gamma_{\text{basal}} = 510 \pm 150 \text{ mJ/m}^2 \quad \gamma_{\text{prism}} = 370 \pm 134 \text{ mJ/m}^2$$

Again good agreement between theory and experiment is noted. The metal has been studied here so that Phythians findings may be incorporated into the present study of h.c.p metals using antimony ion irradiations. One interesting point to arise from the present study was that sub-cascade formation was not observed. Phythian *et al* felt that by increasing the ion energy above 100 keV the incident ions might be energetic enough to escape the initial cascade region, thus producing sub-cascades. This effect would manifest itself by an increase in the yields observed. This has not been found here, implying that either sub-cascades are not produced in ruthenium, in contradiction with Phythian *et al*, or that the incident ion energy must be raised further than the range employed here.

7.4.iv Rhenium.

Rhenium is a very high density, high melting point high atomic mass metal, and thus of interest in elucidating the effects of these parameters on the final defect structures observed. Legrand 1984 calculated the stacking fault energy on the prism plane as 600 mJ/m^2 , which is the highest prism plane stacking fault of all the metals examined in this study. Annealing in a U.H.V furnace is critical for rhenium since at 150°C rhenium reacts with any oxygen present to form rhenium heptoxide (Re_2O_7), a volatile yellow solid which melts at 302°C , thus the foils can soon be reduced to powdery remains, as indeed occurred when some foils were initially heat-treated in a low vacuum muffle furnace.

The S.F.E for the prism plane in rhenium has been calculated using the method outlined in chapter 6. The value obtained was between $795 - 1120 \text{ mJ/m}^2$. This compares to Legrand's' value of 600 mJ/m^2 . It should be borne in mind that premature unfauling due to the proximity of the foil surface or other dislocations will result in an artificially high experimental value and thus the value calculated here may be too high.

7.4 Comparison to Cubic Metals.

In comparing the results of heavy-ion irradiations into h.c.p metals with the findings for metals with the cubic structure some basic similarities become apparent:

- 1.) The $d.y$ increases for increasing ion energy (except for very low vacancy concentrations).
- 2.) The $d.y$ increases for increasing ion mass (both for increasing single-ion mass and for transition from atomic to molecular ions).
- 3.) The ϵ decreases for increasing ion energy.
- 4.) The ϵ decreases for decreasing ion mass (again both for increasing atomic-ion mass and for transition from atomic to molecular ions)
- 5.) Unfaulting occurs most readily for large loops and for metals with high stacking fault energies.

The main differences noted are:

- 1.) The loop habit plane is not exclusively the close-packed plane in h.c.p metals.
- 2.) An increase in impurity content results in an increase in the $d.y$ for titanium. (Habtetsion 1989 noted an increase in the damage rate in electron irradiated cobalt with increasing impurity content, adding to earlier evidence of similar behaviour in magnesium and, in this study, titanium).

7.5 Summary.

In attempting to understand the role of each individual parameter it is obviously desirable to hold all the others constant. However factors such as the c/a ratio and S.F.E cannot be changed at will. The effect of variation in melting point could be cancelled by studying each metal at a different temperature. For instance an arbitrary value, say $0.2 T_m$, could be chosen and then each metal should behave equally as far as temperature effects are concerned. Varying incident ion energies and masses could be chosen to produce cascades of equal energy density or vacancy

concentration in different metals, but here the cascades would vary in size. It seems unlikely therefore that a definitive statement on the effects of each parameter can be made, but our understanding can still be improved.

To summarise for the h.c.p crystal structure: a minimum energy density and vacancy concentration is required to produce visible dislocation loops. Once this threshold has been surpassed the melting point and atomic mass of the target metal play a vital role in determining the extent of damage observed. The c/a ratio and S.F.E may also play a small role in determining the damage. The geometry of the damage observed is dependent on the orientation of the crystal and damage is not confined to the close-packed planes.

7.6 Implications for Reactor Construction Materials.

The most deleterious effect seen in h.c.p materials used where a neutron flux is present is the phenomenon known as growth. The mechanism by which this process occurs has been attributed to the presence of c component loops (see chapter three). From the results for titanium and ruthenium, where these c -component loops have been observed, the trend seems to be for the proportion of these loops to increase as R , (the ratio: prism/basal stacking fault energy) decreases. R is quoted as 2.64 for titanium, 2.27 for zirconium and 1.68 for ruthenium, thus growth should be less of a problem in titanium than that encountered in zirconium.

7.7 Cluster Fusion.

The claims by Fleischmann and Pons (1989) that fusion could be attained at room temperature, while being of dubious authenticity in themselves, served to stimulate Beuhler *et al* (1989) to consider the possibility of fusion occurring in this material due to the high transitory temperatures achieved during a cascade event, thus enabling the Lawson criterion for pressure, temperature and time to be met. The fusion reaction:



was achieved by bombarding deuterated titanium with large clusters of molecular heavy water (d_2O) at around 300 keV per cluster. By varying the energy and size of the clusters Beuhler *et al* managed to achieve a best figure of one fusion event per 10^{13} incident deuterons. Greenland (1989) showed that these results are consistent with the fusion cross-sections for deuterium at the elevated temperatures achieved during the cascade. He notes that this rate of reaction is 5×10^9 below break even for reaction (7.2). This could be improved by the addition of tritium to the heavy water giving the reaction:



For reaction (7.3) he calculates the fusion rate improves to 2×10^7 below break even. One way forward may be to apply the knowledge gained here for the temperature and time scale of cascades produced by heavy-ion bombardment of a material. The requirement is for a metal capable of holding large quantities of deuterium, whilst also exhibiting a large defect yield (implying a large thermal spike lifetime) and having a high cascade energy density, hence producing as hot a cascade as possible for as long as possible. The present work, therefore points to hafnium as an interesting material since it has an equal affinity for deuterium as titanium and has very favourable properties (low melting point, low S.F.E and high mass) as far as high cascade temperatures are concerned, hence creating ideal conditions for prolonged fusion to occur.

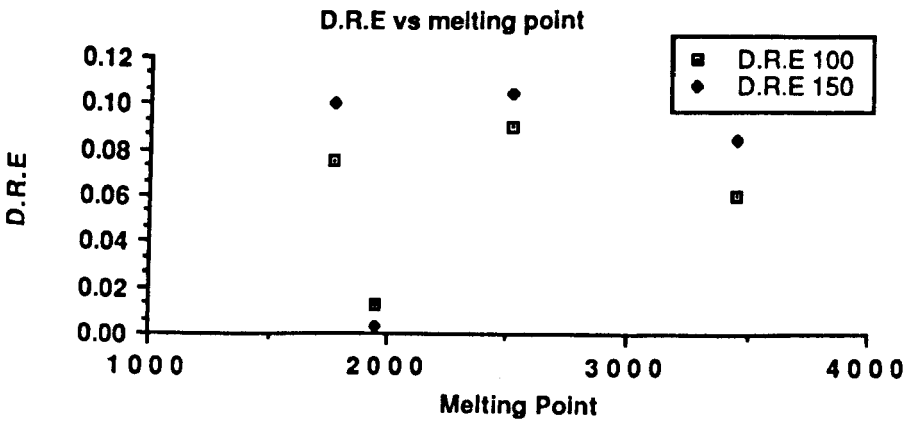
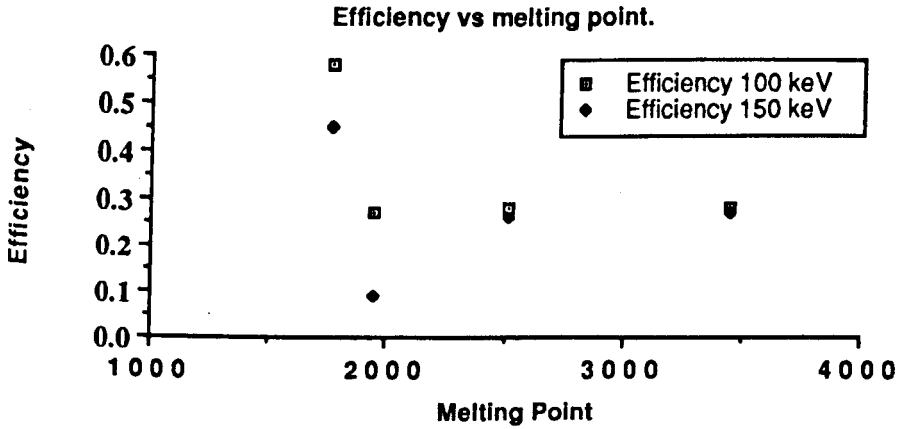
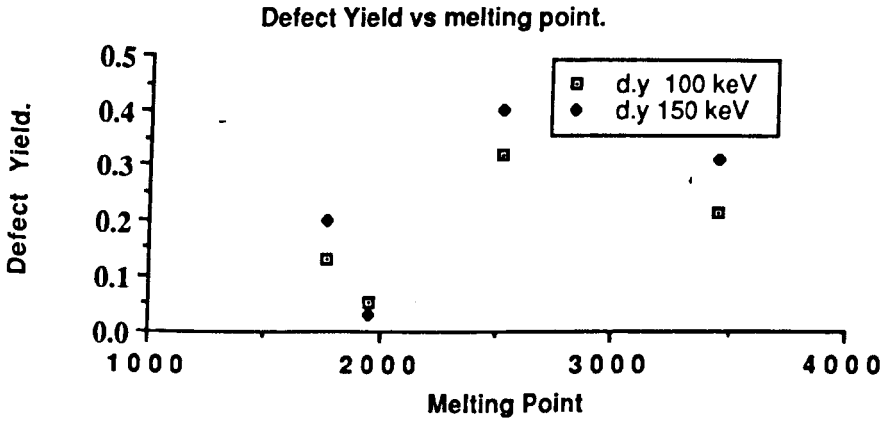


Fig 7.1: D.R.E, d.y, and ϵ vs melting point.

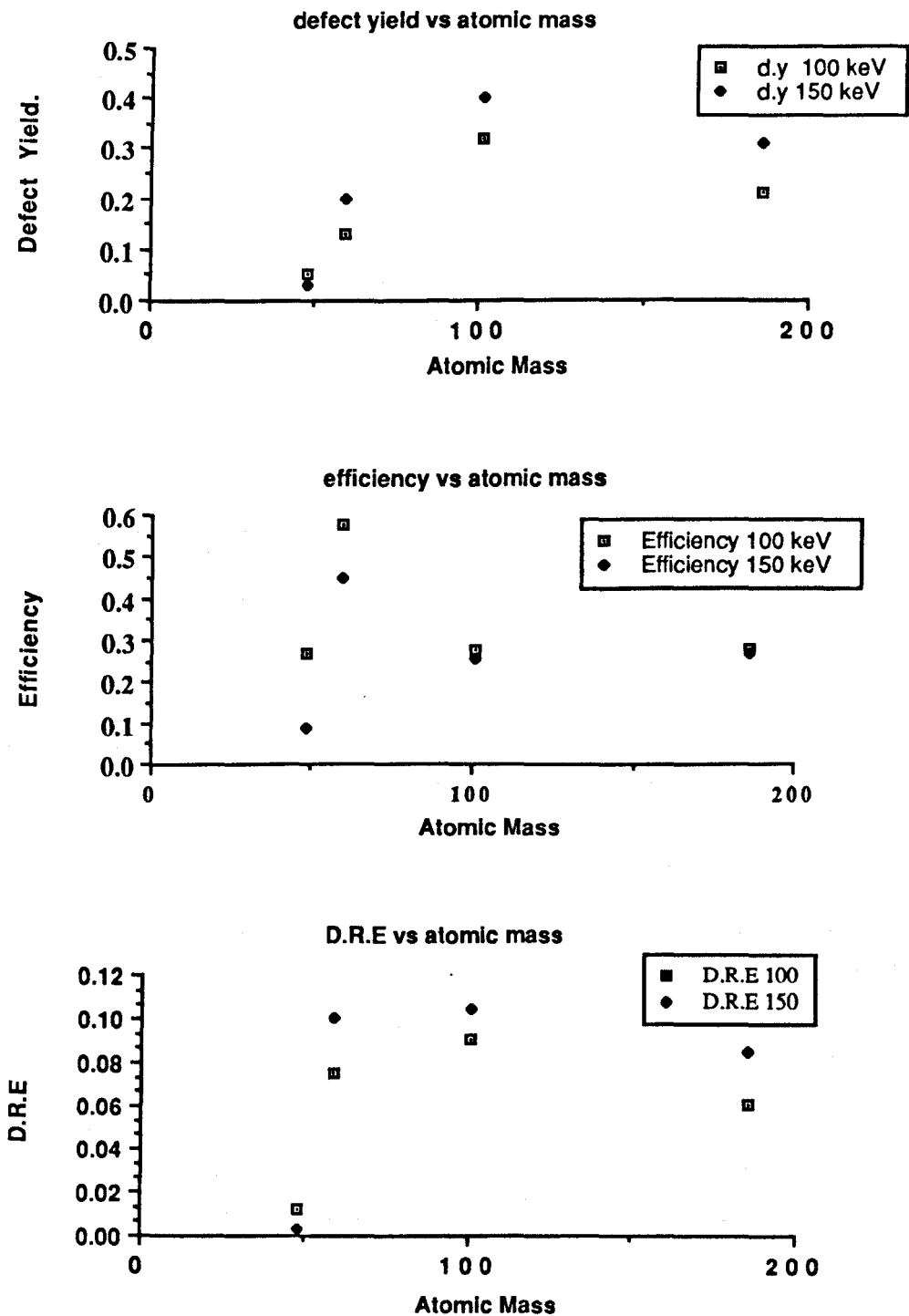
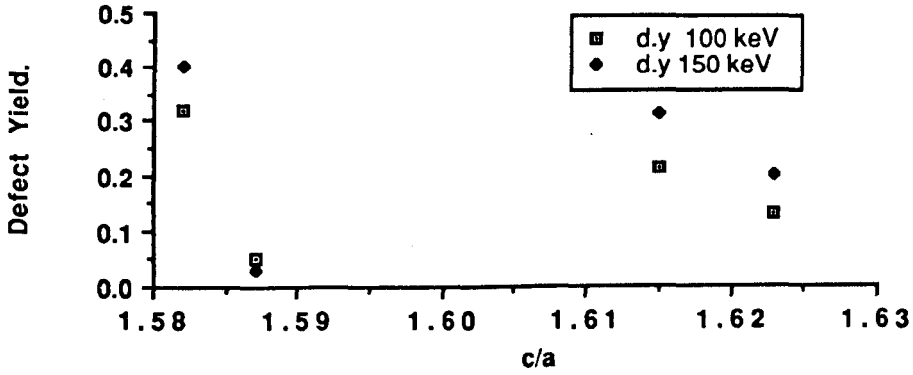
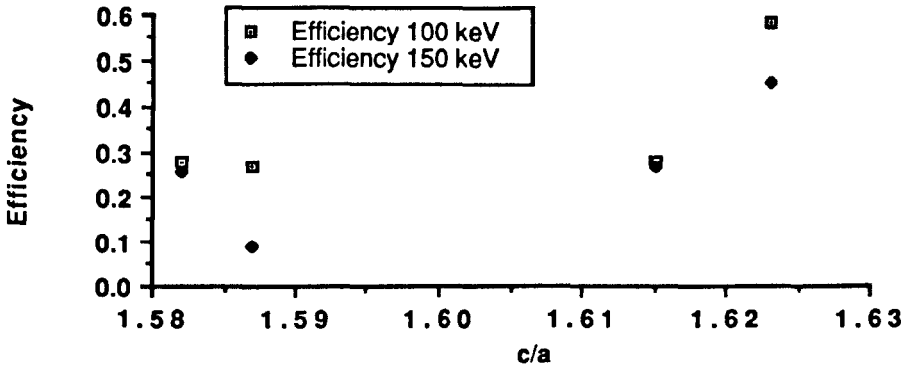


Fig 7.2: D.R.E, d.y, and ϵ vs atomic mass.

defect yield vs c/a ratio



Efficiency vs c/a ratio



D.R.E vs c/a ratio

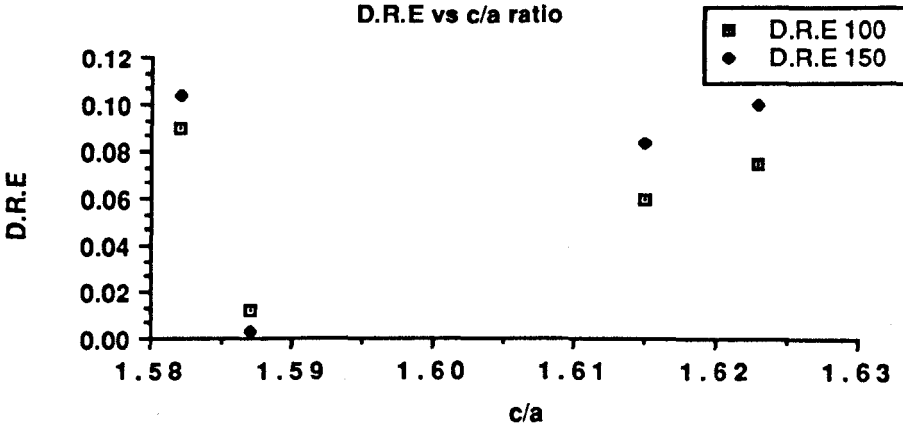
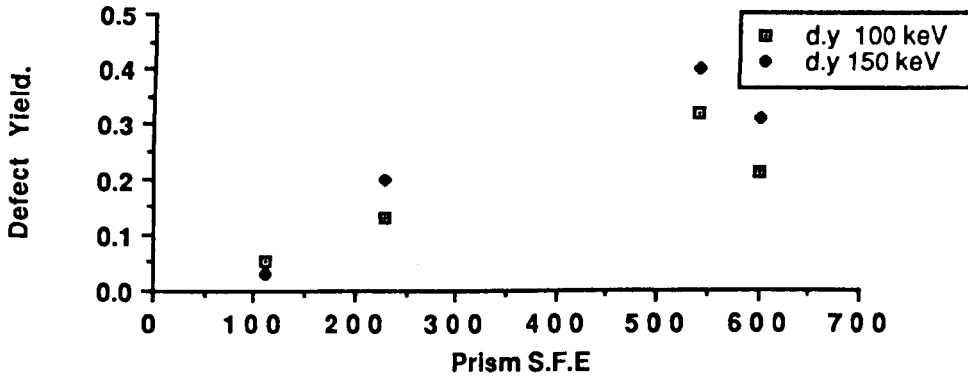
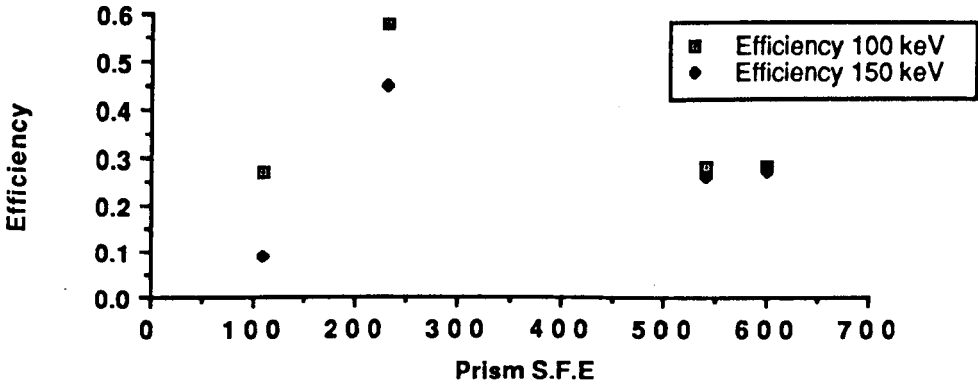


Fig 7.3: D.R.E, d.y, and ϵ vs c/a ratio.

Graph of defect yield vs S.F.E.



Graph of efficiency vs S.F.E



D.R.E vs S.F.E

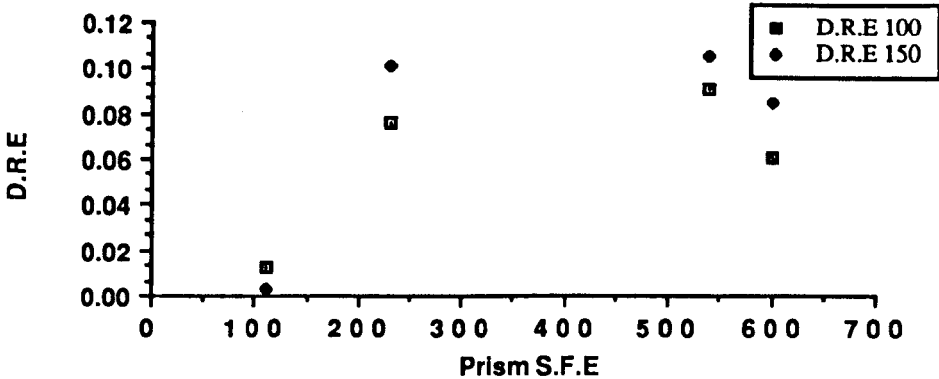


Fig 7.4: D.R.E, d.y, and ϵ vs stacking fault energy.

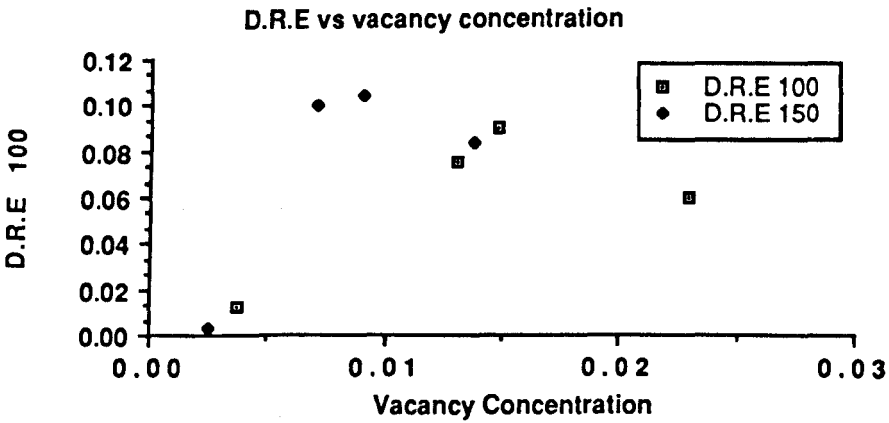
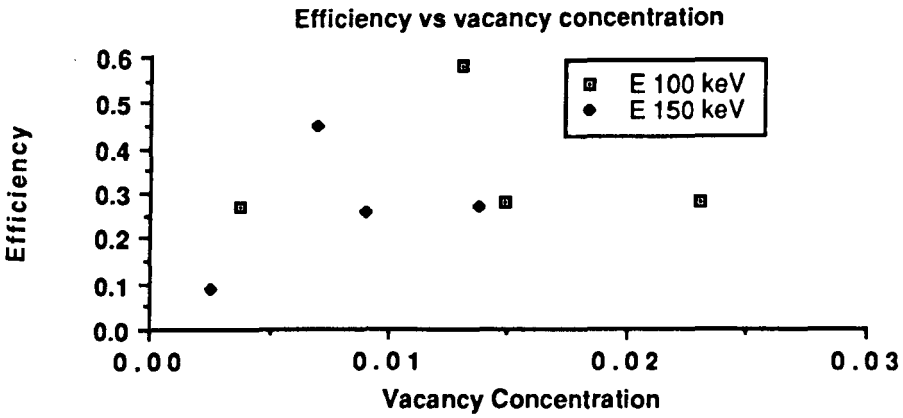
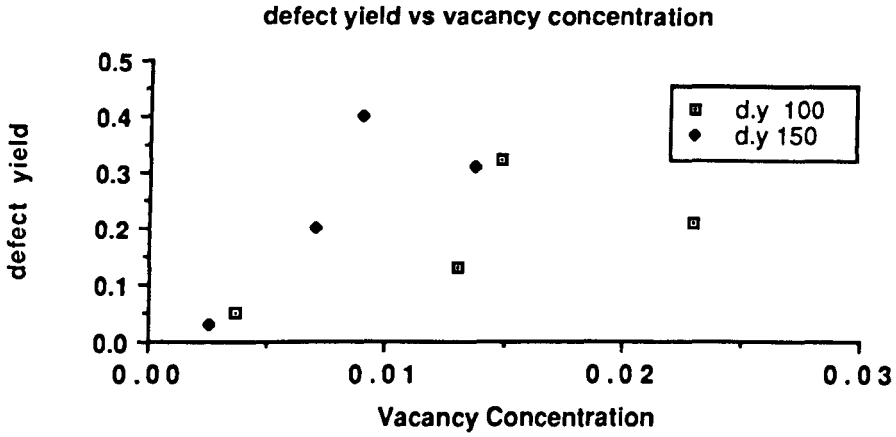


Fig 7.5: D.R.E, d.y, and ϵ vs vacancy concentration.

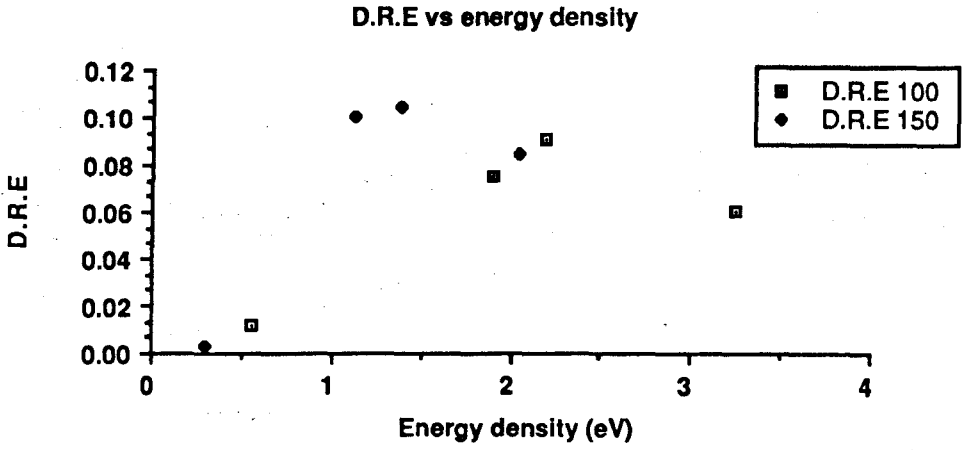
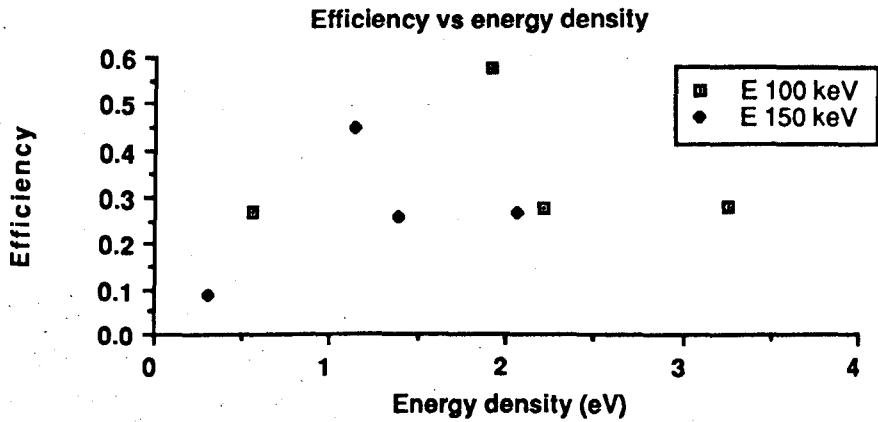
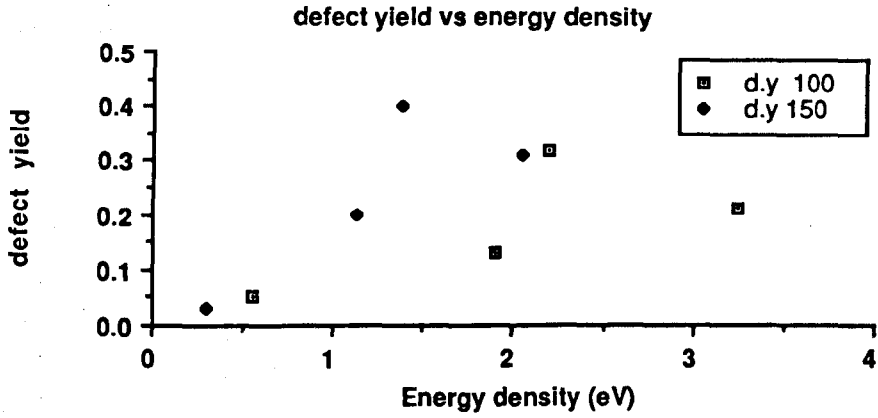


Fig 7.6: D.R.E, d.y, and ϵ vs energy density.

c/a ratio vs stacking fault energy

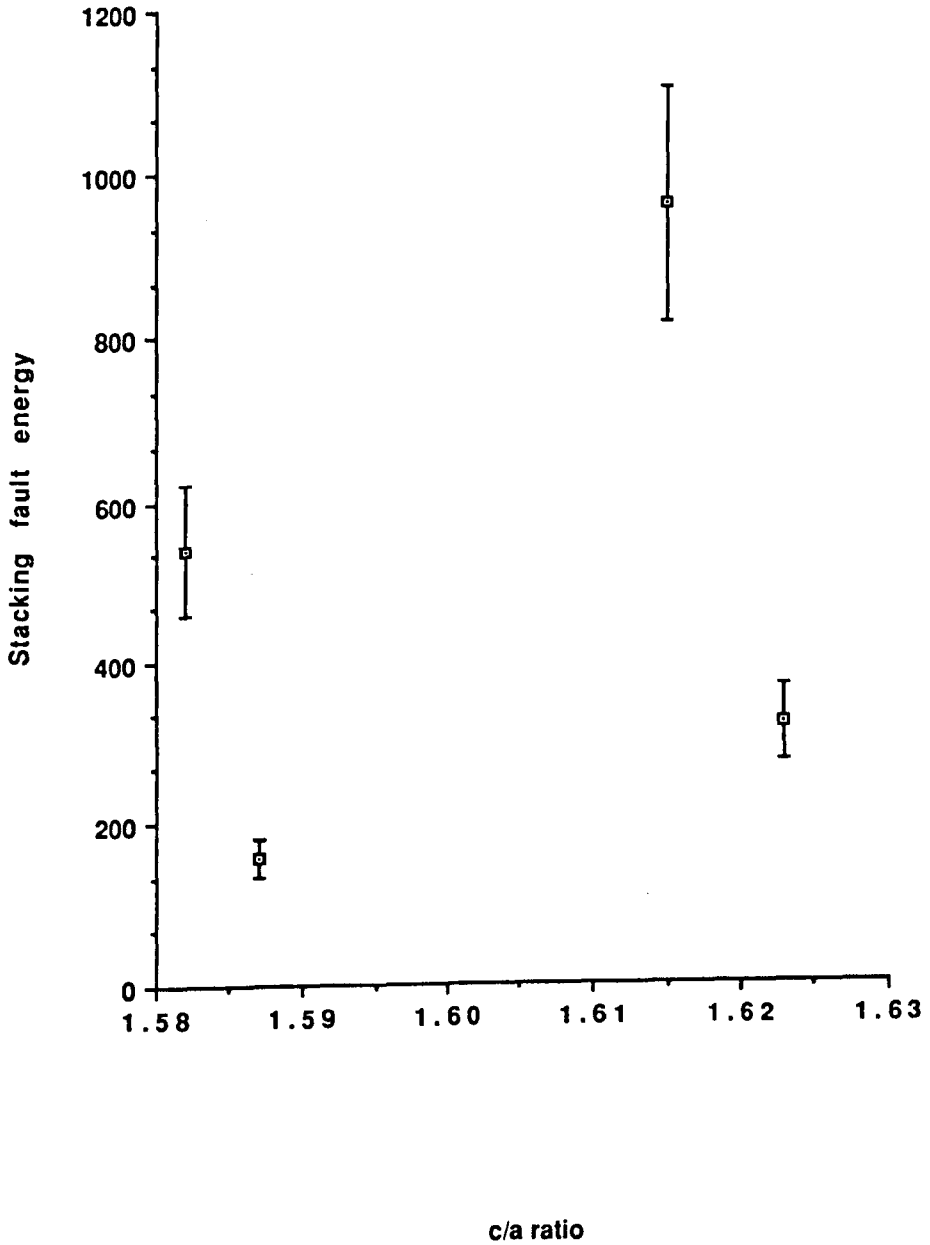


Fig 7.7: c/a ratio vs stacking fault energy.

Energy Density per Atom vs Ion Energy

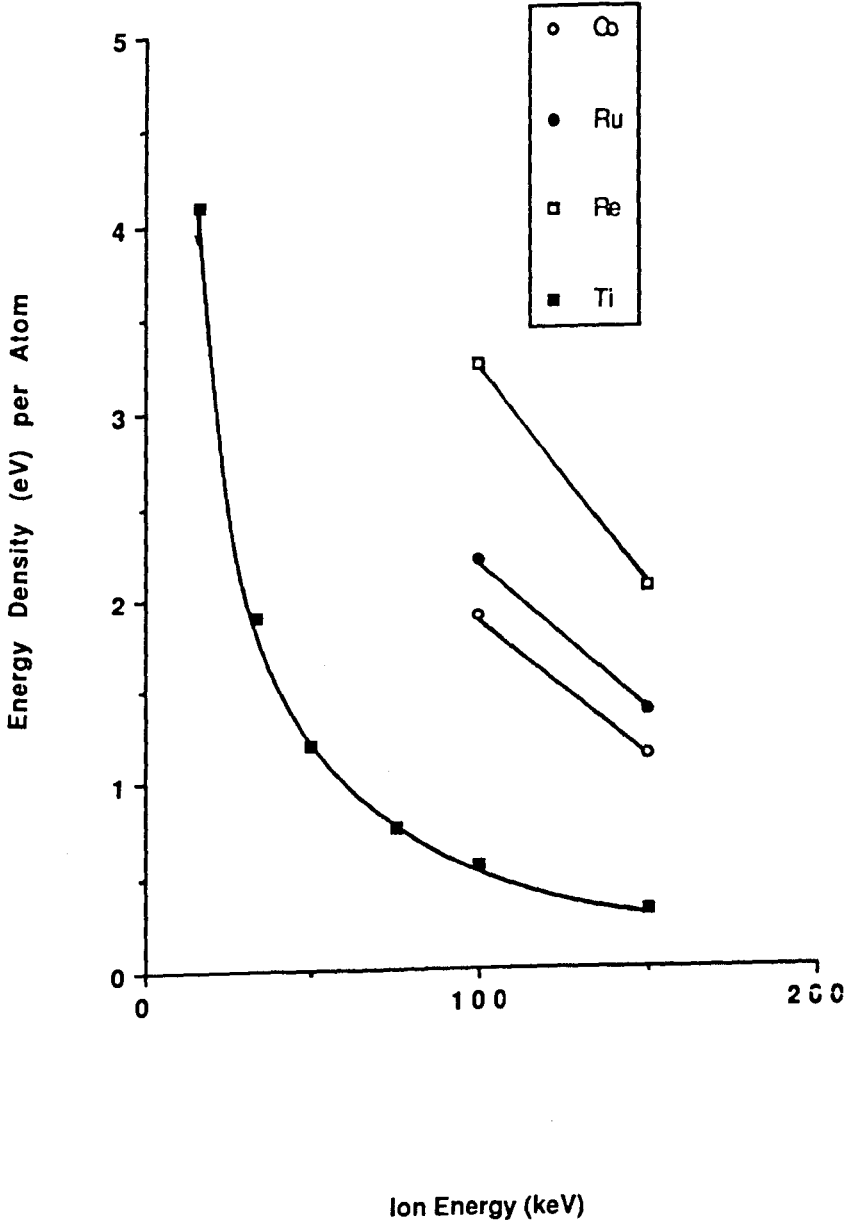


Fig 7.8: Energy density per atom vs ion energy.

Vacancy concentration vs ion energy

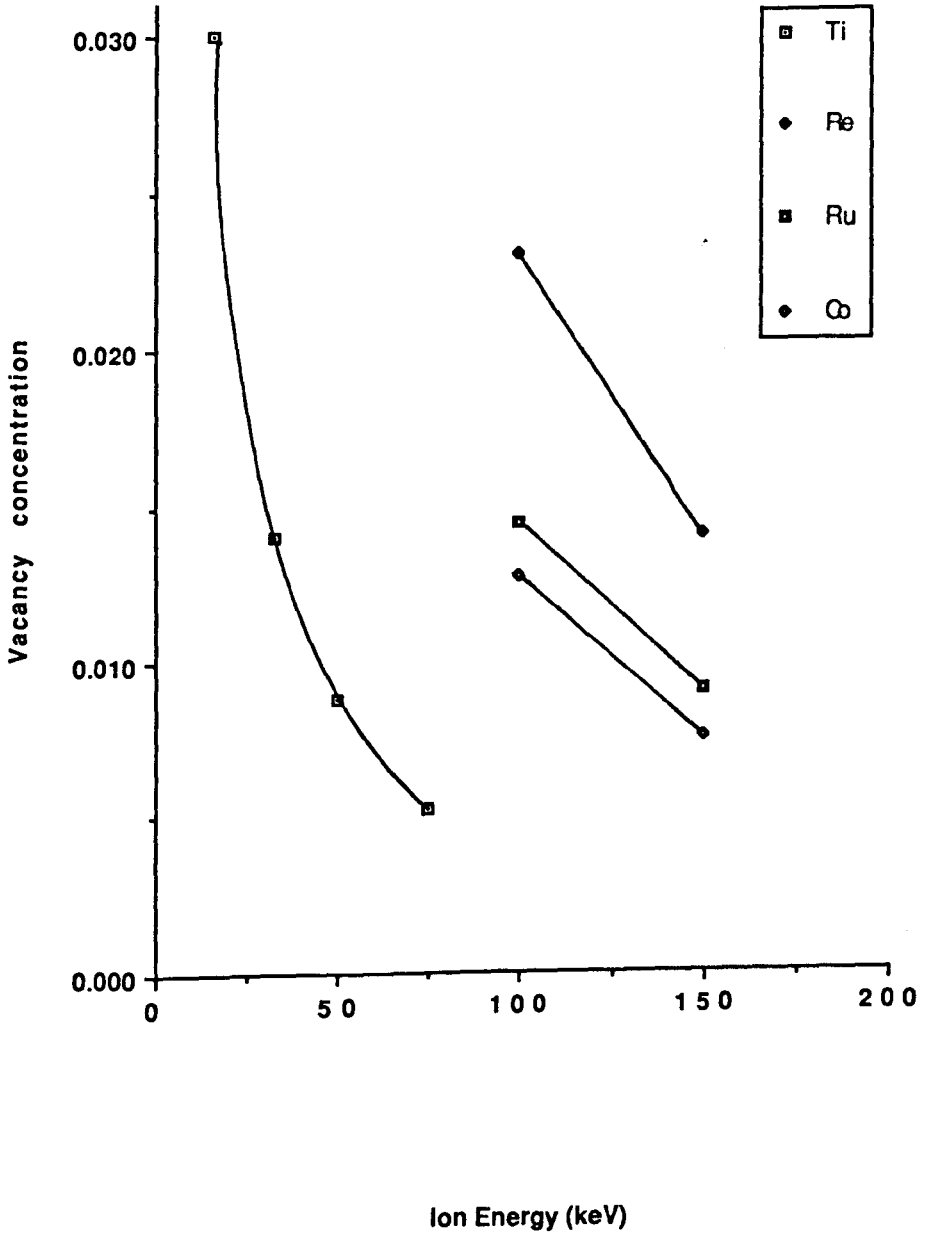


Fig 7.9: Vacancy concentration per atom vs ion energy.

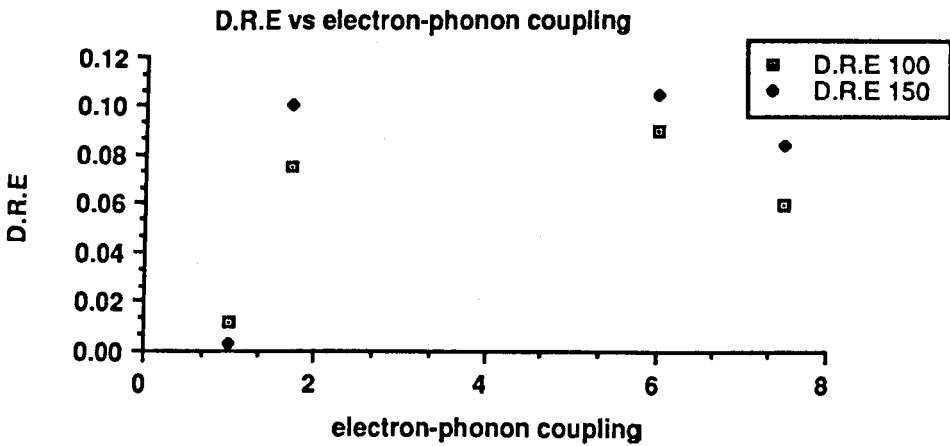
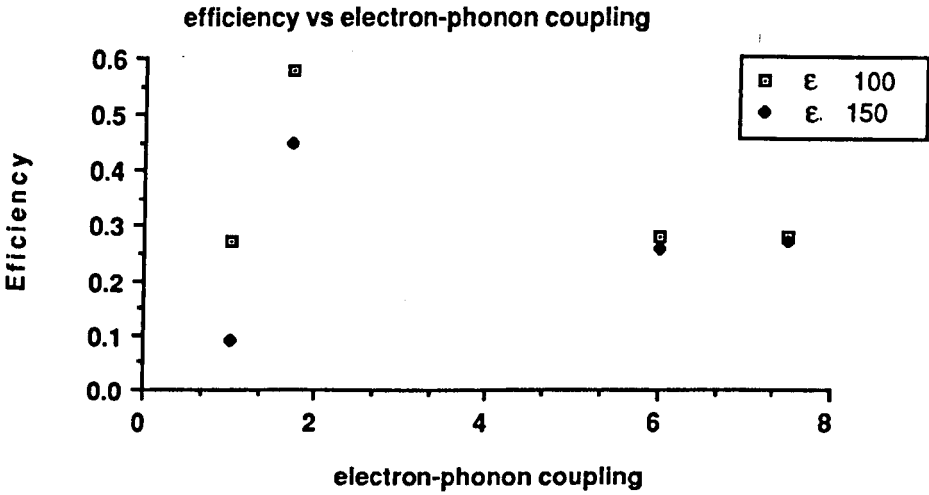
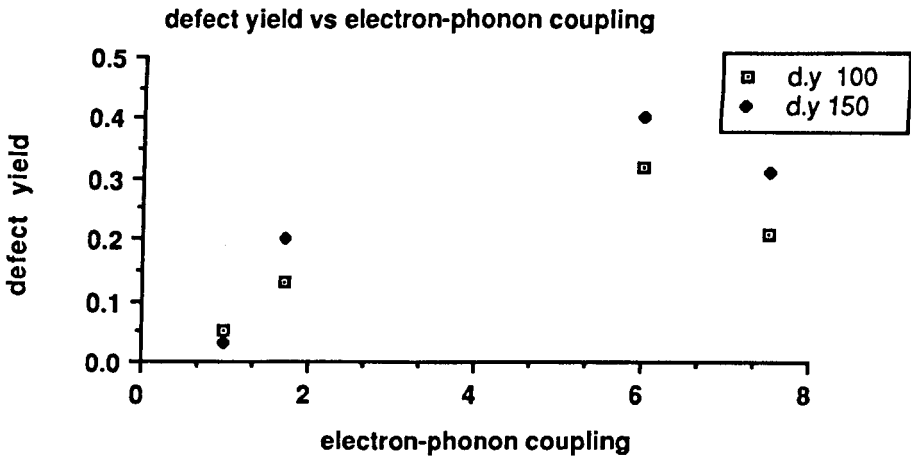


Fig 7.10: D.R.E, d.y, and ϵ vs electron-phonon coupling ratio,

Chapter 8 Summary and Suggestions for Further Work.

8.1 Summary.

The main points arising from the present study can be summarised as follows:

- 1.) Heavy-ion irradiation at a low dose produces vacancy dislocation loops in a range of h.c.p metals.
- 2.) The observed damage geometries are in good agreement with the accepted theory for all the metals examined.
- 3.) The pure edge population increases for molecular Sb_3^+ ions in titanium
- 4.) Loop depth increases for molecular Sb_3^+ ions in titanium
- 5.) The stacking fault energies for iodide and commercial titanium, cobalt and rhenium have been experimentally calculated to be:

$$\text{titanium : } \gamma_{\text{prism}} = 129 - 184 \text{ mJ/m}^2 \quad \gamma_{\text{basal}} = > 272 \text{ mJ/m}^2$$

$$\text{commercial titanium : } \gamma_{\text{prism}} = 119 - 141 \text{ mJ/m}^2$$

$$\text{cobalt : } \gamma_{\text{prism}} = 281 - 377 \text{ mJ/m}^2$$

$$\text{rhenium : } \gamma_{\text{prism}} = 795 - 1120 \text{ mJ/m}^2.$$

These values are all in good agreement with previously reported theoretical and experimental estimates.

- 6.) The d_y increases with increasing impurity content in titanium.
- 7.) Threshold values for the onset of visible loop formation in titanium are:
Vacancy concentration: > 0.05 vacancies per atom.
Energy density: > 0.6 eV per atom.
- 8.) Subcascade formation has not been observed in h.c.p metals for incident ion energies up to 150 keV
- 9.) Ordered alloys were not found to provide useful dosimetry information for incident ion energies as high as those used in this study.

10.) No one material parameter dominates in determining the quantity of damage observed.

8.2 Suggestions for Further Work.

The following experiments would be useful in further elucidating the trends observed due to heavy-ion irradiation of h.c.p metals.

- 1.) Extend the investigations into the range of materials by performing the antimony matrix molecular ion irradiations. This would enhance our understanding both of the materials behaviour and the effects of molecular ion irradiations.
- 2.) 45° irradiations of S_3 iodide titanium or ruthenium to determine the effects of irregular cascade shape on the loop habit plane.
- 3.) Low temperature irradiations of S_1 and S_3 magnesium to illuminate our understanding of the role of the surface oxide in determining the habit plane of the loops.
- 4.) Low temperature irradiations of zinc to evaluate the effect of a large variation in c/a ratio and to examine the transition from less than ideal to greater than ideal c/a ratio.
- 5.) Irradiation of hafnium foils to illustrate the importance of melting point and atomic mass on the final defect structure.
- 6.) Irradiation of yttrium foils to further investigate the role of stacking fault energy in determining the final defect structures.
- 7.) Irradiations in beryllium would be informative due to its very low mass. However problems in specimen preparation will be encountered due to the highly toxic nature of beryllium dust.
- 8.) A series of irradiations into different metals at $\sim 0.2 T_m$ to elucidate our understanding of the role played by temperature.
- 9.) Heavy water cluster ion bombardment of deuterated hafnium to investigate the possibility of fusion processes.

References

- Agnew, P. (1989)**
Harwell, Internal Memorandum.
- Averback, R.S. & Seidman, D.N. (1987)**
Mat.Sci.For., 18, p693
- Bacon, D.J. (1988)**
J.Nuc.Mat., 159, p176.
- Beeler, J.R. (1966)**
Phys.Rev. 150, p170.
- Beeler, J.R. (1974)**
J.Nuc.Mat., 53, p207.
- Bell, W.L. (1975)**
J.Nuc.Mat., 55, p14.
- Bell, W.L. & Adamson, R.B. (1978)**
General.Electric.report., NEDO-12708.
- Berghezan, A., Fourdeux, A. & Amelinckx, S. (1961)**
Acta.Met., 9, p464.
- Beuhler, R., Friedlander, G. & Friedman, L. (1989)**
Phys.Rev.Letts., 63, p1292.
- Biersack, J.P., & Haggmark, L.J. (1980)**
Nuc.Inst. & Meths., 174, p257
- Biersack, J.P., & Fink, D. (1975)**
Atomic collisions in solids, 2, p793. pub.Plenum.press.
- Black, T. (1984)**
Ph.D.Thesis., University of Oxford.
- Blake, R.G., Jostsons, A. & Kelly, P.M. (1974)**
Proc.8th.Int.Conf.Elect.Mic., p610.

- Bond, G.M., Robertson, I.M., Zeides, F.M. & Birnbaum, H.K. (1987)**
Phil.Mag., 55A, p669.
- Bradley, C.R. (1987)**
"Calculations of atomic sputtering and displacement crosssections in solid elements by electrons with energies from threshold to 1.5 MeV". pub, Argonne National Lab
- Brager, H.R., Garner, F.A. & Guthrie, G.L. (1977)**
J.Nuc.Mat., 66, p301.
- Brimhall, J.L., & Mastel, B. (1968)**
Phys.Stat.Sol., 27, K89
- Brimhall, J.L., Kulcinski, K.L. & Kissinger, H.E. (1971)**
Rad.Effs., 9, p273.
- Buckley, S.N. (1962)**
"Prop.Of.React.Mat. & Effs.Of.Rad.Dam", Pub. Butterworth, London.p413.
- Bullough, T.J., (1987)**
Ph.D.Thesis, University of Liverpool.
- Cairns, J.A., Marwick, A.D., Nelson, R.S., & Briggs, J.S. (1972)**
Rad.Effs., 12, p7.
- Calder, A.F. (1989)**
Unpublished work.
- Calder, A.F. (1989)**
Vacuum., 39, p1115.
- Carpenter, G.J.C. (1973)**
Rad.Effs., 19, p189.
- Carpenter, G.J.C., Murgatroyd, R.A., Rogerson. & Watters, J.F. (1981)**
J.Nuc.Mat., 101, p28.
- Causey, A.R., Fidleris, V. & Holt, R.A. (1986)**
J.Nuc.Mat., 139, p277.

- Chivers, D. (1989)**
Private communication.
- Delaplace, J., Hillairet, J., Nicoud, J.C., Schumacher, D. & Vogl, G. (1968)**
Phys.Stat.Sol., 30, p119.
- Diaz de la Rubia, T., Averbach, R.S., Hsieh, H. & Benedek, R (1989)**
J.Mater.Res., 4, p579.
- Diepers, H. & Diehl, J. (1966)**
Phys.Stat.Sol., 16, K109.
- Dollins, C.C. (1975)**
J.Nuc.Mat., 59, p61.
- Echer, C.J. (1974)**
Rad.Effs., 23, p171.
- English, C.A., Eyre, B.L., Bartlett, A.F. & Wadley, H.N.G. (1977)**
Phil.Mag., 35A, p533.
- English, C.A., Eyre, B.L., & Summers, J. (1976)**
Phil.Mag., 34, p603.
- English, C.A., Eyre, B.L., & Holmes, S.M. (1980)**
J.Phys.F, 10, p1065
- English, C.A., & Jenkins, M.L. (1987)**
Mat.Sci.Forum., 15- 18, p1003.
- Erginsoy, C., Vineyard , G.H. & Englert, A. (1964)**
Phys.Rev., 133A, p595
- Erginsoy, C., Vineyard , G.H. & Shinzu, A. (1965)**
Phys.Rev., 139A, p118
- Eyre, B.L. (1973)**
J.Phys.F: Metal Phys., 3, p422.
- Eyre, B.L., & English, C.A. (1982)**
Point defects & defect interactions in metals, Tokyo.

- Eyre, B.L., Maher, D.M. & Perrin, R.C. (1977 a)**
J.Phys.F: Metal Phys., 7, p1359.
- Eyre, B.L., Maher, D.M. & Perrin, R.C. (1977 b)**
J.Phys.F: Metal Phys., 7, p1371.
- Farrell, K. (1977)**
J.Nuc.Mat., 68, p267.
- Faulkner, D. & Woo, C.H. (1980)**
J.Nuc.Mat., 90, p307.
- Firsov, O.B. (1959)**
J.Exp.Theo.Phys.(USSR), 36, p1517.
- Fleischmann, M. & Pons, B.S. (1989)**
J.Electroanal.Chem., 261, p301.
- Flynn, C.P., & Averback, R.S. (1988)**
Phys.Rev., 38B, p7118.
- Föll, H. & Wilkens, M. (1977)**
Phys.Stat.Sol., 39, p561.
- Foreman, A. (1990)**
To be published.
- Foster, A.H., Harder, J.M. & Bacon, D.J. (1987)**
Mat.Sci.Forum., 15-18, p849.
- Gardner, R.W., & Partridge, P.G. (1967)**
J.Sci.Inst., 44, p63.
- Gallagher, P.C.J. (1970)**
Met.Trans., 1, p2429.
- Gemmell, D.S. (1974)**
Rev.Mod.Phys., 46, p129.
- Gilbert, R.W., Farrell, K. & Coleman, C.E. (1979).**
J.Nuc.Mat., 84, p137.

- Greenland, T. (1989)**
Phys. World., 2, 12, p19.
- Griffiths, M., Faulkner, D. & Styles, R.C. (1983)**
J. Nuc. Mat., 119, p189.
- Griffiths, M., Loretto, M.H. & Smallman, R.E. (1983)**
J. Nuc. Mat., 115, p323.
- Griffiths, M., Loretto, M.H. & Smallman, R.E. (1984)**
Phil. Mag., 49A, p613.
- Griffiths, M., White, J., Loretto, M.H. & Smallman, R.E. (1982)**
"Point defects & defect interactions in metals", Tokyo press, p880.
- Guinan, M.W., Stuart, R.N. & Borg, R.J. (1977)**
Phys. Rev., 15B, p699.
- Habtetsion, S. (1989)**
PhD. Thesis., Sheffield University.
- Hales, R., Dobson, P.S. & Smallman, R.S. (1968)**
Met. Sci. J., 2, p224.
- Häussermann, F. (1972a)**
Phil. Mag., 25, p537.
- Häussermann, F. (1972b)**
Phil. Mag., 25, p561.
- Heinisch, H.L. (1981)**
Proc. 2nd Topical Meeting of Fusion Reactor Materials, Seattle. p143.
- Heinisch, H.L. (1983)**
J. Nuc. Mat., 117, p46
- Hertel, B. (1980)**
Rad Effs., 48, p45
- Hillairet, J., Malry, C., Espinasse, J., & Levy, V. (1970)**
Acta. Met., 18, p1285.

- Hitzenberger,C.,Karnthaler,H.P., & Korner,A. (1985)**
Acta.Met.,33,p1293.
- Holmes,S.M.,Eyre,B.L.,English,C.A. & Perrin,R.C.(1979)**
J.Phys.F:Metal Phys.,9,p2307
- Hossain,M.K. & Brown,L.M.(1977)**
Acta.Met.,25,p257.
- Howe,M.L.(1970)**
Phil.Mag.,22,p965.
- Hull,D. & Bacon,D.J.(1984)**
"Introduction to dislocations",Pergamon press.
- Jäger,W. & Merkle,K.L.(1981)**
J.Mic.Spect.Elect.,6,p437
- Jäger,W. & Merkle,K.L.(1988)**
Phil.Mag.,57A,p479.
- Jäger,W. & Wilkens,M.(1975)**
Phys.Stat.Sol.,32,p89.
- Jenkins,M.L.,Katerbau,K.H. & Wilkens,M.(1976)**
Phil.Mag.,34,p1141.
- Jenkins,M.L. & Wilkens,M.(1976)**
Phil.Mag.,34,p1155.
- Jenkins,M.L. & English,C.A.(1982)**
J.Nuc.Mat.,108,p46.
- Jenkins,M.L.,English,C.A. & Eyre,B.L.(1978)**
Phil.Mag.,38A,p97.
- Jones,R.H. & Charlot,L.A.(1980)**
J.Nuc.Mat.,91,p329.
- Jostsons,A.,Blake,R.G. & Kelly,P.M.(1980)**
Phil.Mag.,41,p903.

- Jostsons, A., Blake, R.G., Napier, J.G., Kelly, P.M. & Juchniewicz, R.**
(1962)
Plat.Met.Rev.,6,p100.
- Kelly, P.M., Blake, R.G. & Jostsons, A.(1976)**
J.Nuc.Mat.,59,p307.
- Kinchin, G.H., & Pease, R.S.(1955)**
Rep.Prog.Phys.,18,p1.
- Kinney, J.H. & Guinan, M.W.(1982)**
Phil.Mag.,46A,p789.
- Korner, A. & Karnthaler, H.P.(1983)**
Phil.Mag.,48A,p469.
- Kwadjo, R.(1973)**
Ph.D Thesis, University of Cambridge.
- Legrand, B.,(1984)**
Phil.Mag.,49B,p171.
- Lindhard, J.(1965)**
K.Dan.Vid.Selsk.Mat.Fyss.Medd.,34,p14.
- Lindhard, J., Scharff, M. & Schlott, H.E.(1963)**
K.Dan.Vid.Selsk.Mat.Fyss.Medd.,33,p1
- Lyle, R.L. & Merkle, K.L.(1975)**
Proc.Int.Conf.On.Rad.Effs & Tritium.Tech.For.Fusion, Gatlingburg,USA.
- Maher, D.M., Perrin, R.C. & Bullough, R.(1970)**
UKAEA AERE R.6348
- Mallett, C.M.(1989)**
Int.Rep.,University of Liverpool.
- Mastel, B. & Brimhall, J.L.(1965)**
Acta.Met.,13,p1109.
- Matthai, C.C. & Bacon, D.J.(1984)**
J.Nuc.Mat.,125,p138.

- Maury, F., Vajda, P., Lucasson, A. & Lucasson, P. (1970)**
Phil.Mag., 22, p1265.
- McIntyre, K. G. (1967)**
Phil.Mag., 15, p205.
- Merkle, K. L. (1966)**
Phys.Stat.Sol., 18, p173.
- Merkle, K. L. (1976)**
"Radiation damage in metals", U.S Society for metals, Metals park, Ohio, U.S.A., p58
- Moliere, G. (1947)**
Z.Naturforsch., A2, p133.
- Morning, J. R. (1968)**
"Diffusion kinetics for atoms in crystals", Toronto.
- Muncie, J. W., Eyre, B. L. & English, C. A. (1985)**
Phil.Mag., 52A, p309
- Naka, S., Lasalmonie, A., Costa, P., & Kubin, L. P. (1988)**
Phil.Mag., 5Z, p717.
- Nelson, R. S. (1969)**
UKAEA AERE-R6092
- Nelson, R. S. & Thompson, M. W. (1963)**
Phil.Mag., 8, p1677; erratum: Phil.Mag., 9, p1069.
- Norgett, M. J., Robinson, M. T., & Torrens, I. M. (1975)**
Nuc.Eng.Design., 33, p50.
- Northwood, D. O., Gilbert, R. W., Bahen, L. E., Kelly, F. M., Blake, R. G.,
Jostsons, A., Madden, P. K., Faulkner, D., Bell, W. & Adamson, R. B. (1979)**
J.Nuc.Mat., 79, p379.
- Oh, D. J. & Johnson, R. A. (1989)**
J.Nuc.Mat., 169, p5.
- Pedraza, A. J. & Fainstein-Pedraza, D. (1981)**
Phys.Stat.Sol., 63A, p723.

- Perrin, R. C. (1981)**
Unpublished work.
- Phythian, W. J., (1985)**
Ph.D. Thesis., University of Liverpool.
- Phythian, W. J., Eyre, B. L., Bacon, D. J. & English, C. A. (1987)**
Phil. Mag., 55A, p757.
- Phythian, W. J., Eyre, B. L., Bacon, D. J. & English, C. A. (1990)**
Phil. Mag., (In Press).
- Pramanik, D. & Seidman, D. N. (1983)**
Appl. Phys. Lett., 43, p639
- Protasov, V. I. & Chudinov, V. G. (1982)**
Rad. Effs., 66, p1
- Robinson, M. T. (1970)**
Nuc. Fiss. Reactors., (Brit. Nuc. Eng. Soc. London), p364
- Robinson, T. M. & Jenkins, M. L. (1981)**
Phil. Mag., 43A, p999.
- Rogerson, A. (1988)**
J. Nuc. Mat., 159, p43.
- Rossi, F. & Parkin, M. D. (1988)**
J. Mater. Res., 4, p137
- Ruault, M. O., Bernas, H., & Chaumont, J. (1979)**
Phil. Mag., 39, p757.
- Ruault, M. O. & Jäger, W. (1980)**
J. Mic., 118, p67.
- Rühle, M. R. (1969)**
"Rad. Dam. In. Reactor. Mat"., 1, p138.
- Ruhle, M. R., Wilkens, M. & Essman, U. (1965)**
Phys. Stat. Sol., 11, p819.

- Salisbury, I.G., Loretto, M.H. & Smallman, R.S. (1980)**
Proc. 6th. Int. Conf. H.V.E.M., p232.
- Schober, T., & Baluffi, R.W. (1968)**
Phys. Stat. Sol., 27, p195.
- Seeger, A. (1970)**
Rad. Effs., 2, p165.
- Seidman, D.N. (1973)**
J. Phys. F: Metal. Phys., 3, p393.
- Seller, G., Wilkens, M. & Katerbau, K.H. (1974)**
Proc. 8th. Int. Cong. E.M., 1, p618.
- Seitz, F. & Koehler, J.S. (1956)**
Progress in solid state physics., 2, p305
- Sigmund, P. (1969)**
Rad. Effs., 1, p15.
- Sigmund, P. (1977)**
"Inelastic Ion-surface Collisions", New York: Academic Press, p121
- Silsbee, R.H. (1957)**
J. Appl. Phys., 28, p1246
- Snow, D.B., & Breedis, J.F. (1974)**
Acta. Met., 22, p419.
- Stark, J. (1912)**
Phys. Z., 13, p973.
- Stathopoulos, A.Y. (1980)**
Ph.D. Thesis, University of Oxford.
- Thieringer, H.M., & Strunk, H. (1969)**
Z. Metallk., 69, p584.
- Thomas, L.E. & Baluffi, R.W. (1967)**
Phil. Mag., 15, p1117

- Thompson, D.A. (1981)**
Rad.Effs., 56, p105.
- Thompson, M.W. (1969)**
"Defects & radiation damage in metals", Pub. Camb.Univ.Press.
- Urban, K., Salle, B., Yoshida, N. & Zag, W. (1982)**
"Point Defects and Defect Interactions in Metals", p783.
- Wei, C-Y. & Seidman, D.N. (1981)**
Phil.Mag., 43A, p1419
- White, J. (1983)**
Ph.D.Thesis., Birmingham University.
- White, J., Smallman, R.E. & Loretto, M.H. (1983)**
Proc.10th.Int.Conf.Electron Microscopy., 2, p181
- Whitehead, M.E., Karim, A.S.A., Loretto, M.H. & Smallman, R.E. (1978)**
Acta.Met., 26, p983.
- Wilkins, M. (1975)**
"Proc.Int.Conf.Fundamental.Aspects.Of.Rad.Dam.In.Metals", p112.
- Winterbon, K.B., Sigmund, P. & Sanders, J.B. (1970)**
K.Dan.Vid.Selsk.Mat.Fyss.Medd., 37, No14.
- Woo, O.T. & Carpenter, G.J.C (1982)**
J.Nuc.Mat., 105, p326.
- Woo, O.T. & Carpenter, G.J.C (1983)**
Proc.10th.Int.Conf.Electron Microscopy., 2, p179.
- Yellen, D.H., Bacon, D.J., English, C.A. & Phythian, W.J. (1989)**
Vacuum., 39, p1141.
- Yoo, M.H. (1973)**
"Zr.in.Nuc.Appl" ASTM-AIME conf Oregon
- Zee, R.H., Carpenter, G.J.C., Rogerson, A. & Watters, J.F. (1987)**
J.Nuc.Mat., 150, p319.